Hemodynamics in Blood-Contacting Devices with Triply Periodic Minimal Surfaces for Extracorporeal Blood Therapies

Hämodynamik in blutkontaktierenden Apparaten mit dreifach periodischen Minimaloberflächen für extrakorporale Bluttherapien

Von der Fakultät für Maschinenwesen der
Rheinisch-Westfälischen Technischen Hochschule Aachen
zur Erlangung des akademischen Grades eines Doktors
der Ingenieurwissenschaften genehmigte Dissertation

vorgelegt von

Lukas Tobias Hirschwald

Berichter:
Univ.-Prof. Dr.-Ing. Matthias Wessling
Priv.- Doz. Dr. rer. medic. Christian Bleilevens

Tag der mündlichen Prüfung: 17. Februar 2025

Diese Dissertation ist auf den Internetseiten der Universitätsbibliothek online verfügbar.

Impressum

Titel: Hemodynamics in Blood-Contacting Devices with Triply Periodic Minimal Surfaces for Extracorporeal Blood Therapies
Hämodynamik in blutkontaktierenden Apparaten mit dreifach periodischen Minimaloberflächen für extrakorporale Bluttherapien

Autor: Lukas Tobias Hirschwald

Reihe: Aachener Verfahrenstechnik Series
AVT.CVT - Chemical Process Engineering
Volume: 50 (2025)

Herausgeber: Aachener Verfahrenstechnik
Forckenbeckstraße 51
52074 Aachen
Tel.: +49 (0)241 8095470
Fax.: +49 (0)241 8092252
E-Mail: secretary.cvt@avt.rwth-aachen.de
http://www.avt.rwth-aachen.de/AVT

Volltext verfügbar: 10.18154/RWTH-2025-01571

Universitätsbibliothek
RWTH Aachen University
Templergraben 61
52062 Aachen
http://www.ub.rwth-aachen.de

Published Content

Parts of this dissertation have been published.
Reproduced with permission from:

Lukas T. Hirschwald, Franziska Hagemann, Maik Biermann, Paul Hanßen, Patrick Hoffmann, Tim Höhs, Florian Neuhaus, Maerthe Theresa Tillmann, Petar Peric, Maximilian Wattenberg, Maik Stille, Tamara Fechter, Alexander Theißen, Patrick Winnersbach, Kai P. Barbian, Sebastian V. Jansen, Ulrich Steinseifer, Bettina Wiegmann, Rolf Rossaint, Matthias Wessling, Christian Bleilevens, John Linkhorst.
Enhanced Hemodynamics of Anisometric TPMS Topology Reduce Blood Clotting in 3D Printed Blood Contactors
Advanced Healthcare Materials, 2024
DOI: 10.1002/adhm.202403111

Danksagung

Ohne euch alle wäre das hier nichts geworden. Und dafür bin ich euch zutiefst dankbar! Denn diese Dissertation ist das Ergebnis vieler Hände, Gedanken und endloser Diskussionen. Über mehr als fünf Jahre hinweg haben mich viele großartige Menschen begleitet, von und mit denen ich lernen durfte, die mich und mein Tun hinterfragt haben und mir so geholfen haben diesen Meilenstein zu meistern.

Zunächst gilt mein besonderer Dank meinem Betreuer und Erstprüfer Matthias Wessling. Danke für dein Vertrauen in meine Arbeit, die vielen Freiheiten zur persönlichen Weiterentwicklung und die vielen lehrreichen Tage auf dieser riesigen, wissenschaftlichen Spielwiese. Ich werde mich gerne an die Zeit im Småland zurückerinnern! Auch meinem Zweitprüfer, Christian Bleilevens, danke ich für all das Herzblut. Dich als Zweitprüfer haben zu dürfen ist das i-Tüpfelchen dieser freundschaftlichen, interdisziplinären Kooperation!

Die Zeit mit euch im UKA in rosa Schweinchenkitteln und in der Cola-Bier-Ecke wird mir in besonderer Erinnerung bleiben. Mein erster Kontakt mit Blut für Experimente und wie es zu handhaben ist, die vielen Optimierungsschritte und der lockere Austausch, der mir die Welt der Medizintechnik geöffnet hat. Vielen Dank an Tamara, Patrick und Alexander. Und natürlich auch ein riesengroßes Dankeschön an Franziska Hagemensch. Du hast mich stets motiviert dran zu bleiben, mit mir den roten Faden gesucht und gefunden, geholfen als Vampir unsere Kolleg:innen zu einer Spende zu überreden, Module gehämmert, gelacht, gelitten und gefeiert.

Nochmals vielen Dank an die Blutspender:innen: Broschi, Kerstin, Saskia, Nelson, Lea, Valli, Niklas, Lukas, AnnKa, Maria, Johann, Florian und Lucas und das CT-Team aus Lübeck, Max, Maik und Solveig.

Und auch dem Kollegium, das mich stets unterstützt hat, mir Zeit für Probevorträge, Korrektur lesen und (nicht)-wissenschaftlichen Austausch geschenkt hat, möchte ich ebenfalls herzlich danken. Als Erstes gilt mein Dank John. Du hast mich mit 3D-Druck an die CVT gelockt, mich in zwei Abschlussarbeiten betreut und mir die wunderbare Welt der additiven Fer-

tigung und der Elektronik gezeigt, aber auch wie man Häuser baut. Wie langweilig eckig und analog wäre meine Leben ohne 3D-Drucker und Mikrocontroller...

Den Übergang an die CVT hast du, Georg, begleitet und geprägt. Die Welt der Mikrofluidik und Zellen ist klein und frickelig, aber auch äußerst spannend und ich freue mich auf das nächste Kapitel im Schwabenländle, danke dir. Danke Johann für die gemeinsame Bürozeit, deine offenen Ohren und Augen, Zeichenstunden am Whiteboard und gemeinsames Ärgern. Deine und die genialen Ideen von euch, AnnKa, Wibke, LuMa, Lucas, Maria P. und Paul, zum Vortrag haben mir sehr geholfen. Danke Stefan, Mojtaba und Maria R. für eure Korrekturen an diesem Papyrus und eure stets offene und fröhliche Art, euer Lächeln und Aufmuntern. Zum Start meiner Promotionszeit hatte ich riesiges Glück mit der ersten BA und MA. Ihr, Flo (Rolf) und Broschi, habt mir das Leben wirklich leicht gemacht. Ihr seid und wart entspannte Studis, Kollegen und Freunde, die mit Drive und Spaß viel bewegt haben (und bestimmt noch bewegen werden), danke.

Aber natürlich waren da noch all die anderen motivierten und engagierten Studis: Petar, Märthe, Tim, Patrick, Vera, Wiebke, Maik, Felix, Xianan und Paul. Ohne euch wär' hier gar nix los gewesen. Habt vielen Dank für eure tollen Arbeiten, eure Geduld mit mir und den vergessenen To-Do's, die Erinnerungen und den Ar***tritt am Morgen. Nicht zu vergessen, die weltbesten Hiwis: Alex, LuMa und Till. Dank euch hatte ich stets einen freien Rücken. Ein Hoch auf das Team Spitzenforschung!

Wissenschaft und Arbeiten an der CVT wäre nicht möglich ohne viele weitere Menschen, die teils still und heimlich im Hintergrund helfen. Mein ganz besonderer Dank gilt dir, Caro, für deine Wissbegierde und den Spaß am 3D-Druck. So konnte ich einen Großteil an Aufgaben guten Gewissens abgeben und wusste immer: Das läuft! Auch Karin und dem ZAL-Team möchte ich danken, vor allem für eure Ratschläge und die gute Laune, die jeden Tag im NGP zu einem fröhlichen macht. Danke Regina, denn ohne Moos nix los. Du hast mir immer geholfen kleine und große Hürden ohne Tamtam aus dem Weg zu räumen. Und natürlich auch dir, Susi, ein herzliches Dankeschön für das Rundum-sorglos-Paket, insbesondere im Promotionspro-

zess.

Wenn immer alles rund liefe, wäre ja auch langweilig. Manchmal eckt man an, manchmal ärgert man sich und braucht Menschen, denen man vertraut und die mitfühlen, aber auch wieder Erden. Liebes MuCo-Team ihr seid spitze! Danke Jonas, Arne, Jens, AnnKa, Valli und Paul!

Neben all der Wissenschaft und der Zeit am Lehrstuhl, gibt es auch noch einen Teil daneben, der glücklicherweise auch oft genug verschmilzt. Aber grade da, wo keine Überschneidung ist, kommen neue Ideen und ein anderer Blickwinkel her. Liebe Lisa, lieber Philipp, lieber Jens, ihr seid die weltbesten Mitbewohner:innen, die mir Geborgenheit, Ruhe und eine solide Basis gegeben haben. Dazu gehören auch meine Heimatfreunde: Liebe Lenu, lieber Vincent, danke, dass wir noch immer in Kontakt stehen, uns immer wieder treffen und nie aus den Augen verloren haben. Lieber Arne, lieber Maik, lieber Christian, auch ihr seid wie Mitbewohner und Familie für mich. Kulinarik, Technik und ein bisschen verrückt, so lässt es sich aushalten. Skifahren?

Meinen Eltern, Barbara und Uli, und meiner Schwester, Julia, möchte ich für Rückendeckung, Verständnis, Zuspruch und Unterstützung in jeder Situation danken. Ihr habt nie an mir gezweifelt und mir Freiräume gegeben so zu studieren und zu leben, wie ich möchte. Und so wurde es zum Glück kein gerader Weg, sondern ein ganz besonderer auf dem ich viel lernen und erleben konnte.

Zum Abschluss bleibt noch eine Person. Danke Carla! Ich hätte dich wohl in (fast) jedem Absatz erwähnen und noch unzählige mehr hinzufügen können. Und ich freue mich auf viele neue, spannende und gemeinsame Abschnitte.

Es jibt eben sone und solche, und dann jibt es
noch janz andre, aba dit sind die Schlimmstn, wa?

- Herta, Marc-Uwe Kling

Für Peggy, Else, Kurt und Wolfgang.
Julia, Barbara, Uli und Carla.

Wenn wir in 50 Jahren feststellen, es gibt gar keine Klimaerwärmung, dann hätten wir völlig ohne Grund dafür gesorgt, dass man in den Städten die Luft wieder atmen kann, dass die Flüsse nicht mehr giftig sind.
Da würden wir uns schön ärgern.

- Das Känguru, Marc-Uwe Kling

Artificial Intelligence (AI) Statement

Parts of this dissertation have been generated or rewritten with the help of an artificial intelligence (AI) model to improve readability. All ideas, considerations, and content are original and created by me. Therefore, AI systems are not concerned with intellectual property and this dissertation fully belongs to me, the human author. I encourage you to enjoy reading a clearer and easier-to-understand dissertation and to focus on the content, not the methods it was written with.

Contents

Abstract

Extracorporeal organ support devices are life-saving in cases of lung or kidney failure. They bridge the time until the organ heals or is transplanted, which can take weeks or months. These support devices replace the organ's function by exchanging breathing gases or unwanted species over hollow fiber membranes. While short-term support is generally considered safe, long-term application often leads to severe complications.

Until now, research has focused on improving biocompatibility by modifying the membrane's surface to reduce immune reactions that trigger blood clotting and eventually cause the device to malfunction. However, unphysiological flow conditions also trigger blood clotting. Additionally, commercial support devices suffer from an uneven flow distribution that leads to a broad residence time distribution (RTD) and unbalanced mass transfer driving forces. In order to exploit the device's full capacity, uniform residence times and homogeneous driving forces are essential.

Recently, triply periodic minimal surfaces (TPMS) have emerged as novel topologies to substitute hollow fiber membranes in blood-contacting devices. They offer more design freedom and increase mass transfer at lesser artificial surfaces by introducing secondary flows that reduce boundary layer effects. However, the influence of TPMS topologies on hemodynamics have hardly been investigated.

In this thesis, I employed computational fluid dynamics simulations, human whole blood experiments, and simulative optimization to evaluate and optimize the hemodynamics in differently designed modules with isometric and anisometric TPMS topology compared to a conventional tubular architecture. The simulations, validated by RTD experiments, highlighted the advantageous topology of TPMS that notably enhanced the flow distribution. By post-experimental computed tomography scanning, the location and amount of formed blood clots were visualized and quantified. The blood clot locations largely matched regions of elevated shear rates predicted by the simulations, emphasizing the importance of physiological hemodynamics. Furthermore, the blood clot amounts revealed significantly less clotting in the anisometric TPMS module compared to the tubular module. Further improvement of the RTD was simulatively achieved through Bayesian optimization by subdividing the module's fluid volume into independent domains and varying the domains' permeability. With this procedure, the RTD can be optimally tailored within a given external shape, e.g., a lung lobe, to enable the design of patient-individualized devices.

Overall, my work demonstrated that anisometric TPMS topologies with anisotropic properties have the potential to significantly improve hemodynamics in blood-contacting devices. Deploying anisometric TPMS as substitutes for hollow fiber membranes could be a major step forward in the long-term application and even implantability of lung or kidney replacement systems.

Zusammenfassung

Extrakorporale Organunterstützungssysteme sind bei Lungen- oder Nierenversagen lebensrettend. Sie überbrücken die Zeit bis zur Heilung oder Transplantation des Organs, was Wochen bis Monate dauern kann. Diese Systeme ersetzen die Funktion des Organs, indem sie Atemgase oder unerwünschte Stoffe über Hohlfasermembranen austauschen. Während die kurzfristige Unterstützung im Allgemeinen als sicher gilt, führt die langfristige Anwendung oft zu schweren Komplikationen.

Bisher hat sich die Forschung auf die Verbesserung der Biokompatibilität der Membran konzentriert, um Immunreaktionen zu verringern, die Blutgerinnung auslösen und schließlich zu einer Fehlfunktion des Systems führen. Aber auch unphysiologische Strömungsbedingungen lösen Blutgerinnung aus. Darüber hinaus leiden kommerzielle Systeme an ungleichmäßigen Strömungsverteilungen, die zu einer breiten Verweilzeitverteilung (RTD) und unausgewogenen Stoffaustauschtriebkräften führen. Um die volle Leistungsfähigkeit des Systems auszuschöpfen, sind gleichmäßige Verweilzeiten und homogene Triebkräfte unerlässlich.

Neuerdings sind dreifach periodische Minimaloberflächen (TPMS) als neuartige Topologien zum Ersatz von Hohlfasermembranen in blutkontaktierenden Systemen bekannt geworden. Sie bieten mehr Designfreiheit und erhöhen den Stoffaustausch bei weniger künstlicher Oberfläche, indem sie Sekundärströmungen erzeugen, die Grenzschichteffekte reduzieren. Der Einfluss von TPMS Topologien auf die Hämodynamik wurde jedoch bisher kaum erforscht.

In dieser Arbeit habe ich Strömungssimulationen, Experimente mit menschlichem Vollblut, und simulative Optimierung angewandt, um die Hämodynamik in unterschiedlichen Modulen mit isometrischer und anisometrischer TPMS Topologie im Vergleich zu einer tubulären Konstruktion zu untersuchen und zu optimieren. Die Simulationen, validiert durch RTD-Experimente, verdeutlichten die vorteilhafte TPMS Topologie, die die Flussverteilung erheblich verbesserte. Durch Computertomographieaufnahmen im Anschluss an die Experimente wurden die Position und das Volumen der gebildeten Blutgerinnsel visualisiert und quantifiziert. Die Positionen entsprachen weitgehend den in den Simulationen vorhergesagten Regionen mit erhöhten Scherraten, was die Bedeutung der physiologischen Hämodynamik betont. Darüber hinaus zeigte das Volumen signifikant weniger Koagulation im anisometrischen TPMS Modul im Vergleich zum tubulären Modul. Eine weitere Verbesserung der RTD wurde simulativ durch Bayes'sche Optimierung erreicht, indem das Modulvolumen in unabhängige Domänen unterteilt und die Permeabilität der Domänen variiert wurde. Mit diesem Verfahren kann die RTD optimal auf eine gegebene äußere Form, z. B. einen Lungenflügel, angepasst werden.

Insgesamt zeigte meine Arbeit, dass anisometrische TPMS Topologien mit anisotropen Eigenschaften das Potential haben, die Hämodynamik in blutkontaktierenden Systemen erheblich zu verbessern. Der Einsatz anisometrischer TPMS als Ersatz für Hohlfasermembranen könnte die langfristige Anwendung und sogar die Implantierbarkeit von Lungen- oder Nierenersatzsystemen einen entscheidenden Schritt voranbringen.

1. Introduction

Acute organ failures require immediate extracorporeal support therapies. Depending on the severity of the failure, a short-term (days) or long-term application (weeks to months) is necessary to allow the damaged organ to heal, be repaired, or be exchanged through transplantation. For irreversible damage, transplantation remains the best option, but donor organs are rare. Thus, to bridge the time gap until a donor organ is available, long-term extracorporeal support therapies are required. Common therapy needs are blood pumping, oxygenation, decarbonization, and purification due to heart, lung, kidney, and liver failure. [Aren2020; Meht2023; Duy 2021; Ronc2022]

Extracorporeal life support (ECLS) therapy uses a cardiopulmonary bypass for patients with acute cardiac or respiratory failure. It provides extracorporeal pumping and exchange of breathing gases via circulating the patient's blood through a **membrane lung** [Conr2018]. Additionally, the depletion of cytokines and pathogens due to kidney or liver failure may be necessary and is provided by integrating **purification devices** into the extracorporeal blood circulation [Meht2023]. Membrane lungs or purification devices are blood-contacting devices comprising functional surfaces to support or replace an organ optimally. However, these blood-contacting devices share common disadvantages regardless of their function. Goh et al. defined three factors influencing the application of extracorporeal support therapies: patient pathology, material properties, and blood flow hemodynamics [Goh2024]. Technologically, only the last two factors can be influenced, whereby the material properties have an impact at the molecular

level and determine biocompatibility. From an engineering perspective, the last factor, hemodynamics, is crucial, as it is determined by the device design associated with the following two challenges.

Non-Physiological Flow The blood is introduced into the devices through large tubing capable of transporting up to several liters of blood per minute. Thus, in the inlet area, the blood needs to be distributed instantaneously to cover the entire functional surface of the device. At the outlet, the treated blood is collected and transported further. However, due to poor distribution, the blood's residence time inside the device varies, causing an insufficient exploitation of the device's capacity. Furthermore, irregular residence times cause zones of low to no flow, referred to as stagnation, or high flow, called channeling. Irrespective of wasted device potential or insufficient blood treatment, stagnating or rushing blood causes severe issues, such as thrombus formation or blood damage. Additionally, areas that are not contributing to blood treatment but needed to distribute or collect the blood add additional priming volume. [Aren2020; Mine2015; Duy 2021; Park2020]

Shear-Induced Clotting In addition to the unfavorable flow distribution, the flow velocity changes drastically at the inlet and outlet, resulting in high shear rates with adverse effects. Shear rates of 10 to 2000 s^{-1} are common in the human body [Saka2015]. Between 10 to 1000 s^{-1}, the von Willebrand factor (vWf), a glycoprotein involved in hemostasis, changes and exposes more binding sites for platelets [Schn2007]. In their review, Casa et al. describe the effects of shear-induced thrombus formation, where platelets preferably bind to vWf at shear rates greater than approx. 630 s^{-1}. The vWf adheres to the foreign surface and thus captures circulating platelets that are then exposed to the high shear rates near the wall and are activated. [Casa2015] Thus, the lack of contact with healthy endothelium, which inhibits and reverses activation, results in the formation of a stable blood coagulum [De S2013].

1.1 Membrane Lungs

Membrane lungs are devices consisting of several thousand semi-permeable hollow fiber membranes physically separating the blood and gas phase, facilitating the exchange of breathing gases. For short-term applications such as open heart surgery, the advantages are substantial. However, the scenario alters drastically when addressing long-term lung damage because the protracted use over weeks or months leads to additional complexities. [Phil2018; Aren2020]

The most common complications include clot formation and deposits on the membrane's surface, demanding an exchange of the membrane lung [Phil2018; Aren2020]. This issue is rooted in the interaction between the blood and the large foreign surface of the membrane lung, which activates coagulation pathways and inflammatory responses [Phil2018] and promotes adhesion of proteins and cells that increase the diffusion distance [Aren2020; Mull2009]. Near the membrane, the flow profile promotes the formation of a boundary layer that further reduces gas exchange [Fern2017]. Additionally, suboptimal flow dynamics within the membrane lung create zones of stasis, uneven shear forces, and varied blood residence times [Hess2022]. Consequently, this necessitates the use of oversized membrane lungs to counteract performance decrease over time [Mart2023].

In commercial membrane lungs, blood flows on the outside of knitted hollow fiber mats, arranged in alternately rotated layers to form a hollow fiber bundle. The resulting deflected and tortuous flow path significantly increases mass transfer by decreasing the boundary layer. [Lim2006; Duy 2021] However, this configuration also tremendously increases the complexity of the flow profile [De S2013]. Factors influencing the flow profile are the diameter of the hollow fiber [Hira2009; Mart2023], the packing density [Hira2009; Mart2023], and the design of the housing [Hira2009; De S2013], but also external factors such as blood flow [De S2013]. Different parts of membrane lungs have been investigated hydrodynamically regarding the flow profile with computational fluid dynamics (CFD) simulations, such as the location of connection ports [Hira2009], the hollow fiber

arrangement [Bhav2011; Zhan2013; Fern2017], and general fluid flow distribution [Maza2006; Zhan2007]. Furthermore, the flow in the creeping to laminar range can cause deposits [Mart2023], particularly at the knitting points, which reduce the gas exchange and increase the flow resistance [Lehl2008]. This limitation can be actively counteracted by a periodic deformation of the hollow fibers with cycling oxygen pressure [Schl2014] or a rotating hollow fiber bundle [Polk2010]. Passive methods for inhibiting deposits are based on surface modification [Yao2024] or modified membrane materials (commonly polypropylene (PP) and polymethylpentene (PMP) are used) by adding fluoropolymers to increase hydrophobicity and decrease surface energy [Li2023; Park2020].

1.2 Purification Devices

Blood purification devices remove harmful substances, such as waste products and toxins. Hemodialyzers function as artificial kidneys by diffusively and/or convectively purifying the patient's blood by passing it through hollow fiber membranes that are in contact with a cleansing fluid, the dialysate [Duy 2021]. Hemoadsorbers are devices filled with adsorptive materials that come into contact with the blood to adsorb harmful substances [Hous2017].

In **hemodialyzers**, fibers in the module center experience higher blood throughput than peripheral ones, causing varying residence times and imbalanced mass transfer driving forces [Ronc2002; Eloo2002; Mine2015]. This effect becomes more pronounced with increasing hematocrit and also strongly depends on the inlet geometry [Ronc2001; Kim2009]. Conversely, the dialysate flow is higher in the periphery than in the module's center [Ronc2002; Eloo2002; Osug2004]. These mismatched blood and dialysate flows reinforce each other, which, in addition to unequal mass transfer driving forces, leads to an increased protein deposition that lowers mass transfer due to increased resistance [Kim2009]. Approaches to a more uniform flow distribution and improved dialyzer performance were investigated simulatively and experimentally. Kim et al. developed a model to study mechanical shaking to generate secondary flows to reduce protein depo-

sition [Kim2012]. Furthermore, the distribution of blood flow in dialyzers can be improved by using undulated [Yama2007] or curly [Luel2017] hollow fibers and optimized housing geometries [Yama2009; Hira2011; Hira2012; Kim2009].

For **hemoadsorbers**, to the best of my knowledge, no literature regarding the device perfusion and flow characteristics exists. However, the most common commercial hemoadsorption devices are the Toraymyxin, a fiber column device with immobilized polymyxin B, the Cytosorb, a device filled with porous polystyrene divinylbenzene copolymer beads, and the oXiris, a hollow fiber membrane device with modified AN69ST membranes [Bona2018; Anka2018]. The perfusion of the Toraymyxin and oXiris device (fiber or membrane based) are comparable to membrane lungs and dyalizers as discussed previously. The Cytosorb filled with porous beads resembles a packed bed as used in chromatography [Ronc2022; Snyd2011] where inhomogeneous column packing and non-uniform flow distribution yield major limitations [Umat2019]. Similar to the fiber based devices, radial flow distribution in the inlet is a key challenge due to the flow paths in the device's periphery being much longer than those close to the center axis [Umat2019]. To form more uniform flow paths and equal residence times, either the length of all streamlines must be aligned or locally adapted flow resistance allows for varying flow velocities. Furthermore, the concern of a clotted device and the limited maximal administration of 24 h necessitates the replacement of the devices yielding in blood loss in already critically ill patients [Bona2018].

1.3 Triply Periodic Minimal Surfaces for Medical Applications

From the previously stated literature, it is obvious that the inlet and outlet areas of blood therapy devices significantly contribute to a non-uniform flow distribution. Thus, the status quo of these devices demands novel approaches to improve flow distribution at physiological shear rates in order to

minimize the artificial surface and the impact on critically ill patients. However, the uniform arrangement of fibers or beads forms a uniform flow resistance, which hinders equal residence times. Furthermore, the fiber bundles of fiber based devices can hardly be adapted to other device geometries but cylindrical or cuboidal; thus, requiring voids for flow distribution in the inlet and outlet that do not contribute to blood treatment but increase the module volume.

In light of these challenges, recent research has pivoted towards exploring triply periodic minimal surfaces (TPMS) for medical applications [Feng2022]. TPMS structures are mathematical surfaces with a smooth and continuous topology as their mean curvature at all points is zero. The smallest entity, called unit cell, can be repeated in all three spatial directions. [Schw1890; Scho1970] By thickening the surface, an intertwined structure with multiple voids evolves that can fill an entire device of complex geometry [Hess2022; Barb2024] and offers the advantage of enhanced mass exchange efficiency [Hess2021; Femm2015a].

Like the uniform arrangement of fibers or beads, unit cells of the same size lead to uniform resistance. In cylindrical or cuboidal devices, the peripheral streamlines are always longer than the streamlines between the inlet and outlet ports. To ensure a uniform residence time along these streamlines of different lengths, variable flow resistances are required. The distortion of the TPMS unit cells to form an anisometric TPMS enables fluid channels of different sizes in order to vary the permeability and thus yield a more uniform flow distribution with narrow residence time distribution (RTD) [Hess2022; Barb2024; Tian2024].

1.4 Scope of the Thesis

Alongside the **introduction** (Chapter 1) and the **fundamentals** (Chapter 2), this work is divided into three chapters, followed by a **conclusion with future perspectives** (Chapter 6).

Chapter 3 focuses on the design of complex isometric and anisometric TPMS geometries. These were integrated into housings and investigated

as theoretical models by performing stationary and time-dependent CFD simulations on the entire TPMS modules. This theoretical approach was complemented by the additive manufacturing of these modules, allowing for an experimental investigation of their RTD and comparison of simulation and experiment.

Key Findings The chapter details significant achievements, most notably the validation of CFD simulations through direct experimental measurements of RTD. This validation underscores the reliability of CFD as a predictive tool for designing blood treatment devices. It was found that TPMS geometries greatly improve uniform perfusion across the module, presenting a substantial advance over traditional tubular geometries which are more prone to creating uneven flow patterns. Furthermore, the research identified stagnation zones and areas within the modules that exhibited high shear rate deviations, using an established blood viscosity model.

Chapter 4 revolves on investigating how different TPMS geometries affect blood coagulation when perfused with human whole blood. A critical aspect of the research involves the use of computed tomography (CT) scanning to analyze blood residues post-perfusion. This method provides a detailed visual and quantitative assessment of how blood interacts with the geometry inside the modules.

Key Findings It was found that anisometric TPMS geometries significantly reduce blood coagulation compared to other geometrical configurations, highlighting their potential to improve the biocompatibility and efficiency of blood-contacting medical devices. Moreover, the research demonstrated a clear correlation between regions of high shear rates within the different geometries and the formation of blood clots. This finding underscores the importance of geometric design in influencing blood dynamics and coagulation pathways. Additionally, the study successfully visualized the specific locations of blood clots within the modules and quantitatively determined their volumes, providing valuable insights into the spatial distribution and size of coagulation events.

In Chapter 5, a CFD simulation model, specifically tailored to optimize the RTD, was developed and utilized, crucial for ensuring efficient and uni-

form treatment within the modules. One aspect of the work involved the variation of geometric parameters to explore their impact on fluid dynamics. Additionally, the study abstracted the fluid volume within the module to optimize local flow resistances, an approach that aims to balance fluid dynamics across the module.

Key Findings This chapter showcases that the inlet area of a module plays a critical role in achieving a uniform flow distribution, highlighting the need for careful design in this region. The research also showed that selecting and weighting evaluation parameters within the optimization model presents a challenge, indicating the complexity of optimizations in choosing the best evaluation parameters. Moreover, the strategy of dividing the fluid volume into domains with variable flow resistances showed considerable potential for enhancing the overall utilization of the perfused modules, suggesting that targeted adjustments in local resistances can significantly improve module performance.

Previous Publications in Student Theses

This thesis's content and results emanate from research conducted under the affiliation and position of the author as research fellow and PhD candidate at RWTH Aachen University. The position is associated with the Chair of Chemical Process Engineering. The work comprises data based on the following student theses:

- Petar Peric, Master's thesis, 2021-03-31, *Direct fabrication of gas-permeable triply periodic minimal surface (TPMS) structures as extra-corporeal membrane oxygenators (ECMO)*
- Florian Yannick Neuhaus, Bachelor's thesis, 2021-05-25, *Analytic flow design of additively manufactured TPMS modules*
- Märthe Theresa Tillmann, Bachelor's thesis, 2021-07-15, *Investigation of Flows at Triply Periodic Minimal Surface Structures*

- Tim Höhs, Master's thesis, 2021-12-15, *Rapid prototyping design optimization of TPMS contactor modules based on fluid dynamic studies*
- Patrick Hoffmann, Bachelor's thesis, 2022-04-29, *Simulation-Based Design Optimization of Flow Distributors in the Field of Membrane Technology*
- Wiebke Wiessner, Master's thesis, 2022-12-22, *Direct laser writing of a microfluidic blood oxygenator using triply periodic minimal surface structures*
- Maik Biermann, Bachelor's thesis, 2023-03-20, *Hydrodynamic investigation of TPMS blood contactor modules via residence time distribution*
- Paul Hanßen, Bachelor's thesis, 2023-12-15, *Optimization of TPMS-structures for the usage in blood contactor modules using sequential design strategies and multiphysics simulations*

1

2. Fundamentals

2.1 Extracorporeal Blood Therapies

Extracorporeal blood therapies play an important role in critical care. When one or more organs are about to fail or have already failed they require support. Common functions that need to be supported or replaced are the oxygenation, decarbonization, movement of the blood, and removal of harmful substances from the blood. The following sections describe the basics of blood and extracorporeal blood therapy systems.

2.1.1 Blood

Human blood is a transport fluid that carries the respiratory gases oxygen and carbon dioxide, as well as nutrients and waste products. Blood is also a tissue, as it consists of many different cells with specific functions. The red blood cells, erythrocytes, make up the largest cellular proportion with a volume fraction of approximately 45 %. The white blood cells, leukocytes, and platelets, thrombocytes, make up less than a volume fraction of 1 %. The remaining 54 % of volume fraction is taken up by the blood plasma. More than 90 % in volume of the plasma consists of water. The remaining plasma components are proteins, nutrients, hormones, and minerals. [Schw2024; Hall2011]

All blood components are equally important. However, in the context of this work, red blood cells and platelets are particularly important.

Red Blood Cells The main task of red blood cells is to transport oxygen from the lungs to the body tissue. A red cell has the shape of a biconcave disk with a diameter of about 8 µm and a thickness of around 2 µm. This shape offers a large surface area to volume ratio. Inside, the red cells consist mainly of hemoglobin (Hb), which is responsible for transporting oxygen. However, they have no nucleus and cannot reproduce. The cell membrane holds everything together and is extremely flexible, so that red cells can also flow through constrictions that are smaller than their diameter. If the cell membrane is subjected to too much physical or chemical stress, the membrane can rupture and lose its contents, a process known as **hemolysis**. Every day, almost 1 % of new red blood cells, around $200 \cdot 10^9$, are produced in the bone marrow to replace the same number of old or damaged cells. [Schw2024]

Platelets The main task of platelets is called **hemostasis**, the prevention and control of blood loss, for example when blood vessel walls are injured. Platelets have a disk-like shape with a diameter of 2 to 4 µm and a thickness of around 0.5 µm. They have no cell nucleus and therefore cannot reproduce. Platelets contain a large number of proteins which enable the platelet to contract and they store a great amount of calcium ions. Furthermore, the cell contains various systems for the production of enzymes, adenosine triphosphate (ATP), adenosine diphosphate (ADP), and hormones. On their outer surface, platelets have a layer of glycoproteins that prevent adhesion to the endothelium but adhere very well to injured vessel walls or collagen from deeper tissue. Every day, around $400 \cdot 10^9$ new platelets are produced in the bone marrow, whose lifespan is around 8 to 12 days. [Schw2024; Hall2011]

Hemostasis, Blood Coagulation, and Hemodynamic Phenomena

Hemostasis is the process that prevents too much blood from leaking out of the vascular system, thus causing wound closure in the event of an injury as illustrated in Figure 2.1. Hemostasis consists of the following four steps:

1. Constriction of blood vessels to reduce blood flow (vascoconstriction, cf. Figure 2.1b).

2. Formation of a platelet plug by adherent platelets (cf. Figure 2.1c). The injured vessel wall activates platelets that come into contact with it. An activated platelet swells and changes into irregular shapes, it becomes sticky to adhere better to collagen and von Willebrand factor (vWf), and it releases a series of substances to activate surrounding platelets. In the case of minor injuries, platelet occlusion is usually sufficient to stop blood loss.

3. Formation of a fibrin clot due to coagulation (cf. Figure 2.1d). Fibrin fibers are integrated into the loose network of platelets, which trap red blood cells, other platelets and also blood plasma. The cross-linking of the fibers with everything trapped in them leads to a blood clot that closes the wound tightly. This seemingly simple process involves more than 50 substances that contribute to the coagulation of blood. The formation of fibrin fibers is the last part of the coagulation cascade, which consists of more than 13 influencing factors and can be initiated in different ways.

4. Repair of the vessel wall and dissolution of the blood clot.

Platelet activation can occur in different ways, with collagen, ADP, thromboxane A_2 (TxA_2), and thrombin being of chemical nature, and only the shear rate being a physical parameter. Within the human body, coagulants and anticoagulants are in balance. In particular, the smooth and special surface of the endothelium prevents the adhesion of clotting factors, activation of platelets, and coagulation cascade. The flow regime of the blood is laminar with Reynolds numbers between 200 and 400, except for the flows close to the heart, which fall into the turbulent regime with Reynolds numbers far beyond 2300. The wall shear rates range from around $10\,s^{-1}$ for large veins to $1000\,s^{-1}$ in arteries. [Schw2024; Hoss2017; Hall2011]

The Reynolds number Re is defined by Equation 2.1 in which ρ is the fluid's density, v is the fluid's superficial velocity, L is the characteristic

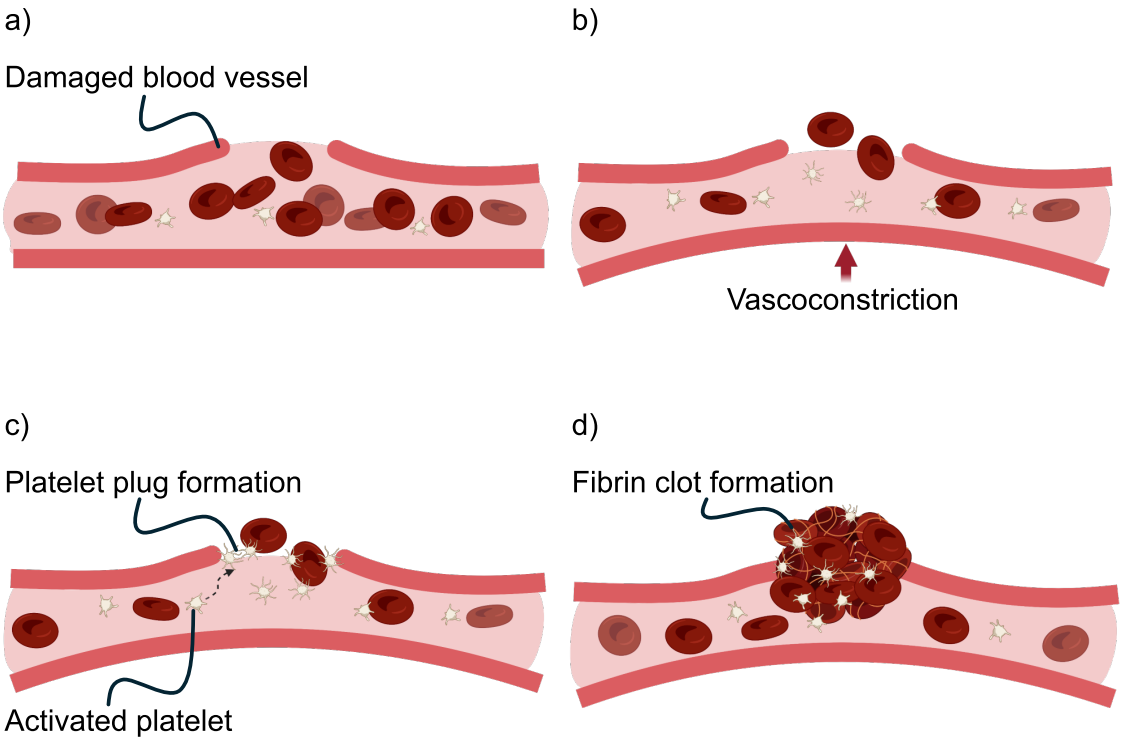

Figure 2.1: Stages of hemostasis: a) A damaged blood vessel. b) Illustration of the narrowing of the blood vessel to reduce the blood flow, called vascoconstriction. c) Formation of a platelet plug due to platelets changing their shape and adhering to the vessel wall to atract more platelets and other blood components to close the rupture. d) Formation of a fibrin clot. Fibrin fibers are integrated into the plug and then are cross-linked to firmly hold all entrapped components together and close the rupture with a clot. Created with BioRender.com.

length, and η the fluid's dynamic viscosity.

$$Re = \frac{\rho \cdot v \cdot L}{\eta} \tag{2.1}$$

The Reynolds number can be used to distinguish between different flow regimes: creeping flow, laminar flow, transitional flow, and turbulent flow. The boundaries between the flow regimes depend on the geometry through which the flow passes. In a pipe, the characteristic length is the pipe diameter. For creeping flow the $Re << 1$, laminar flow occurs until $Re = 2300$, and above $Re = 2900$ the flow is fully turbulent. For non-circular cross-sections, the hydraulic diameter as described in Equation 2.15 can be used. [Reyn1883; Schl2017]

In laminar blood flow in small capillaries, two effects relevant for hemosta-

sis occur:

Fåhræus Effect The smaller the capillary, the lower the blood's hematocrit (Hct) of flowing blood in the capillary (tube hematocrit, Hct_T) compared to the baseline value of blood entering or leaving the capillary (discharge hematocrit, Hct_D) [Fåhr1929; Prie1990]. This effect occurs in capillaries with a diameter of less than 500 µm and is based on the separation of the blood into three regions as illustrated in Figure 2.2a. The red blood cells are drawn towards the center of the capillary, creating a layer without red blood cells close to the wall. The transition between the two regions forms an intermediate region. In the core region, the local hematocrit is equal to the discharge hematocrit, in the boundary region it is zero, resulting in a mean that is lower than the discharge value [Herc2016]. Figure 2.2b plots the ratio of tube hematocrit and discharge hematocrit versus the capillary diameter for various values of discharge hematocrit according to a parametric description by Pries et al. [Prie1990]:

$$\frac{Hct_T}{Hct_D} = Hct_D + (1 + Hct_D) \cdot \left(1 + 1.7e^{-0.415 \cdot D} - 0.6e^{-0.011 \cdot D}\right) \tag{2.2}$$

Platelets are much smaller than red blood cells and present in smaller numbers, so they have negligible effects on blood rheology. With increasing shear rate and higher hematocrit, the platelets are moved closer to the wall and form a platelet-rich layer. This process is called margination and also occurs in larger vessels. [Foge2015] The same mechanism drives the spherical protein vWf towards vessel walls to support its adhesion where needed [Rack2017].

Fåhræus-Lindqvist Effect The Fåhræus-Lindqvist effect describes the decrease of apparent viscosity in small capillaries as depicted in Figure 2.3. This results from the Fåhræus effect, as the viscosity of a suspension depends on the number of particles. In the core region, the red blood cells are more densely packed, resulting in a higher local viscosity than close to the

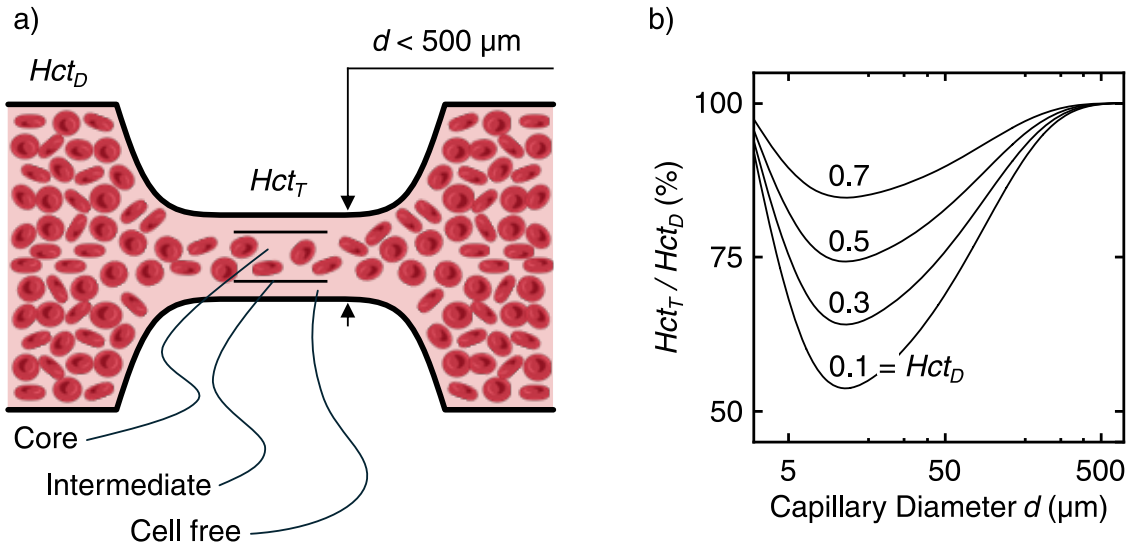

Figure 2.2: Fåhræus effect. a) In capillaries with a diameter d of less than 500 µm the blood separates into three regions: a cell free region close to the wall, an intermediate region, and a core region in the center of the capillary. Due to the cell free region, the mean hematocrit in the capillary (tube hematocrit, Hct_T) is lower than the baseline value of blood entering or leaving the capillary (discharge hematocrit, Hct_D). b) Ratio of Hct_T and Hct_D versus the diameter d for different values of Hct_D according to a parametric description by Pries et al. [Prie1990] (Equation 2.2). Parts of this figure have been created with BioRender.com.

wall. The thin boundary layer without red blood cells supports the gliding properties like a lubricant. As the boundary layer has a virtually constant thickness, only the viscosity of the core region changes. [Herc2016] The lower limit of this effect is formed by capillaries with a diameter the size of red blood cells (∼8 µm). This is where the blood viscosity reaches its minimum. As soon as the capillary becomes too small and deformation of the red blood cells becomes necessary, the viscosity increases rapidly. Pries et al. fitted experimental data of blood with an hematocrit of 0.45 to give an equation for the relative apparent viscosity $\eta_{rel0.45}$ versus the capillary diameter D [Prie1992]:

$$\eta_{rel,0.45} = 3.2 + 220 \cdot e^{-1.3 \cdot D} - 2.44 \cdot e^{-0.06 \cdot D^{0.645}} \tag{2.3}$$

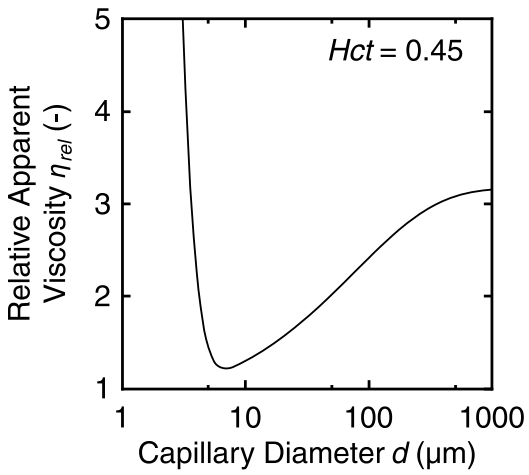

Figure 2.3: Relative apparent viscosity ($\eta_{rel,0.45}$) at an hematocrit of 0.45 versus the capillary diameter d according to the experimental fit given in Equation 2.3 by Pries et al. [Prie1992]. The decrease of apparent viscosity for decreasing capillary diameters is called the Fåhræus-Lindqvist effect.

Shear-Induced Clotting Depending on the hematocrit, the Fåhræus effect leads to a margination of the platelets and the vWf. As the shear rate increases, the movement of these particles also increases, causing them to collide more frequently with the surface of the surrounding wall. Depending on the surface properties of the wall, vWf adsorb, with healthy endothelium not allowing adhesion, but artificial surfaces leading to different degrees and speeds of adhesion. [Casa2015; Rack2017] Furthermore, vWf elongate at an increased shear rate (approx. $>1000\,\mathrm{s}^{-1}$) and thus expose considerably more anchors and binding sites. [Schn2007] The binding of vWf with the platelet's surface protein glycoprotein Ib (GPIb) is one of the fastest bindings in biology. This means that even platelets that only have very brief contact with an adsorbed vWf are captured or at least slowed down. A platelet bound to vWf is thus retained in a region of increased shear rate where the platelet switches to the activated state and attracts further platelets. A network of vWf, platelets, and other captured blood components is formed; the coagulation cascade begins. [Casa2015]

2.1.2 Blood Oxygenation and Decarbonization

Humans need energy to live. This energy is supplied by food, which is broken down and metabolized in a series of chemical reactions. The most basic reaction converts carbohydrates ($C_m[H_2O]_n$) with oxygen (O_2) to water (H_2O) and carbon dioxide (CO_2), releasing energy which is then available for other activities. Therefore, O_2 must be provided and CO_2 removed, since CO_2 becomes toxic if it exceeds a certain threshold. Both gases are dissolved and bound in the blood and are exchanged with the environment via the lungs. [Hall2011]

The Lungs

Respiration ensures the supply of O_2 and removal of CO_2 and is divided into four functions:

1. Exchange of air between the lungs and the environment.
2. Transfer of O_2 and CO_2 between the alveoli and the blood.
3. Transportation of respiratory gases within the body.
4. Regulation of ventilation and other aspects of respiration.

In the context of this work, I will focus on the second aspect, as this is one of the most crucial for artificial support systems. The lungs are the organ in which O_2 is transferred to the blood and CO_2 is removed from the blood. This occurs diffusively via the respiratory membrane which forms the boundary between the pulmonary capillaries (blood side) and the pulmonary alveoli (air side) as shown in Figure 2.4a. The amount and speed of which O_2 and CO_2 can be transported between the gas phase and the blood phase mainly depends on two fundamental physical laws: diffusion and solubility. Between the gas phase and the respiratory membrane dissolution of the gases takes place and within the respiratory membrane and the body fluids the gases move via diffusion, unless they are convectively moved by, e.g., the blood stream. [Hall2011]

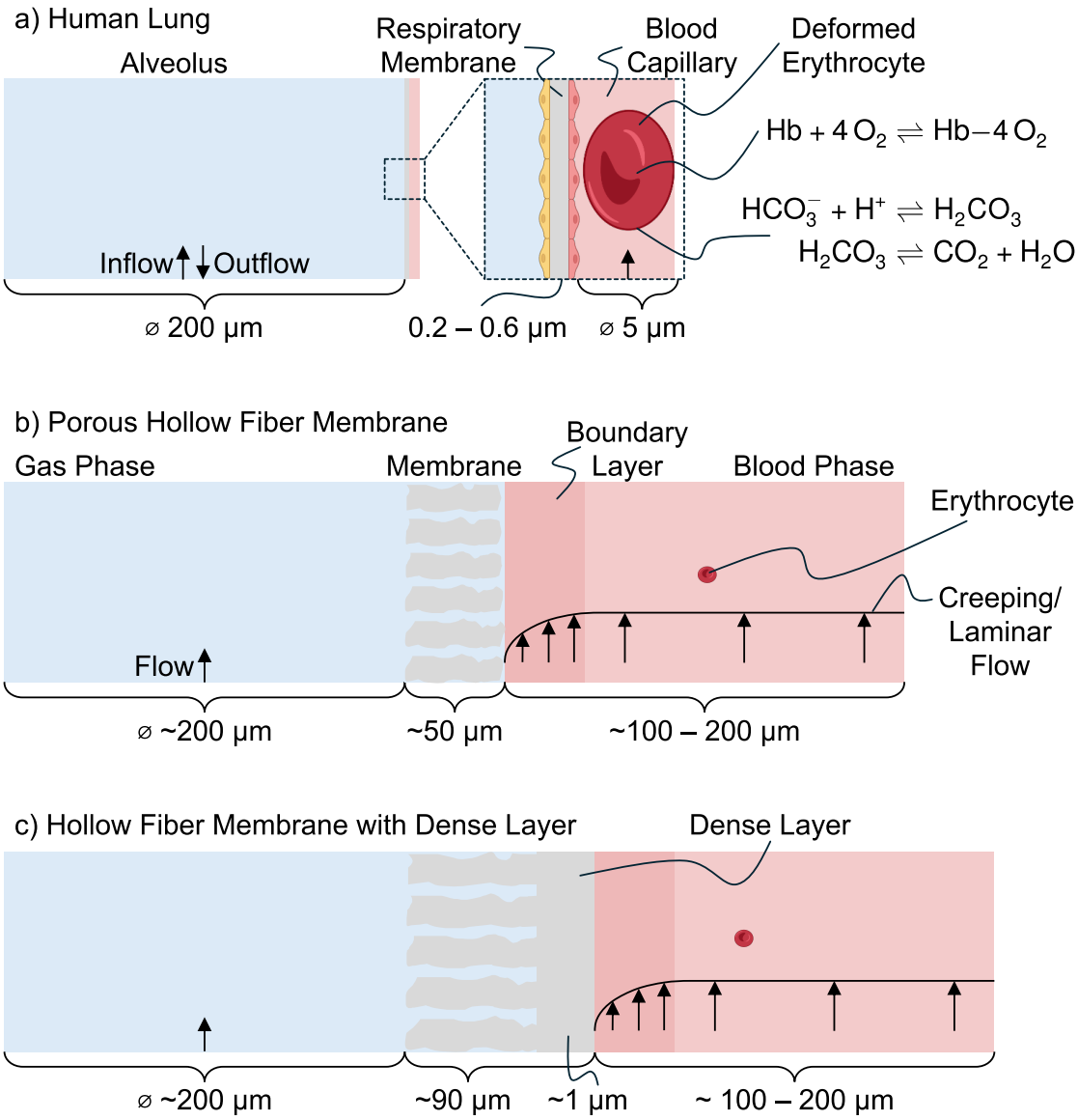

Figure 2.4: Visualization of the boundary between gas and blood phase in the human lung and artificial membrane lungs. Notably, the thicknesses of the different membranes and blood phases are distinct. a) Human lung with alveolus, respiratory membrane, and blood capillary. Inside the blood phase, oxygen binds to hemoglobin inside the erythrocytes. Bicarbonate ions are transformed into carbon dioxide through enzymatic catalysis at the surface of the erythrocytes. b) Porous hollow fiber membrane, e.g., polypropylene (PP). c) Hollow fiber membrane with dense layer, e.g., polymethylpentene (PMP).

Table 2.1 lists the Henry's law solubility constants and relative diffusion coefficients for the most important respiratory gases. Evidently, CO_2 is much more soluble and diffuses much faster than O_2, which is why different transport mechanisms exist for both gases in blood.

Table 2.1: Henry's law solubility constants H_s^{cp} in water at reference temperature of 298.15 K [Sand2023] and relative diffusion coefficients compared to oxygen $\frac{D}{D_{O_2}}$ in body fluids [Hall2011].

Substance	H_s^{cp} ($\mathrm{mol\,m^{-3}\,Pa^{-1}}$)	$\frac{D}{D_{O_2}}$ (-)
Oxygen (O_2)	$13 \cdot 10^{-6}$	1.0
Carbon dioxide (CO_2)	$340 \cdot 10^{-6}$	20.3
Carbon monoxide (CO)	$10 \cdot 10^{-6}$	0.8
Nitrogen (N_2)	$6 \cdot 10^{-6}$	0.5

Diffusion and Fick's Law Diffusion is the undirected, random movement of particles due to their molecular motion. The mechanism of diffusion is described by Fick's first law in Equation 2.4, where J ($\mathrm{mol\,m^{-2}\,s^{-1}}$) is the diffusive flux which is the product of the concentration gradient $\frac{dc}{dx}$ ($\mathrm{mol\,m^{-4}}$) and the diffusion coefficient D ($\mathrm{m^2\,s^{-1}}$) [Fick1855].

$$J = -D \cdot \frac{dc}{dx} \tag{2.4}$$

Solubility and Henry's Law Henry's law states that the partial pressure of a gas acting on a liquid is directly proportional to the concentration of the gas in the liquid. The proportionality is expressed by the Henry's law solubility constant H_s^{cp} ($\mathrm{mol\,m^{-3}\,Pa^{-1}}$) as stated in Equation 2.5, where c_l ($\mathrm{mol\,m^{-3}}$) is the molar concentration of the gas in the liquid and P_i (Pa) is the partial pressure of the gas in the gas phase.

$$H_s^{cp} = \frac{c_l}{P_i} \tag{2.5}$$

Breathing Gas Exchange All blood pumped by the heart flows through the lungs. At rest, this is around $5\,\mathrm{L\,min^{-1}}$ while during exercise, the blood flow increases by a factor of 4 to 7 (20 to $35\,\mathrm{L\,min^{-1}}$). In order to compensate for the increased blood flow during exercise without a significant increase in pressure, the pulmonary capillaries widen and additional ones are opened. Between an alveolus and a blood capillary there is a partial

pressure difference of 64 mmHg for O_2 and 5 mmHg for CO_2. Over an area of approximately 70 m^2, 250 mL min^{-1} O_2 and 200 mL min^{-1} CO_2 can be exchanged at rest and over 1000 mL min^{-1} O_2 and 800 mL min^{-1} CO_2 during exercise. The lungs contain around 450 mL of blood, of which around 70 mL is in the pulmonary capillaries in direct contact with the respiratory membrane. This results in a residence time of 0.8 to 0.3 s (rest vs. exercise) during which gas exchange takes place. [Hall2011]

Figure 2.5 shows the partial pressure profile for O_2 between the gas and the blood phase. In the upper part the profile for the human lung shows a constant bulk concentration inside the gas phase (alveoli). At the interface between the alveolus and and the respiratory membrane the O_2 adsorbs onto the membrane according to Henry's law (Equation 2.5) and then diffuses according to Fick's law (Equation 2.4 through the membrane. On the membrane blood interface, the O_2 molecules desorb into the blood phase, where most of it directly binds to Hb: $Hb + 4\,O_2 \rightleftharpoons Hb-4\,O_2$. Thus, only a small portion of O_2 is dissolved in the blood plasma where it distributes via diffusion. Due to the blood flow, all O_2 can directly be taken up, yielding a constant partial pressure in the blood phase.

In Figure 2.6 the partial pressure profile for CO_2 between the gas and the blood phase is shown. In the blood phase, bicarbonate associates into carbonic acid which is then transformed into CO_2 and H_2O. The dissolved CO_2 adsorbs onto the respiratory membrane, diffuses through the membrane, and desorbs into the gas phase.

Oxygen Transport in Blood In the blood, 97 % of the oxygen is chemically bound to Hb, which has a capacity of 1.34 mL O_2 per gram of Hb. Normally, 100 mL of blood contain about 15 g of Hb which leaves the lungs with a saturation of 97 %, resulting in an oxygen binding capacity of about 19.4 mL O_2 per 100 mL of blood and additional 0.6 mL O_2 in dissolved form. In the resting state, only about 5 mL O_2 per 100 mL of blood are consumed. [Hall2011]

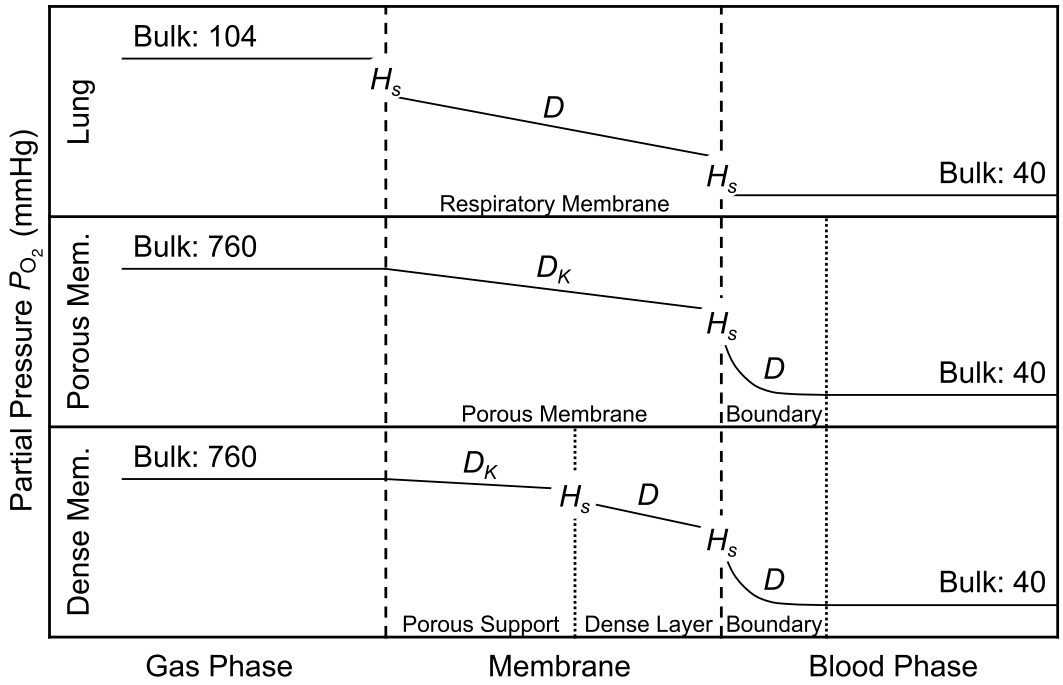

Figure 2.5: Partial pressure (P_{O_2}) profile of oxygen (O_2) from gas to blood phase for the human lung (upper part), an artificial lung with porous membrane (center part), and an artificial lung with dense membrane (lower part). In the bulk phase a constant P_{O_2} is assumed. D is the diffusion coefficient, D_K is the Knudsen diffusion coefficient, and H_s the Henry solubility constant, indicating diffusion or sorption, respectively. Due to the flow of the blood phase, diffusion and convection superimpose and form an unknown curve in the boundary layer between membrane and blood phase.

Carbon Dioxide Transport in Blood CO_2 is transported in the blood in three states. Around 70 % is in the form of bicarbonate ions (HCO_3^-), which are produced by dissociation of carbonic acid ($H_2CO_3 \rightleftharpoons HCO_3^- + H^+$). Carbonic acid is mainly formed from CO_2 in red blood cells by the catalysis of the enzyme carbonic anhydrase. A further 23 % of CO_2 reacts reversibly with amine radicals of Hb to form carbaminohemoglobin ($CO_2 \cdot Hb$). Due to the weak bond between CO_2 and Hb, the CO_2 can easily be released again. The remaining 7 % of CO_2 are transported in dissolved form in the blood. A total of around 4 mL of CO_2 per 100 mL of blood is transported from the tissue to the lungs in a resting state, with a total capacity of around 50 mL of CO_2 per 100 mL of blood. [Hall2011]

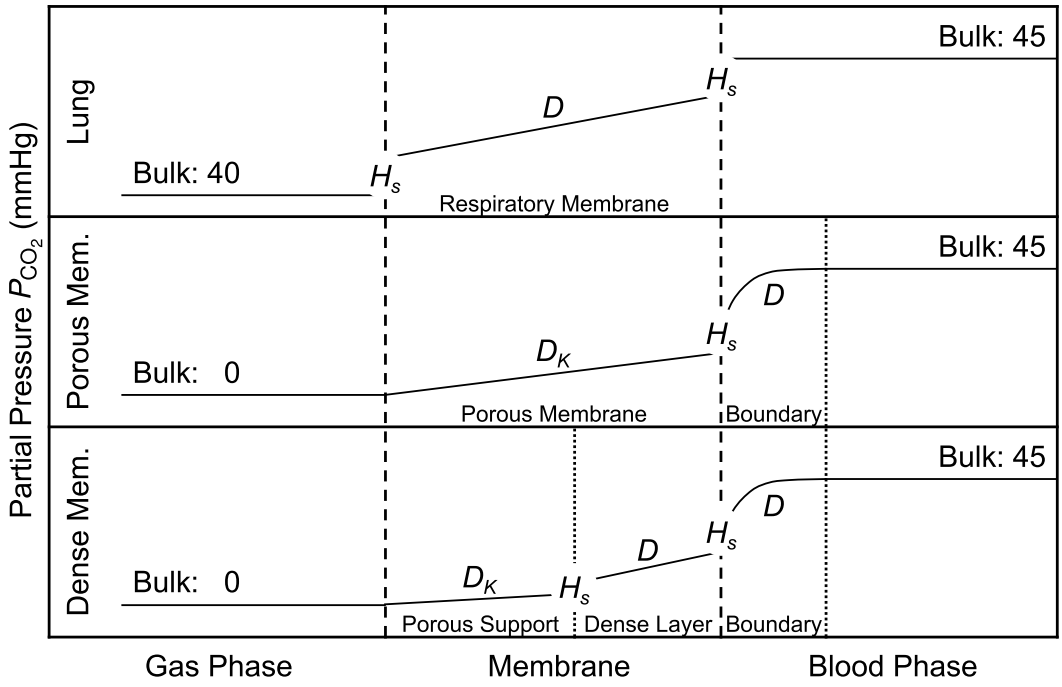

Figure 2.6: Partial pressure (P_{CO_2}) profile of carbon dioxide (CO_2) from gas to blood phase for the human lung (upper part), an artificial lung with porous membrane (center part), and an artificial lung with dense membrane (lower part). In the bulk phase a constant P_{O_2} is assumed. D is the diffusion coefficient, D_K is the Knudsen diffusion coefficient, and H_s the Henry solubility constant, indicating diffusion or sorption, respectively. Due to the flow of the blood phase, diffusion and convection superimpose and form an unknown curve in the boundary layer between membrane and blood phase.

Membrane Lung

Extracorporeal life support (ECLS) comprises two systems for exchanging respiratory gases with blood outside the human body. Extracorporeal membrane oxygenation (ECMO) supplies the patient's blood with O_2 and removes CO_2. It is used in cases of heart failure, cardiorespiratory failure, or respiratory failure. Extracorporeal CO_2 removal (ECCO$_2$R) mainly removes CO_2 and is used to protect the lungs in the event of excessive CO_2 concentrations. As the two systems are used to treat different diseases, the areas of application and conditions are also different, meaning that the devices used also differ. [Conr2018]

Nevertheless, the core of both systems is the membrane lung. This device consists of many thousands of hollow fiber membranes with gas flow-

ing on the lumen side and blood flowing around the shell side. Commercial membrane lungs are available in different sizes for different patient groups, such as children or adults. When perfused with pure O_2, a partial pressure difference of 720 mmHg for O_2 and 45 mmHg for CO_2 drives the gas exchange. Artificial membrane lungs achieve a maximum gas exchange surface area of around 2.5 m^2 and can transfer around 400 mL min^{-1} of O_2 and CO_2 at blood flows of up to 7 L min^{-1}. At the maximum permitted blood flow, a pressure of up to 250 mmHg drops via the membrane lung. The priming volume is up to 320 mL. Two main materials are used for the hollow fibers: polypropylene (PP) for short-term applications of up to 6 hours and polymethylpentene (PMP) for applications of up to 30 days. [Evse2019]

Microporous Polypropylene Membranes In membrane lungs with microporous ultrafiltration PP membranes, blood and gas are brought into direct contact as visualized in Figure 2.4b. On the lumen side of the hollow fibers, pure O_2 is flowing. Around the fibers, on their shell side, blood is flowing and developing a creeping to laminar flow profile. In between both phases, the porous membrane wall forms the interface. The gas transport resistance of a microporous membrane can be described by Knudsen diffusion that is valid for pores of up to 50 nm. The very small pores of state of the art PP hollow fiber membranes of around 30 nm prevent the blood plasma from penetrating the pores and passing through the membrane due to surface tension. Nevertheless, plasma leakage occurs over time as evaporated water condenses in the pores or blood components adsorb on the membrane and thus enable wetting of the pores. [Evse2019; Most2021]

The center part of Figure 2.5 and 2.6 shows the partial pressure profiles for O_2 and CO_2 with a porous membrane. Due to the porosity of the membrane, there is an equilibrium of partial pressure at the interface between gaseous bulk phase and membrane. Inside the membrane the gases diffuse according to Fick's law. At the interface between the membrane and the blood phase, the gases adsorb/desorb. Due to the flow of the blood phase, diffusion and convection superimpose and form an unknown curve. In comparison to the human lung, as depicted in Figure 2.4a, there is only

very little direct contact between erythrocytes and the shell of the membrane. Thus, all gases move via diffusion in the blood plasma over much longer distances.

To describe the diffusion in the porous membrane, the Knudsen diffusion coefficient D_K ($m^2\,s^{-1}$) is given in the following Equation 2.6:

$$D_K = \frac{d_p}{3}\sqrt{\frac{8RT}{\pi M}} \tag{2.6}$$

Here, d_p (m) is the pore diameter, R ($8.314\,J\,mol^{-1}\,K^{-1}$) the gas constant, T (K) the temperature, and M_i ($kg\,mol^{-1}$) the molar mass of the species. Knudsen diffusion follows Fick's first law (Equation 2.4). Substituting D_K into Fick's law (Equation 2.4) and integrating over the diffusive length dx from 0 to δ, the diffusive flux in a microporous membrane is given by Equation 2.7

$$J = -\frac{D_K}{\delta} \cdot \Delta c \tag{2.7}$$

Thus, the speed at which gases diffuse through a microporous membrane can be increased by making the membrane thinner, a higher concentration gradient, or changing the material that alters the diffusion coefficient.

Dense Polymethylpentene Membranes In membrane lungs with dense PMP membranes, blood and gas have no direct contact and the dense layer prevents the blood plasma from passing through the membrane. The gas transport through the membrane plays a decisive role, as the gas solubility and diffusivity have a major influence on the transport rate described by the diffusion-solution model. Solubility is the relevant parameter for the gases to enter or leave the membrane and diffusion describes the transport within the membrane. [Most2021]

The lower part of Figure 2.5 and 2.6 shows the partial pressure profiles for O_2 and CO_2 with a dense membrane. Due to the porous support of the membrane, there is an equilibrium of partial pressure at the interface between gaseous bulk phase and porous support. At the interface between the porous support and the dense layer, sorption takes place, while inside

the membrane the gases diffuse according to Fick's law. At the interface between the dense layer and the blood phase, the gases again adsorb/desorb. Due to the flow of the blood phase, diffusion and convection superimpose and form an unknown curve. In comparison to the human lung, as depicted in Figure 2.4a, there is only very little direct contact between erythrocytes and the shell of the membrane. Thus, all gases move via diffusion in the blood plasma over much longer distances.

To describe the transport over a dense membrane, the solution-diffusion model emerges by substituting Henry's law for sorption into Fick's law for diffusion as shown in Equation 2.8.

$$J = -D \cdot \frac{d(H_s^{cp} \cdot P_i)}{dx} = -D \cdot H_s^{cp} \cdot \frac{dP_i}{dx} \tag{2.8}$$

By integrating over the diffusive length dx from 0 to δ, the diffusive flux in a dense membrane is given by Equation 2.9. $\frac{D \cdot H_s^{cp}}{\delta}$ is the permeance Q with units $\mathrm{m^3\,m^{-2}\,h^{-1}\,bar^{-1}}$.

$$J = -\frac{D \cdot H_s^{cp}}{\delta} \cdot \Delta P_i = Q \cdot \Delta P_i \tag{2.9}$$

Thus, the speed at which gases travel through a dense membrane can be increased by making the membrane thinner, a higher partial pressure gradient, or changing the material that alters the diffusion and Henry coefficient.

Resistances from Gas Phase to Blood Phase During oxygenation or decarbonization, the respiratory gases move via different mechanisms as illustrated in Figure 2.5 and 2.6. The overall transport resistance can be divided into three main sections as shown in Equation 2.10: gas phase, membrane, and blood phase.

$$R_{total} = R_{gas} + R_{membrane} + R_{blood} \tag{2.10}$$

Within the gas phase, the gases can move freely and experience hardly any resistance. Due to the high mobility of the gas molecules and the convective flow, a boundary layer at the gas-membrane interface is neglected.

Through the membrane, however, the resistance is not negligible. Compared to the human lung, in which the respiratory membrane is extremely thin and gases are well soluble, artificial membranes are around 100-fold thicker. Their gas permeabilities vary depending on various parameters, such as thickness, material, or structure (porous or dense). At the interface between the membrane and the blood phase, the respiratory gases dissolve, degas, absorb or desorb, usually described by Henry's law. Within the boundary layer, which is created by the Fåhræus effect, the respiratory gases are transported diffusively, which can be described with the help of Fick's first law, and convectively by the blood flow. In the main flow in which the red blood cells are located, the respiratory gases react with the red blood cells.

The highest resistance and greatest challenge in artificial systems is the boundary layer due to the low solubility of O_2 in blood plasma. In the human lung this boundary layer is cleverly bypassed with capillaries of the same size as the red blood cells to bring the cells into contact with the respiratory membrane as visualized in Figure 2.4. [Most2021]

2.1.3 Blood Purification

Humans consume liquid and solid food, which is metabolized and excreted again. Nutrients as well as other ingested substances and metabolites are transported in the body by the blood. The purification of the blood by removing unnecessary or even harmful substances, is mainly carried out by the kidneys and liver.

The Kidneys and the Liver

Around 1.1 L min^{-1} of blood flows through the kidneys, of which only a small amount is required to supply the kidneys. Most of the blood is transported to the kidneys to be filtered and to restore the balance in the body fluids. The approximately 800 000 to 1 000 000 nephrons per kidney filter around 20 % of the blood plasma flowing through the kidneys, which adds up to around 180 L of filtered blood plasma per day. Hence, the plasma is filtered

about 60 times a day and electrolytes, amino acids, and glucose are reabsorbed and excess amounts excreted. In addition, the end products of metabolism, such as urea, creatinine, uric acid, and urates are excreted. Once destroyed, nephrons cannot be regenerated. As a result, the performance of the kidneys decreases over time as nephrons become damaged over the years. [Hall2011]

The liver is the central metabolic organ in humans and is responsible for the metabolism of fat and proteins, but also for the production of bile and it functions as a detoxification center. It is supplied with blood via two vessels. Arterial blood is used to supply the liver cells. Venous blood from the digestive tract delivers all substances that have entered the bloodstream from food, including nutrients and toxins, to the liver. After liver tissue loss, most of the lost tissue can be regenerated. [Hall2011]

Artificial Kidney: Hemodialysis, Hemodiafiltration, Hemofiltration

If kidney function is severely impaired, the balance of substances in the body fluids is at risk and harmful substances must be removed. Hemodialysis is an extracorporeal way of cleaning the blood and removing excess water. In this process, the blood is passed through the lumen of hollow fiber membranes at a flow rate of around 300 to 600 $\mathrm{mL\,min^{-1}}$. A washing fluid, the dialysate, flows around the membranes on the shell side. The exchange of substances across the porous membranes takes place diffusively up to a size of around 65 kDa, the size of albumin, which must always be held back in the blood. For substances smaller than 65 kDa, mainly electrolytes and glucose, a composition is adjusted in the dialysate so that these substances are supplied to or removed from the patient as required. Urinary substances are always removed. To remove excess water from the patient a slight pressure difference can be applied to generate some convective flow. Hemodialysis operates without a pressure difference, thus exchange is driven by diffusion. Hemodiafiltration uses both, diffusion and convection and hemofiltration is based upon mere convection. [Duy 2021]

Hemoadsorbtion

In the event of an infection, the immune system is activated and fights it. If the infection cannot be controlled, the immune system is further activated until an dysregulated immune response with a cytokine storm occurs. This can also lead to septic shock, a critically reduced tissue perfusion that often results in multi-organ failure. [Meht2023]

To stop the immune reaction and restore the immune balance, the pro-inflammatory substances must be removed. Dialysis has not yet been able to achieve significant and clear results for this purpose due to protein-bound toxins that can not be removed. Depending on the infection and the inflammatory substances released, various hemoadsorbers are used, some of which adsorb molecules specifically, others non-specifically. [Meht2023]

Beads or fibers are mainly used as sorbents. One device based on porous polymer beads is the Cytosorb cartridge, which can be used at a blood flow of 150 to 700 mL min^{-1} for up to seven consecutive days. Hydrophobic molecules, such as pro- and antiinflammatory mediators, with a size of up to 60 kDa are adsorbed non-specifically but endotoxins can not be removed. The mass balance is described by Equation 2.11. Here $c_{blood,initial}$ is the concentration of a species in the blood at the start of treatment and V_{blood} is the total blood volume. The product of these two, i.e. the left-hand side of the equation, indicates the total amount of a species present in the blood. The right-hand side of the equation is the equilibrium between blood and sorbent, where c_{blood} is the concentration of the species and thus indicates the remaining amount of the species in the blood. $c_{sorbent}$ is the concentration of the species on the sorbent (mol unit^{-1} of sorbent mass) and $m_{sorbent}$ is the total mass of the sorbent, resulting in the amount of adsorbed species. The difference between the two terms on the right-hand side approximately indicates the driving force for adsorption. [Ronc2022; Mona2019]

$$c_{blood,initial} \cdot V_{blood} = (c_{blood} \cdot V_{blood}) + (c_{sorbent} \cdot m_{sorbent}) \tag{2.11}$$

The flow through a packed bed of porous particles can be described by the

physical laws of Darcy and Kozeny-Carman. [Ronc2022]

Fiber-based devices are Toraymyxin and oXiris. The Toraymyxin cartridge uses fibers with immobilized polymyxin B, which mainly adsorb endotoxins. The use is limited to 2 h application per day for two consecutive days at a blood flow of 80 to 120 mL min^{-1}. oXiris is a membrane module made of modified AN69 hollow fiber membranes, which is used to remove cytokines and endotoxins. The module is operated like a dialyzer at a blood flow of 100 to 450 mL min^{-1} with a filtration capacity of $>$35 mL kg^{-1} h^{-1} for up to three consecutive days. The polyethylenimine-coated membranes adsorb and simultaneously dialyze and filtrate the blood. [Anka2018]

2.2 Triply Periodic Minimal Surfaces

Minimal surfaces, defined as those with the least area within a given boundary curve, can be exemplified by soap films spanning a closed wire frame. Submerging and pulling out the frame from a soap solution results in the formation of a soap film, spanning a minimal surface due to reduction of free energy. This phenomenon aligns with mathematical principles, where the surface exhibits zero mean curvature at each point. [Jaco2008]

Triply periodic minimal surfaces (TPMS) are a category of minimal surfaces, distinguished by their symmetrical properties and continuous connection within a three-dimensional space. Hermann Schwarz first identified these surfaces in 1865 [Schw1890], followed by Alan Schoen's empirical discovery of 12 new TPMS structures in 1970 [Scho1970]. These discoveries were later validated mathematically by Hermann Karcher in 1989 [Karc1989]. Among the most notable TPMS structures are the Schwarz Primitive (SP), Schwarz Diamond (SD), and Schoen Gyroid (SG) structures that are described mathematically by Equations 2.12 to 2.14 and shwon in Figure 2.7. These TPMS divide a volume with unit cell size s_{unit} into two distinct volumes. For $s_{off} = 0$ the two volumes are congruent, for $s_{off} \neq 0$ the surface shifts to form two unequal but still separate volumes. x, y, and z are the variables in the three dimensions (mm). [Hawk2023]

$$\text{SP: } s_{off} = \cos\left(\frac{2\pi x}{s_{unit}}\right) + \cos\left(\frac{2\pi y}{s_{unit}}\right) + \cos\left(\frac{2\pi z}{s_{unit}}\right) \tag{2.12}$$

$$\begin{aligned}\text{SD: } s_{off} = &\cos\left(\frac{2\pi x}{s_{unit}}\right) \cdot \cos\left(\frac{2\pi y}{s_{unit}}\right) \cdot \cos\left(\frac{2\pi z}{s_{unit}}\right) \\ &- \sin\left(\frac{2\pi x}{s_{unit}}\right) \cdot \sin\left(\frac{2\pi y}{s_{unit}}\right) \cdot \sin\left(\frac{2\pi z}{s_{unit}}\right)\end{aligned} \tag{2.13}$$

$$\begin{aligned}\text{SG: } s_{off} = &\sin\left(\frac{2\pi x}{s_{unit}}\right) \cdot \cos\left(\frac{2\pi y}{s_{unit}}\right) + \sin\left(\frac{2\pi y}{s_{unit}}\right) \cdot \cos\left(\frac{2\pi z}{s_{unit}}\right) \\ &+ \sin\left(\frac{2\pi z}{s_{unit}}\right) \cdot \cos\left(\frac{2\pi x}{s_{unit}}\right)\end{aligned} \tag{2.14}$$

Although a TPMS is a surface without volume, a 3D printer can be controlled to print solid material in one of the two volumes. This creates a single-phase structure. Alternatively, the printer can print the surface with a thickness s_{thick}, creating two independent channels (double-phase structure). Utilizing porous or conductive materials for the walls can facilitate heat or mass transfer between these channels.

Depending on the wall thickness t_{wall} and surface offset s_{off}, the porosity ϕ and channel size s_{chan} of the structure vary. The porosity is defined as the ratio of the free volume to the total volume of the unit cell $\phi = \frac{V_{free}}{V_{unit}}$. For single-phase TPMS with $s_{off} = 0$, this results in a porosity of 50 %. For two-phase TPMS, the total porosity is calculated as $\phi = \frac{V_{unit} - V_{wall}}{V_{unit}}$.

2.2.1 Anisometric TPMS Structures

Standard TPMS structures are uniform and periodic. However, the gradual distortion that creates an anisometric TPMS structure can add further features to the geometry. Distortion is possible in different ways. A change in wall thickness, for example, narrows the channel. The different extension of the unit cells in the three spatial directions distorts the geometry as shown in Figure 2.8. One of the greatest challenges is the uniform transition from one

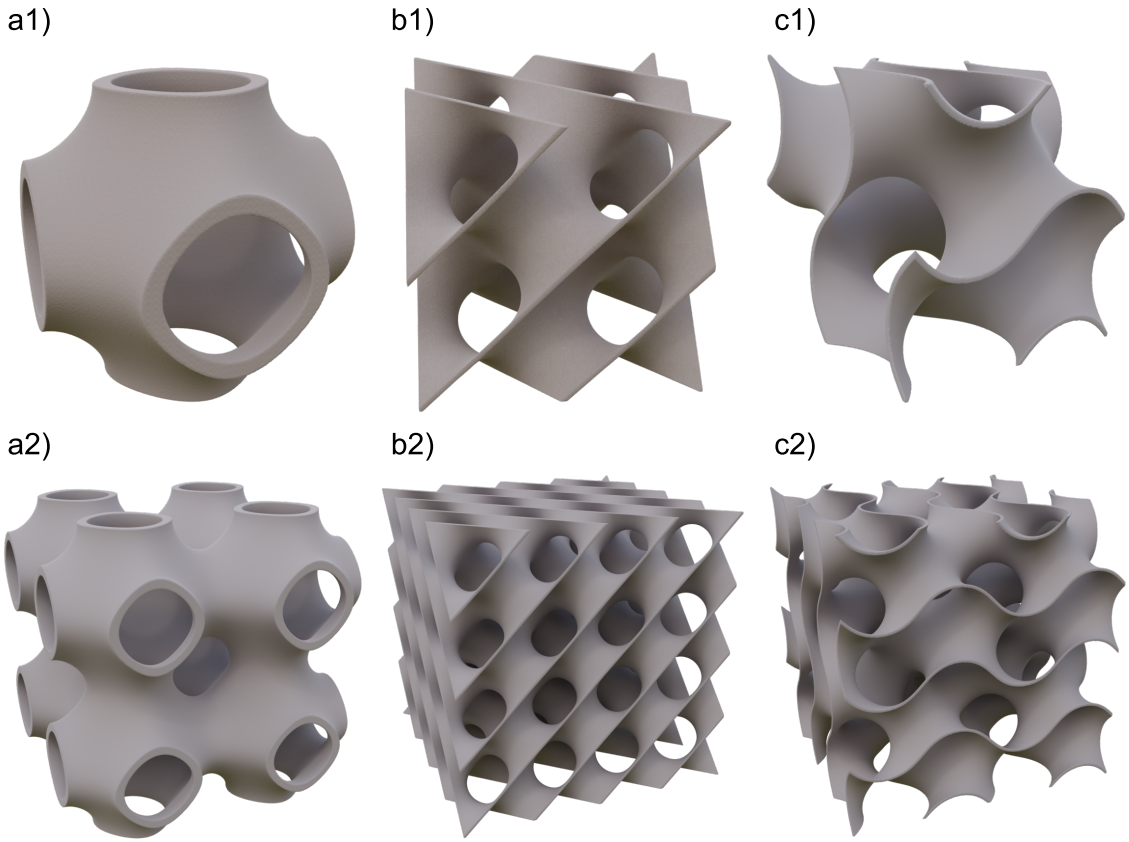

Figure 2.7: Two-phase triply periodic minimal surfaces (TPMS). The upper row shows single unit cells, the lower row shows 2x2x2 unit cells of the respective TPMS. a) Schwarz primitive, b) Schwarz diamond, c) Schoen gyroid.

unit cell to the next, for which various approaches and tools are available. [Tian2024]

2.2.2 Flow Through TPMS Structures

The flow through TPMS geometries is particularly relevant for this work. Due to the tortuous geometry, the fluid is deflected and secondary flows are created which reduce the formation of boundary layers. [Femm2015a; Femm2015b] To determine the flow regime in TPMS geometries, the Reynolds number from Equation 2.1 can be used. The hydraulic diameter can be used as the characteristic length which is given in Equation 2.15, where V is the fluid volume and A_{wet} is the wetted surface. [Hawk2023]

$$d_{hyd} = \frac{4 \cdot \phi \cdot V}{A_{wet}} \tag{2.15}$$

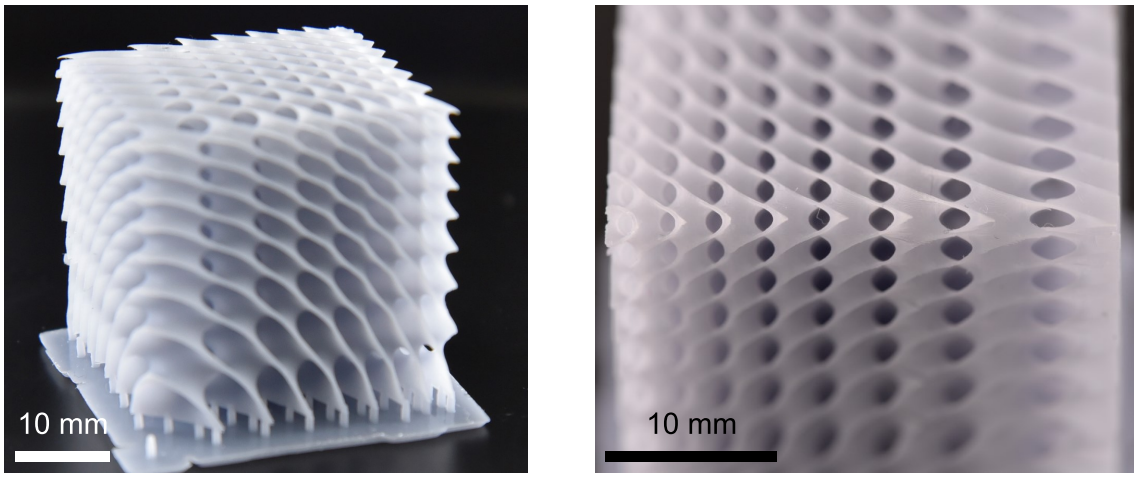

Figure 2.8: Anisometric Schwarz diamond triply periodic minimal surface structure with distorted unit cells.

There are still no exact Reynolds values for the transition from laminar to turbulent flow but Hawken et al. assume a transition between Re_{hyd} = 60 to 600. They also state, that flow in TPMS geometries is similar to flow through packed beds where $Re_{hyd} = 17, 250, 500$ are the transition points between creeping and laminar, laminar and transitional, and transitional and turbulent flow, respectively. [Hawk2023]

Flow Resistance of TPMS Structures

Asbai-Ghoudan et al. proposed an analytical correlation, Equation 2.16, for calculating the permeability κ as a function of the porosity ϕ and TPMS channel size s_{chan} [Asba2021]. However, the TPMS channel size is hardly measurable due to its variability and is not used as a parameter when creating a TPMS geometry. Therefore, it is proposed to use the TPMS unit cell size instead. Since they also found a linear relationship between the channel size and unit cell size, in Equation 2.16 s_{chan} can be substituted by a linear function $s_{chan}(s_{unit}) = m \cdot s_{unit} + b$, yielding Equation 2.17.

$$\kappa(\phi, s_{chan}) = (c_1\phi - c_2) \cdot s_{chan}^2 \tag{2.16}$$

$$\kappa(\phi, s_{unit}) = (c_3\phi - c_4) \cdot s_{unit}^2 + (c_5\phi - c_6) \cdot s_{unit} + c_7\phi + c_8 \tag{2.17}$$

c_1 to c_8 are constants depending on the TPMS type. For $\phi = 0$ and any value for s_{unit}, the permeability must be $0\,m^2$, whereby $c_8 = 0\,m^2$ applies.

2.3 Residence Time Distribution

In order to evaluate and optimize the flow distribution within an extracorporeal blood treatment device the residence time distribution (RTD) is a measure to identify channeling or stagnation. Computational fluid dynamics (CFD) simulations or experiments can visualize and quantify the RTD. For this purpose, a small amount of a detectable, non-reacting substance (tracer) is added to the flow upstream of the device and detected downstream. The concentration profile at the device's outlet yields the residence time density function $E(t)$, which is a fingerprint of the inhomogeneity of flow distribution inside the device. $E(t)$ has the unit of s^{-1}. The easiest to interpret are the pulse and step experiments, but the tracer can also be added periodically or randomly. Only non-reactive tracers and the pulse experiment are relevant for this work, which is why the others are not discussed further. The mean residence time τ (s) is calculated by dividing the fluid volume of the device by the volumetric flow rate as given in Equation 2.20. In the case of channeling, some fluid remains shorter ($< \tau$) in the device, while in domains of stagnant flow, parts of the fluid remain longer ($> \tau$) in the device. Ideally the RTD curve is narrow, symmetric, and a Gaussian-like distribution centered at the mean residence time. To compare different modules with each other, it is convenient that the area under the curve $E(t)$ is comparable and thus equals unity. This procedure is called normalization and yields the dimensionless RTD density function $E_\theta(\theta)$. [Leve1999]

2.3.1 The Pulse Experiment

In the pulse experiment, an amount of tracer n_{tracer} (mol) is added to the fluid flow with volumetric flow rate $\dot{V}$ ($m^3\,s^{-1}$) instantaneously at time $t_0 = 0\,s$ as shown in Figure 2.9. This tracer travels through the module and is detected at the output of the module as concentration $c(t)$ ($mol\,m^{-3}$). For modules

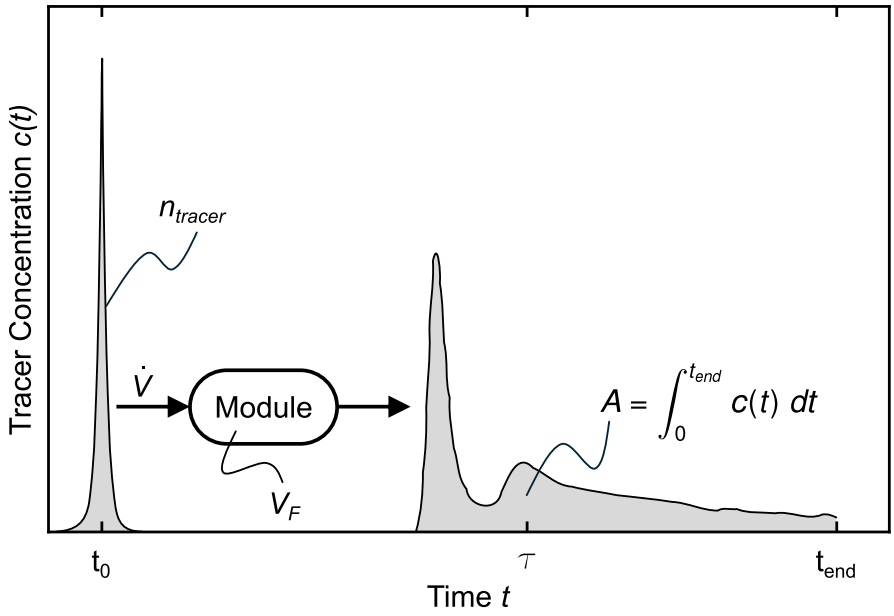

Figure 2.9: In the pulse experiment, an amount of tracer n_{tracer} is added to the fluid flow with volumetric flow rate $\dot{V}$ instantaneously at time t_0. The tracer travels through the module with volume V_F and is detected at the output as concentration $c(t)$ until the end of the experiment at t_{end}. τ is the mean residence time and A the area under the curve.

with closed boundary conditions the mass balance results in

$$\text{Area under } c(t) \text{ curve: } A = \int_0^{t_{end}} c(t)\, dt = \frac{n_{tracer}}{\dot{V}} \tag{2.18}$$

Thus, the RTD density function yields in

$$E(t) = \frac{c(t)}{A} = \frac{c(t)}{\int_0^{t_{end}} c(t)\, dt} = c(t)\frac{\dot{V}}{n_{tracer}} \tag{2.19}$$

In combination with Equations 2.29 and 2.30 the location, scale, and shape of $E(t)$ can be quantified. When dealing with differently sized modules, it is convenient to measure time in terms of dimensionless residence time θ (Equation 2.21) where τ is the mean residence time calculated from the

module's fluid volume V_F (m^3) and volumetric flow rate.

$$\tau = \frac{\int_0^{t_{end}} t\, c(t)\, dt}{\int_0^{t_{end}} c(t)\, dt} \cong \frac{\sum_i t_i\, c_i\, \Delta t_i}{\sum_i c_i\, \Delta t_i} = \frac{V_F}{\dot{V}} \tag{2.20}$$

$$\theta = \frac{t}{\tau} \tag{2.21}$$

Therefore, the dimensionless RTD density function is

$$E_\theta(\theta) = \tau \cdot E(t) \tag{2.22}$$

2.3.2 Statistical Moments or Distribution's Moments

The mathematical moments, also known as statistical moments, here related to the density function $E(t)$, are used to quantify the **location**, **scale**, and **shape** of a distribution. The first five moments are also known as the **total mass**, **mean**, **variance**, **skewness** and **kurtosis**. The generalized form of the kth moment around a non-random value o is:

$$\mathbb{E}\left[(X - o)^k\right] = \int_{-\infty}^{+\infty} (x - o)^k\, f(x)\, dx \tag{2.23}$$

Thus, statistical moments can be divided into three types: Raw moments, central moments and standardized moments. Raw moments refer to the zero point ($o = 0$), central moments refer to the mean of the distribution ($o = \mathbb{E}[X]$) and standardized moments are central moments normalized by the standard deviation raised to the power of k. For the present work, the RTD density function $E(t)$ over time t is considered with a mean of τ. This

results in

$$\text{Raw moments: } \mu_k = \mathbb{E}\left[(T)^k\right] = \int_0^{t_{end}} (t)^k \, E(t) \, dt \tag{2.24}$$

$$\text{Central moments: } m_k = \mathbb{E}\left[(T-\tau)^k\right] = \int_0^{t_{end}} (t-\tau)^k \, E(t) \, dt \tag{2.25}$$

$$\text{Standardized moments: } \widehat{m}_k = \frac{m_k}{\sigma_k} \tag{2.26}$$

$$\text{with } \sigma_k = \sigma_t^k = \left(\sqrt{m_2}\right)^k = \left(\sqrt{\int_0^{t_{end}} (t-\tau)^2 \, E(t) \, dt}\right)^k \tag{2.27}$$

Zeroth Moment - Total Mass

For the zeroth moment, the **total mass**, $\mu_0 = m_0 = \widehat{m}_0 = \int_0^{t_{end}} 1 \, E(t) \, dt = 1$ underlines that the distribution is normalized and equals unity. Figure 2.10 plots a probability density function using the normal distribution of form

$$f(t \mid \tau, \sigma) = \frac{1}{\sqrt{2\pi\sigma^2}} \cdot e^{-\frac{(t-\tau)^2}{2\sigma^2}} \tag{2.28}$$

with $\tau = 4$ and $\sigma = 1$. Due to the distribution being normalized, the area under the curve is $A = 1$.

First Moment - Mean

Because the first central moment and standardized moment equals 0, only the first raw moment is of interest, which is the expectation of T, also referred to as center of mass or **mean**, with

$$\mu_1 = \tau = \int_0^{t_{end}} t \, E(t) \, dt \tag{2.29}$$

Figure 2.10b plots a beta distribution with parameters $a = 2$ and $b = 5$ resulting in an expectation or mean of $\tau = \frac{a}{a+b} = \frac{2}{7} \approx 0.29$. Upon this value, the mass of the distribution is balanced.

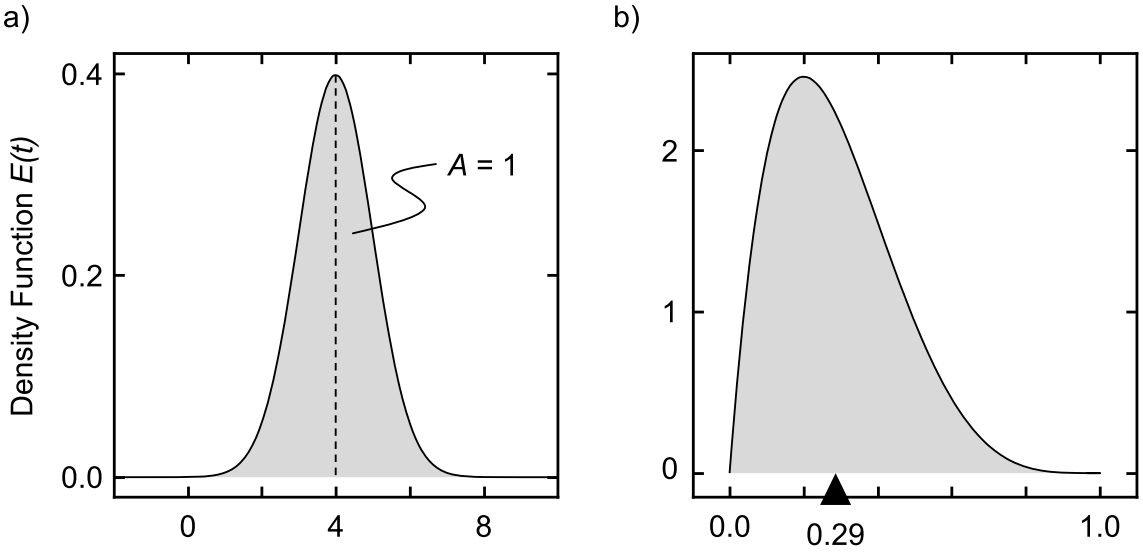

Figure 2.10: a) **Total Mass:** Probability density function using the normal distribution with parameters $\tau = 4$ and $\sigma = 1$. Due to the distribution being normalized, the zeroth raw, central, and standardized moments are all 1, thus the total mass or area of is $A = 1$. b) **Mean:** Probability density function using the beta distribution with parameters $a = 2$ and $b = 5$ resulting in an expectation or mean of $\tau = \frac{a}{a+b} = \frac{2}{7} \approx 0.29$. Upon this value, the mass of the distribution is balanced.

Second Moment - Variance

The second moment describes the **variance** $\mathbb{V}$ of the distribution. However, only the second central moment is relevant because it takes into account the mean of the distribution. The second standardized moment is 1 by definition. This results in the following for the variance, which describes the width of the distribution and is regularly expressed as σ^2:

$$m_2 = \mathbb{V} = \sigma^2 = \int_0^{t_{end}} (t - \tau)^2 \, E(t) \, dt \tag{2.30}$$

A higher variance represents a wider distribution, as visualized in Figure 2.11a, and a variance of 0 results in the expected value τ.

Third Moment - Skewness

The third moment, **skewness** $\mathbb{S}$, measures the length of the two tails below and above the expected value. The standardized third moment $\widehat{m}_3 = \mathbb{S} = \frac{m_3}{\sigma_3}$ measures the relative size by eliminating the location and size, making it

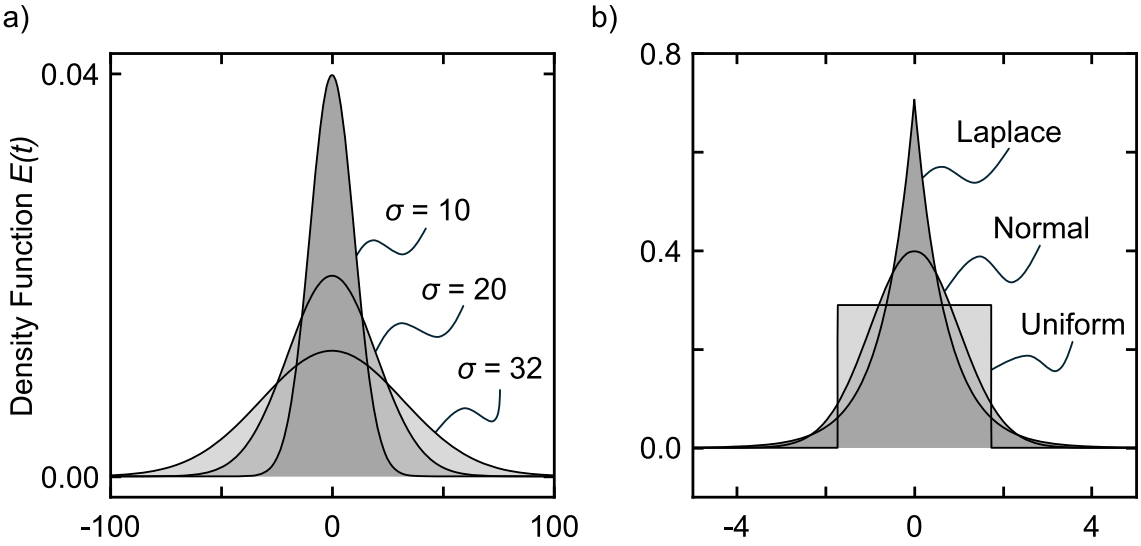

Figure 2.11: a) **Variance:** Probability density function using the normal distribution with parameters $\tau = 0$ and $\sigma = 10,\ 20$ and 32. A higher variance σ represents a wider distribution and a variance of 0 results in the expected value τ. b) **Kurtosis:** Probability density function using the Laplace, normal, and uniform distribution with mean 0 and variance 1. Their excess kurtosis ($\mathbb{K} - 3$) are 3, 0 and -1.2, respectively. Positive values mean that the distribution is more tailed than the normal distribution and negative values mean it is less tailed.

possible to compare different distributions with each other. For balanced tails, $\mathbb{S} = 0$. Figure 2.12 shows two distributions, one left-tailed (a) and one right-tailed (b). Values of $\mathbb{S}$ greater than 0 indicate a longer right tail and values less than 0 indicate a longer left tail. Skewness can therefore also be interpreted as tailedness. Many online sources describe the third moment as the asymmetry of a distribution. While a symmetrical distribution always has a skewness of 0, a skewness of 0 does not necessarily describe a symmetrical distribution.

Fourth Moment - Kurtosis

In comparison to the skewness, the fourth moment, **kurtosis** $\mathbb{K}$, considers the length of both tails together. The even exponent eliminates the sign, which means that $\mathbb{K}$ is always positive and long tails have a greater influence than short ones. The kurtosis of a normal distribution is 3, so one possible interpretation of the kurtosis is that it describes the tailedness of a distribution in relation to the normal distribution. $\mathbb{K} - 3$ is called "excess

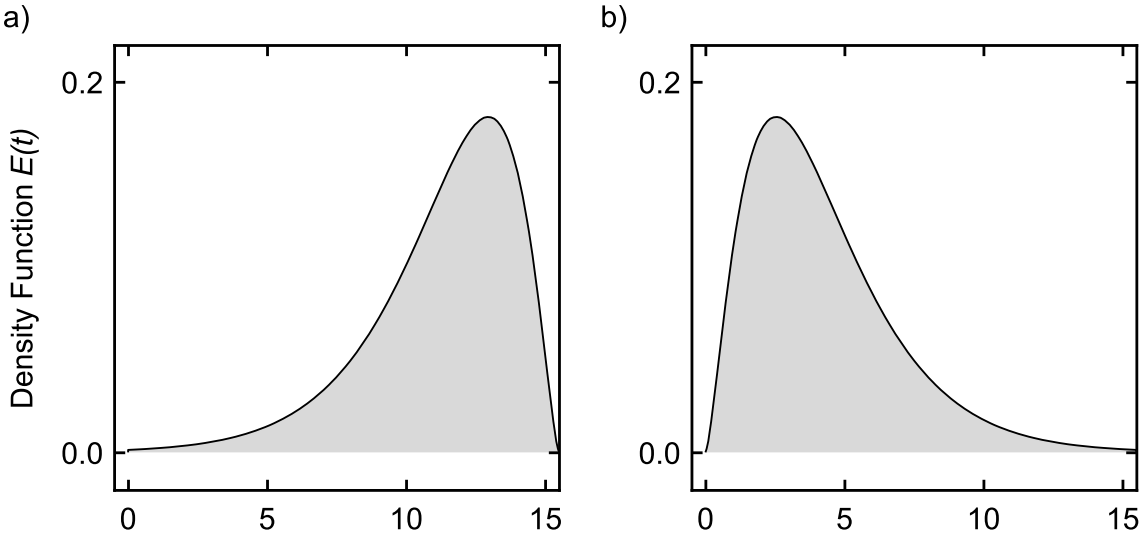

Figure 2.12: Skewness: a) Left-tailed distribution with $\mathbb{S} < 0$ and b) right-tailed distribution with $\mathbb{S} > 0$.

kurtosis", as for values greater than 3 a distribution is more tailed than the normal distribution and values smaller than 3 less. Figure 2.11b depicts a Laplace, normal, and uniform distribution with excess kurtosis of 3, 0 and -1.2, respectively.
[Gund2020]

2.3.3 Mirror-Image Analysis for Quantifying Symmetry

Mirror-image analysis is a method of quantifying the symmetry or asymmetry of any data. The method is mainly used in fields such as dentistry, orthodontics, and facial reconstructive surgery, but can also be applied to residence time distribution data. The calculation involves several steps. First, the mirror axis must be defined. Common axes are the mean or median of a distribution, but the maximum or any other axis can be used. The curve is divided along this axis to create two halves. One half of the curve is mirrored along the defined axis and placed on top of the other half. Both halves can now be compared. If both halves match, the distribution is symmetrical. The difference between the two halves is the asymmetry. This can be calculated in a variety of ways. For example, statistical methods or the area between the two halves of the curve. [Dams2011; Zhu2022; Wu2022]

2.4 Computational Fluid Dynamics

CFD is a discipline of fluid mechanics. It is the science in which fluid and gas flows are predicted using computers and numerical methods to iteratively and approximately solve mathematical equations. Compared to the analytical fluid mechanics, complex and non-linear sets of equations can be solved and compared to experimental fluid mechanics it is possible to investigate large setups or conditions outside the feasible at low cost and a lot less effort. In cfd the free flow and the interaction of the fluid with surrounding matter are calculated. As there are many different approaches to solving the fluid flow, for example smoothed-particle hydrodynamics (SPH) or the continuum approach, it is essential to select a method before the calculation. [Ansy; Baum2003]

2.4.1 Continuum Approach

The continuum approach considers fluids as continuous media. This means that the fluid properties (e.g., density, velocity, pressure) can be described using continuous functions. If the continuum approach is chosen, there are three essential steps:

1. Identification of the fluid domain for which the equations shall be solved.
2. Discretization of the domain and thus determination of the locations for which the equations shall be solved.
3. Determining the equations and boundary conditions to be solved that describe the fluid mechanics problem with sufficient accuracy.

[Ansy]

Fluid Domain

Usually there is a computer aided design (CAD) model of the geometry through which the fluid will flow, as shown in Figure 2.13a. For the first

step, the negative, i.e. the part that is later filled by the fluid, is extracted from this outer geometry as shown in Figure 2.13b.

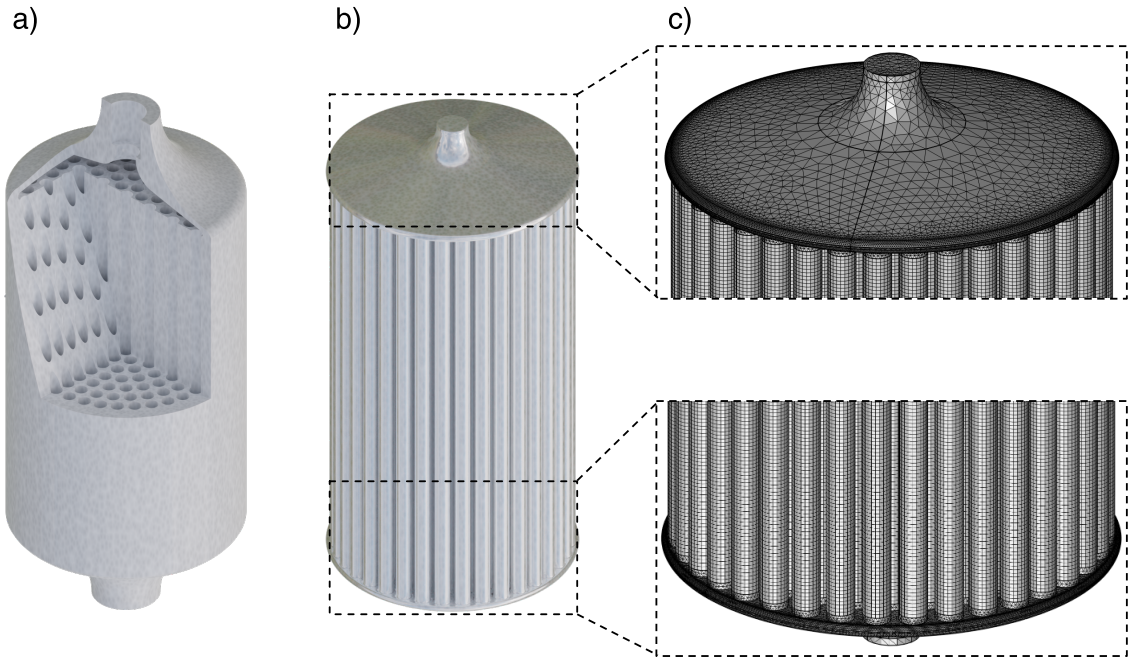

Figure 2.13: Identification and discretization of a fluid domain. a) CAD model of the outer geometry through which the fluid will flow. b) Negative of the geometry representing the fluid volume. c) Discretization of the fluid volume into finite volume elements. The top and bottom of the geometry were discretized into tetrahedrons, while the center part (tubes) were discretized into hexahedrons.

Discretization

In the second step, this fluid volume is discretized, visualized with the help of the mesh elements shown in Figure 2.13c. Discretization means transferring the continuous functions to the discrete locations of a computational grid with the aim of obtaining a linear system of equations and solving it numerically. Discretization causes the system to lose accuracy (an error occurs), however, only then does it become solvable. The most common discretization methods are the finite difference (FD), finite element (FE), and finite volume (FV) methods. [Baum2003]

Finite Difference Method Using the FD method, a grid of discrete points is generated and the derivatives of the partial differential equations are ap-

proximated at these points by difference equations. Considerable continuity defects can arise with this method. [Baum2003; Roll2005]

Finite Element Method The FE method divides the domain into smaller, non-overlapping elements (e.g. triangles, cuboids, tetrahedrons). The corner points of the elements form the so-called nodes for which solutions are calculated. Between two neighboring nodes, the partial differential equations are replaced by simple continuous functions (e.g. polynomials), thus converting the non-linear system of equations into a linear one. In comparison to the FD method, the continuity between neighboring nodes is thus maintained. [Baum2003; Roll2005]

Finite Volume Method The third and most frequently used method, the FV method, divides the domain into smaller control volumes. The partial differential equations are applied to each control volume to ensure that the conservation principle applies, i.e. nothing can emerge or disappear within the control volume. For each control volume, the differential equations are integrated and converted into surface integrals in order to calculate a flow across the boundaries. The calculated final value corresponds to the mean value of the control volume. This method can be used to analyze any geometry without problems with high gradients (discontinuities). [Baum2003; Roll2005]

Fundamental Equations

The movement of a fluid follows some general conservation laws: conservation of mass and conservation of momentum. The general conservation of a property states that the change of this property within a control volume is equal to the amount entering and leaving across the boundaries plus the amount created and consumed in the volume. In case of chemical reactions the conservation of species, stating that each single component must be preserved, is added. [Baum2003] For heat transfer, the conservation of energy is used. However, for the fluid flow investigated in this thesis, only

the conservation of mass and conservation of momentum are sufficient because no chemical reactions or heat transfer have been investigated. In Chapter 3 and 5, a tracer species is added to the fluid flow. Therefore, an additional transport equation describing the concentration of the species is needed.

Conservation of Mass The conservation of mass without any sources or sinks is:

$$\frac{\delta \rho}{\delta t} + \nabla \cdot (\rho v) = 0 \tag{2.31}$$

where ρ is the density, t is the time, v is the flow velocity, and $\nabla\cdot$ is the divergence of a vector field, indicating the partial derivations along all dimensions $(\frac{\delta}{\delta x_1}, ..., \frac{\delta}{\delta x_n})$. For an incompressible fluid ($\rho = const.$), such as water or blood, Equation 2.31 simplifies to $\nabla \cdot v = 0$. [Ansy]

Conservation of Momentum The conservation of momentum follows Newton's second law $F = ma$. Here, F are all external forces acting on a body that equal to the product of mass m times acceleration a. For fluid flow this results in Equation 2.32. The external forces can be split into two terms, one to describe internal stresses and one for external forces, such as gravity g (Equation 2.33).

$$F = \rho \left(\frac{\delta v}{\delta t} + v \cdot \nabla v \right) \tag{2.32}$$

$$\nabla \cdot \sigma + g = \rho \left(\frac{\delta v}{\delta t} + v \cdot \nabla v \right) \tag{2.33}$$

$$-\nabla P + \nabla \cdot \tau + g = \rho \left(\frac{\delta v}{\delta t} + v \cdot \nabla v \right) \tag{2.34}$$

Here, σ is the Cauchy stress tensor composed of normal stresses (σ_{xx}, σ_{yy}, σ_{zz}) and shear stresses τ. Mechanical pressure P, a relevant parameter in CFD, is equal to the negative of the mean normal stress, yielding Equation 2.34. For Newtonian fluids the viscosity η can be related to the viscous term $\nabla \cdot \tau = \eta \nabla^2 v$, while for non-Newtonian fluids, such as blood, the vis-

cosity is a function of the shear rate as explained in Section 2.4.2. [Ansy; Baum2003; Hosc2024]

Transport Equation for Diluted Species In case of a diluted species only fluid-species interaction are considered, thus the species itself has no impact back on the fluid. Therefore, first the fluid equations can be solved and then the advection and diffusion of the species are calculated. The species transport equation follows the general conservation equation and, in case of no sources or sinks, is given in Equation 2.35:

$$\frac{\delta c}{\delta t} + \nabla (vc - D\nabla c) = 0 \tag{2.35}$$

where D is the diffusion coefficient and c is the species' concentration. In this equation the vc term accounts for advective transport and the $D\nabla c$ term considers diffusion of the species. [Haut2020]

Navier-Stokes Equations for Incompressible Fluid The final Navier-Stokes equations for an incompressible fluid with non-Newtonian viscosity and coupling to the transport of diluted species with constant diffusion coefficient are:

$$\begin{aligned}
\text{Continuity:}\quad & \nabla \cdot v = 0 \\
\text{Momentum:}\quad & -\nabla P + \nabla \cdot \left[\eta(\dot{\gamma})(\nabla v + (\nabla v)^T)\right] + g = \rho\left(\frac{\delta v}{\delta t} + v \cdot \nabla v\right) \\
\text{Transport:}\quad & \frac{\delta c}{\delta t} + v \cdot \nabla c - D\nabla^2 c = 0
\end{aligned}$$

2.4.2 Simulation of Blood

The simulation of flowing blood through arbitrary geometries has enormous advantages, especially since blood is a very precious liquid. However, not all blood is the same, because blood is a composition of many components as described in Section 2.1.1. Different compositions lead to different rheological properties, which are crucial for simulations. In addition, there is the

non-linear dependency of the rheological parameters on external influences such as flow velocity or shear rate. [Freu2014; Fuch2023]

Simple approximations use a constant density and viscosity. For a more accurate calculation, especially when considering shear rates, the shear-thinning properties of blood should be taken into account by using a non-linear model. A common model is the Carreau-Yasuda model, as described in Equation 2.36. The viscosity η (Pa s) is a function of the shear rate $\dot{\gamma}$ (s^{-1}) and is calculated from the viscosity without shear rate η_0, the viscosity at infinite shear rate η_∞, the relaxation time λ (s), the power law index n, and the dimensionless parameter a. [Seeh2023; Boyd2007]

$$\eta(\dot{\gamma}) = \eta_\infty + (\eta_0 - \eta_\infty)\left[1 + (\lambda \cdot \dot{\gamma})^a\right]^{\frac{n-1}{a}} \tag{2.36}$$

2.4.3 Computational Optimization

The aim of optimization is to find an optimum state. In the case of simulations and computer-aided calculations, statistical models aid in covering an arbitrary parameter space that would be almost impossible to access manually or experimentally.

The problem to be optimized is treated as a black box with input and output parameters. The aim of optimization is to establish a connection between these input and output parameters in the parameter space to find the best possible state, the global optimum. Depending on the complexity of the model, there may be no clear solution or there may be several optima, either global or local. The output parameter is calculated from an initial value. Based on the result, a function without a specific form is created as a relationship between the input and output parameters. An acquisition function evaluates the result and determines the next point to be examined, whereby a trade-off is made between exploration and exploitation. [McCa2023]

Single and Multi-Objective Optimization

Single-objective optimization reduces the problem to a single output parameter, which is maximized or minimized and thus specifies the optimum. As there are usually several output parameters, it is essential to combine them into one value. Various weighting functions are available for this purpose, such as the weighted, geometric, arithmetic or harmonic mean. With multi-objective optimization, the output parameters are considered as a whole. Each iteration examines whether and to what extent an output parameter changes without the other parameters worsening too much. [McCa2023; Brad2018]

2

3.

Simulative and Experimental Flow Analysis of Blood Contactors

Parts of this chapter have been published as:
Lukas T. Hirschwald, Franziska Hagemann, Maik Biermann, Paul Hanßen, Patrick Hoffmann, Tim Höhs, Florian Neuhaus, Maerthe Theresa Tillmann, Petar Peric, Maximilian Wattenberg, Maik Stille, Tamara Fechter, Alexander Theißen, Patrick Winnersbach, Kai P. Barbian, Sebastian V. Jansen, Ulrich Steinseifer, Bettina Wiegmann, Rolf Rossaint, Matthias Wessling, Christian Bleilevens, John Linkhorst
Enhanced Hemodynamics of Anisometric TPMS Topology Reduce Blood Clotting in 3D Printed Blood Contactors, Advanced Healthcare Materials, 2024
DOI: 10.1002/adhm.202403111

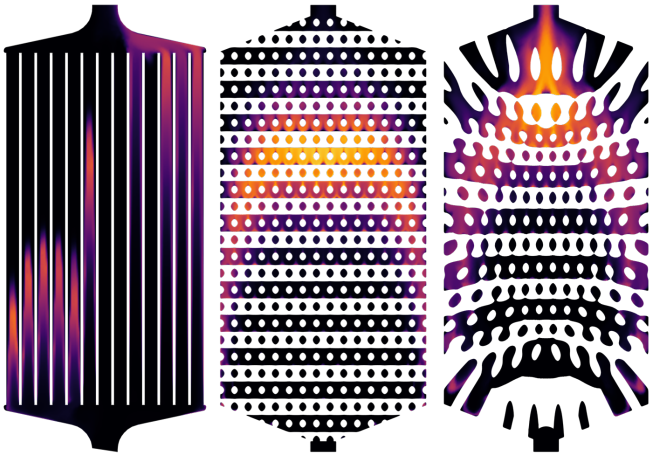

3.1 Introduction

Non-physiological flows and high shear rates in extracorporeal blood treatment devices lead to unexploited potential and increased risk of thrombosis. It is important to utilize the entire functional surface of the devices evenly to minimize the residence time of the blood in the device, as the artificial surfaces cause rejection reactions.

Current dialyzers and fiber-based hemoadsorbers suffer from poor radial blood distribution in the inlet area [Ronc2002; Kim2009; Hira2012]. Cylindrical hemoadsorbers with porous polymer beads also exhibit different residence times for blood in the peripheral areas compared to blood along the central axis [Umat2019]. Although membrane lungs exist in different shapes, they do not achieve homogeneous blood distribution [Hess2022]. Furthermore, too high or too low shear rates can lead to activation of the coagulation cascade and thus to the formation of blood clots [Feau2023; Casa2015].

In this chapter, four modules with different inner geometries were created. Triply periodic minimal surface (TPMS) structures were used to improve the flow distribution [Hess2021; Hess2022]. This novel geometry for blood treatment devices was simulatively analyzed with regard to its hemodynamics in order to be able to make a comparison with state-of-the-art devices. Furthermore, the analysis allows conclusions about regions with an potentially increased risk of blood clot formation.

3.2 Materials and Methods

Four modules, each with a distinct inner geometry but identical fluid volumes of 25 mL, were designed, manufactured, and tested. These modules are illustrated in Figure 3.1. Notably, the "isoTPMS smaller" module features smaller unit cells, which result in a larger inner surface area.

3.2.1 Computer-Aided Design of Blood Contactor Modules

Tubular Module (tubular)

The tubular module, created using Autodesk Inventor (version 2023, Autodesk Inc., USA), features an inner diameter of 32 mm and a length of 84 mm. Inside, it includes 127 straight tubes, each 2 mm in diameter and 55 mm long, resulting in a total volume of 21.9 mL and a surface area of 438.9 cm^2. Additionally, two end caps fit onto the tube section as distributors, each with a volume of 1.6 mL and an inner surface area of 12.7 cm^2, designed to accommodate a 4 mm $\times$ 6 mm tube (inner x outer diameter). The combined volume of the module is 25.0 mL, and the total inner surface area is 464.3 cm^2, leading to a surface area to volume ratio (SAV) of 1.85 mm^{-1}.

Isometric TPMS Module (isoTPMS)

The isometric TPMS modules, designed using nTop (Version 4.8.2, nTopology Inc., USA), share the same dimensions as the tubular module and are configured to fit identical tubes. The TPMS structure is rotated by 45° around the x-axis and then by $\arctan(1/\sqrt{2}) = 35.3°$ around the y-axis to optimize flow through its unit cells along the space diagonal. Two versions were developed:

- One version matches the tubular and anisoTPMS modules in surface area and volume, using unit cells sized 4.27 mm $\times$ 4.27 mm $\times$ 4.27 mm with a mid-surface offset of -0.045 mm, and shifted -5.3 mm along the z-axis.
- The second version has a larger surface area, consisting of unit cells sized 3 mm $\times$ 3 mm $\times$ 3 mm with a mid-surface offset of -0.031 mm, shifted 5.6 mm along the z-axis. It has a volume of 25.0 mL and a larger inner surface area of 644.3 cm^2, yielding an SAV of 2.58 mm^{-1}.

Anisometric TPMS Module (anisoTPMS)

The anisometric TPMS module (anisoTPMS), also designed in nTop, maintains the same dimensions as the isoTPMS module but uses distorted Schwarz di-

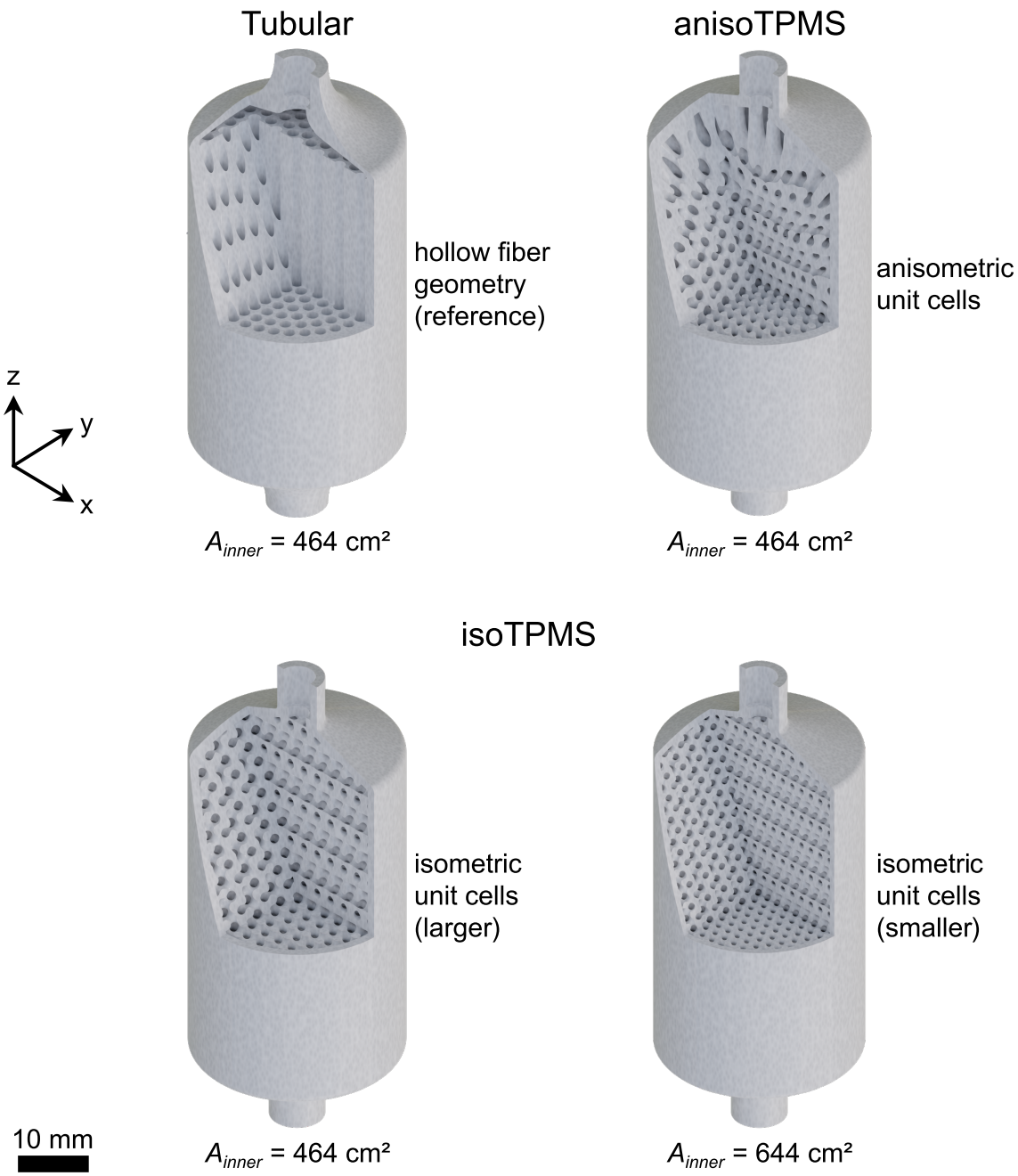

Figure 3.1: Illustration of four module types: tubular, anisoTPMS, and isoTPMS with larger and smaller unit cells. The tubular module serves as a reference. The anisoTPMS module is designed to facilitate smoother transitions from the inlet to the core of the module, while the isoTPMS modules feature simpler, anisometric TPMS structures.

amond TPMS unit cells. These cells are configured with a base size of 8.95 mm × 8.95 mm × 8.95 mm and a mid-surface offset of −0.064 mm. They were generated using the *Warp Cell Map* block inside the *Periodic Lattice* block.

3.2.2 Computational Fluid Dynamic Simulations

The computational fluid dynamics (CFD) software COMSOL Multiphysics (Version 6.1, COMSOL AB, Sweden), including the *CAD Import Module*, *CFD Module*, and *Chemical Reaction Engineering Module*, was utilized. These simulations of the blood contactors were conducted in 3D space using their inverse geometry, which represents the fluid-containing volume.

Import and Meshing

For the tubular module, the inverse geometries of the individual parts were constructed by subtraction, followed by the creation of a derived part that formed a unified body. This module was integrated via geometry import. At the module's in and outlet cap and at the end face of the tubes, a *free tetrahedral* mesh was applied. The tubes themselves were meshed using a *swept* mesh in the axial direction with 200 elements.

Similarly, the inverse geometries for the isoTPMS and anisoTPMS modules were assembled by subtraction and meshed using the *Mesh from Implicit Body* block with a tolerance of 0.1 mm. A subsequent remeshing step with the *Remesh Surface* block was necessary to decrease the element count, remove artifacts, and facilitate domain generation in COMSOL. The specific meshing parameters are detailed in Table 3.1. The STL files for both the isoTPMS and anisoTPMS modules were imported into COMSOL, where a *free tetrahedral* mesh was applied to each.

Study Setup and Fluid Properties

Velocity profiles and shear rates were simulated with a stationary study of laminar fluid flow. At the module's inlet a fully developed flow with a flow rate of 300 mL min^{-1} was set.

Water Properties for Residence Time Distribution The fluid had a density of 1000 kg m^{-3}, and a Newtonian viscosity of 1 mPa s. Additionally, a time-dependent study with the *transport of diluted species* physics was used to simulate

Table 3.1: Meshing parameters in nTop for isoTPMS and anisoTPMS for CFD simulations.

Mesh from Implicit Body (isoTPMS)	
Body	isoTPMS
Tolerance	0.1 mm
Min. feature size	-
Sharpen	no
Simplify	no

Mesh from Implicit Body (anisoTPMS)	
Body	anisoTPMS
Tolerance	0.1 mm
Min. feature size	-
Sharpen	no
Simplify	no

Remesh Surface (isoTPMS)	
Surface	Mesh for CFD
Edge length	0.2 mm
Shape	Triangle
Span angle	15 deg
Growth rate	2
Feature angle	30 deg
Min edge length	0.01 mm
Chord height	
Min feature size	0.05 mm

Remesh Surface (anisoTPMS)	
Surface	Mesh for CFD
Edge length	0.2 mm
Shape	Triangle
Span angle	15 deg
Growth rate	2
Feature angle	30 deg
Min edge length	0.05 mm
Chord height	
Min feature size	0.05 mm

the residence time distribution (RTD). This time-dependent simulation ran in 0.1 s increments over a period of 15 s. The tracer was injected via a rectangular function between 0 to 0.1 s with an amplitude of 1 mol m^{-3} and a diffusion coefficient of $1 \cdot 10^{-9}$ m^2 s^{-1}.

Blood Properties for Hydrodynamic Evaluation The fluid had a density of 1050 kg m^{-3}, and its viscosity was set according to the inelastic non-Newtonian Carreau-Yasuda model given in Equation 2.36 with parameters from Seehanam et al. [Seeh2023]:

infinite shear viscosity: $\mu_\infty = 0.0035$ Pa s

zero shear viscosity: $\mu_0 = 0.25$ Pa s

relaxation time: $\lambda = 69.1$ s

power law index: $n = 0.3621$

transition parameter: $a = 2$

3.2.3 Experimental Setup for Residence Time Distribution Measurement

Additive Manufacturing and Preparation

All modules were produced using a Phrozen Sonic Mini 8K printer (Phrozen Technology, Taiwan) via digital light processing additive manufacturing, utilizing hemocompatible resin (Printodent GR-20 MJF, pro3dure medical GmbH, Germany). The STL files were prepared using Chitubox Basic (Version 1.9.4, Chitubox, China), with printing parameters detailed in Table 3.2. After printing, the modules were detached from the platform and cleansed in isopropyl alcohol (70 % in H_2O, Sigma-Aldrich Chemie GmbH, Germany) using a Form Wash (Formlabs Inc., USA). Further rinsing involved flushing the interior with pure isopropyl alcohol (>99.8 %, EMSURE ACS reagent, Sigma-Aldrich Chemie GmbH, Germany) using a 50 mL syringe attached to 4 mm × 6 mm tubing. Subsequent to washing, the modules were dried using compressed air and then aired in a fume hood for a minimum of 1 h. Postcuring was conducted overnight in a homemade light chamber lined with aluminum foil and illuminated by two energy-saving lightbulbs (each 25 W, 1400 lm, daylight), ensuring complete polymerization of the material. Lastly, two 8 cm pieces of tubing (Class VI, 1/8 x 1/16 S DEHP free, from CAPIOX FX05 set, Terumo Europe N.V., Belgium) were glued to the module (UHU Plus Sofortfest, UHU GmbH, Germany).

Each module was equipped with two 8 cm pieces of tubing (Class VI, 1/8 x 1/16 S DEHP free, from CAPIOX FX05 set, Terumo Europe N.V., Belgium). These were glued to the module (UHU Plus Sofortfest, UHU GmbH, Germany).

Residence Time Distribution Measurement

To experimentally determine the RTD, the setup depicted in Figure 3.2 was employed. This configuration included a peristaltic pump (Pumpdrive 5206, Heidolph Instruments GmbH, Germany), with the flow rate managed by a volumetric flow sensor (Sonoflow CO.55/0250 V3.0, Sonotec GmbH, Germany) and set at 300 mL min^{-1}. The injection loop comprised four three-way stopcocks (Discofix C, Ref 16494C, B. Braun SE, Germany) and had a total volume of 4 mL due to the tubing used, which featured an inner diameter of 4 mm. All experiments were conducted at room temperature.

Prior to each experiment, the injection loop was filled with a tracer solution consisting of 400 mg L^{-1} Ponceau S dye (P3504, Sigma-Aldrich Chemie GmbH, Ger-

Table 3.2: Printing parameters for Printodent GR-20 MJF resin on a Phrozen Sonic Mini 8K 3D printer.

Parameter	Value
Layer Height	0.05 mm
Bottom Layer Count	6
Exposure Time	9.0 s
Bottom Exposure Time	50.0 s
Transition Layer Count	6
Transition Type	Linear
Transition Time Decrement	5.86 s
Waiting Mode During Printing	Resting Time
Rest Time Before Lift	0.0 s
Rest Time After Lift	0.0 s
Rest Time After Retract	2.0 s
Bottom Lift Distance	6.0 mm + 0.0 mm
Lifting Distance	6.0 mm + 0.0 mm
Bottom Retract Distance	6.0 mm + 0.0 mm
Retract Distance	6.0 mm + 0.0 mm
Bottom Lift Speed	60.0 mm min^{-1} & 0.0 mm min^{-1}
Lifting Speed	60.0 mm min^{-1} & 0.0 mm min^{-1}
Bottom Retract Speed	150.0 mm min^{-1} & 0.0 mm min^{-1}
Retract Speed	150.0 mm min^{-1} & 0.0 mm min^{-1}

many) dissolved in water. Initially, the upper three-way stopcocks were positioned to bypass the injection loop, allowing the water to flow directly into the module. To initiate the RTD measurement, both stopcocks were simultaneously turned to direct the water through all four stopcocks, thereby introducing the tracer solution into the module. Tracer detection was performed using an RGB color sensor board (TCS3200 evaluation board with four white LEDs, AZ-Delivery Vertriebs GmbH, Germany). The sensor's output voltage was converted to RGB data by a microcontroller (Arduino Uno Rev3, Arduino S.r.l., Italy), with only the green color values utilized for data analysis due to their higher amplitude. To ensure no external light affected the measurements, the sensor was housed inside a white-covered box, which was then placed within another black box. Given the extra-column volume was minimal relative to the module's volume, it was considered negligible for the RTD analysis.

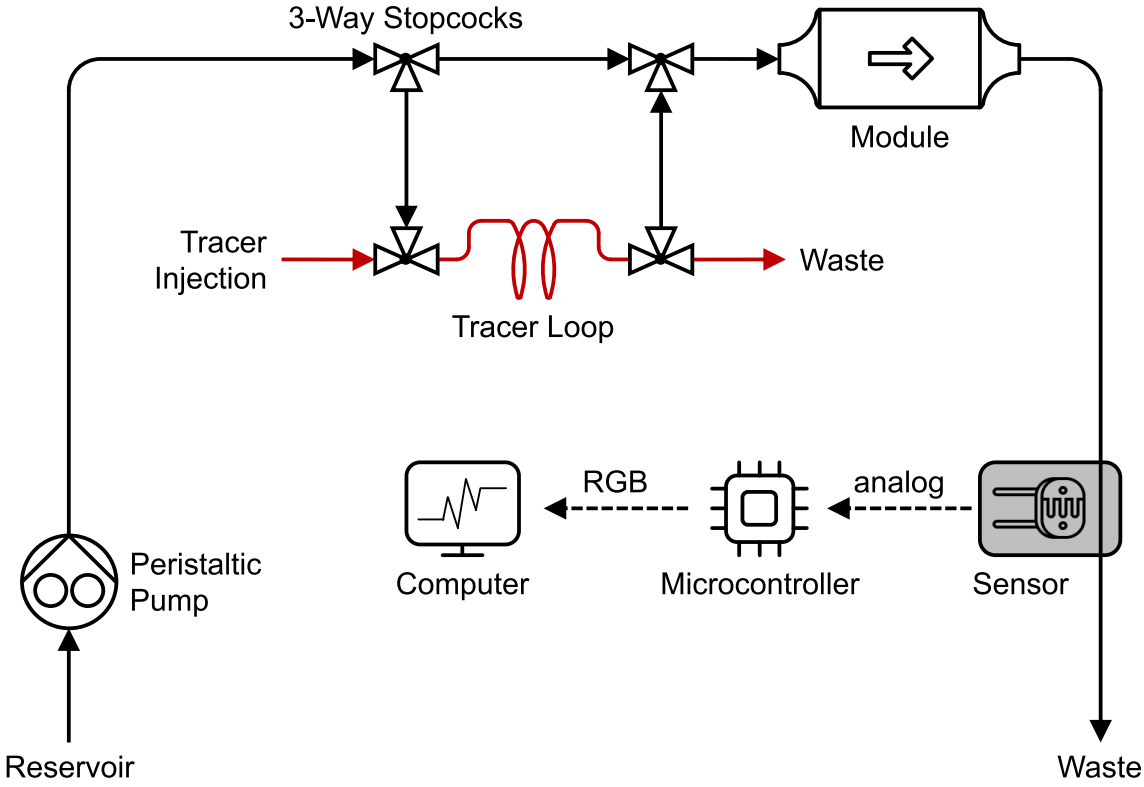

Figure 3.2: Experimental setup for determining the RTD. A peristaltic pump pumps water through the module. Initially, the water bypasses the injection loop for priming. For tracer injection, the three-way stopcocks are adjusted to divert the flow through the injection loop. Post-module, a color sensor captures RGB values, which a microcontroller converts and sends to a computer for analysis.

3.3 Results and Discussion

Four modules were developed to explore the hydrodynamic properties of TPMS structures. Each module retained the same outer geometry and fluid volume but varied in inner geometry. The tubular module, consisting of straight tubes, served as the reference structure. The TPMS modules are subdivided into isometric and anisometric, with two different unit cell sizes examined within the isometric category.

A blood viscosity model was used to simulate the flow, enabling detailed examination of hydrodynamic features, such as identifying stagnation zones or regions with significant shear rate variations. To validate these simulations, experimental measurements of the residence time distribution were compared with simulations of time-dependent tracer transport.

3.3.1 Validation of the Simulation Model through Experimental Residence Time Distribution Measurements

The simulation model was validated using water, which in the simulation corresponds to a Newtonian viscosity of 0.001 Pa s and a density of 1000 kg m^{-3}. Experimentally, deionized water at room temperature was utilized, employing the setup illustrated in Figure 3.2.

Tubular Module

The simulated and experimental RTD curves for the tubular module with ideal straight inflow are depicted in Figure 3.3. Generally, both curves follow the same trend, featuring a higher and sharper primary peak followed by a smaller and broader secondary peak. However, the simulated curve displays three peaks due to the separation of the initial peak. Furthermore, while the second peaks in both the simulation and experiment align closely in height and shape, the first experimental peak appears approximately 1.5 s later, is lower, and is slightly broader than its simulated counterpart.

The division of the tracer into two principal fractions is attributable to varying flow velocities within the tubes. The central tubes exhibited higher velocities and thus the tracer is transported faster, whereas the outer tubes conveyed the tracer more

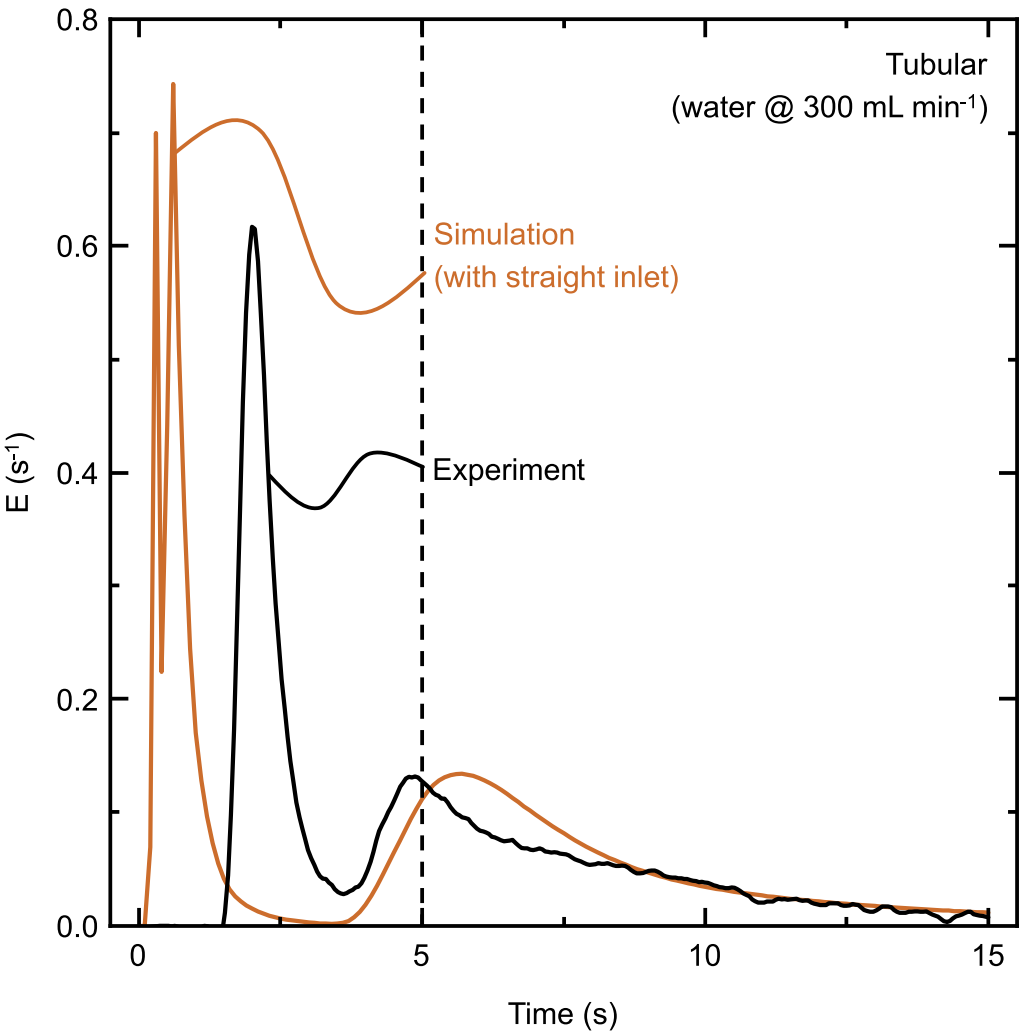

Figure 3.3: Simulative and experimental RTD for the tubular module. The simulation employed an ideal straight inflow. However, the experimental results may contain deviations due to potential bending of the inlet tube or manual operation of the setup. At 5 s the dashed line marks the mean residence time τ.

slowly. This tracer variation is illustrated in the cross-sectional images of the XZ and YZ planes, shown in Figure 3.4. The left images, captured at 0.2 s, highlight how the central tubes carry a significant portion of the tracer, corresponding to the first peak. From the YZ plane image, it is evident that the tracer is distributed between the central tube and its surrounding ring of six tubes, which accounts for the division of the first peak. The right images, captured at 3.0 s, correspond to the second peak. Given that the areas under both peaks are similar, it is concluded that the seven central tubes transported the same amount of tracer as the remaining 119 tubes.

In the experimental setup, three-way stopcocks were utilized to create an in-

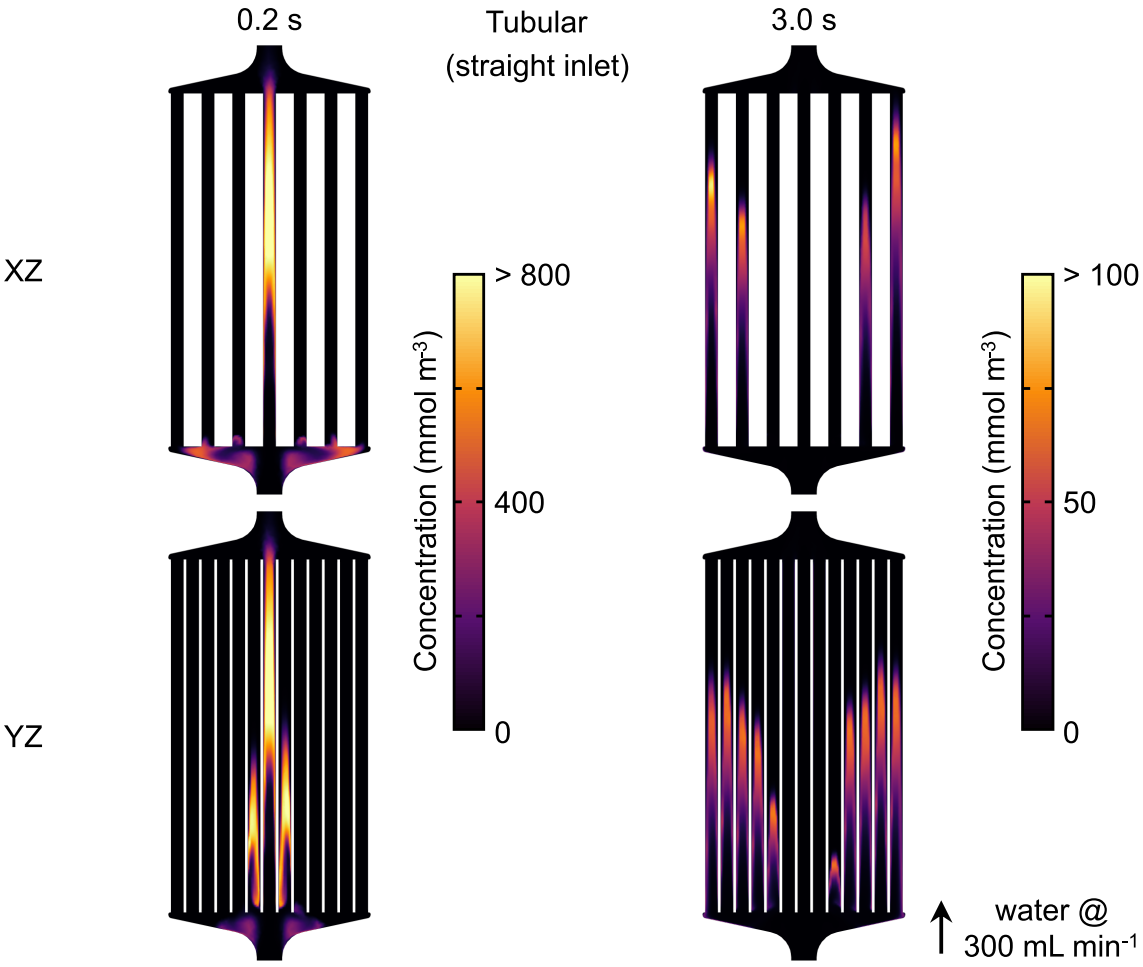

Figure 3.4: Cross-sectional images of the tubular module at 0.2 s and 3.0 s, showcasing the simulated tracer passage. To improve the visibility of tracer concentrations, distinct color bars were applied: the 0.2 s images utilize a range from 0 to 800 mmol m^{-3}, whereas the 3.0 s images cover a range from 0 to 100 mmol m^{-3}.

jection loop, which was operated manually. Due to this manual operation, timing discrepancies are possible. Additionally, an inclined position of the tube at the inlet or a bend in the tube could cause the flow not to enter the module in a perfectly straight path, leading to an angled inflow that distributes the fluid across multiple tubes instead of aligning with the central tube. To investigate these possibilities, a simulation of the tubular module with an angled inlet was performed. The RTD curve from this simulation is displayed in Figure 3.5. The characteristic shape of a sharper first peak followed by a broader second peak remains, but the first peak does not split into two. Adjusting the experimental curve by -1.5 s to compensate for potential manual timing errors shows that both curves align closely.

Figure 3.6 presents section views of the tubular module with the angled inlet. The images captured at 0.2 s clearly demonstrate the impact of the non-ideal inflow.

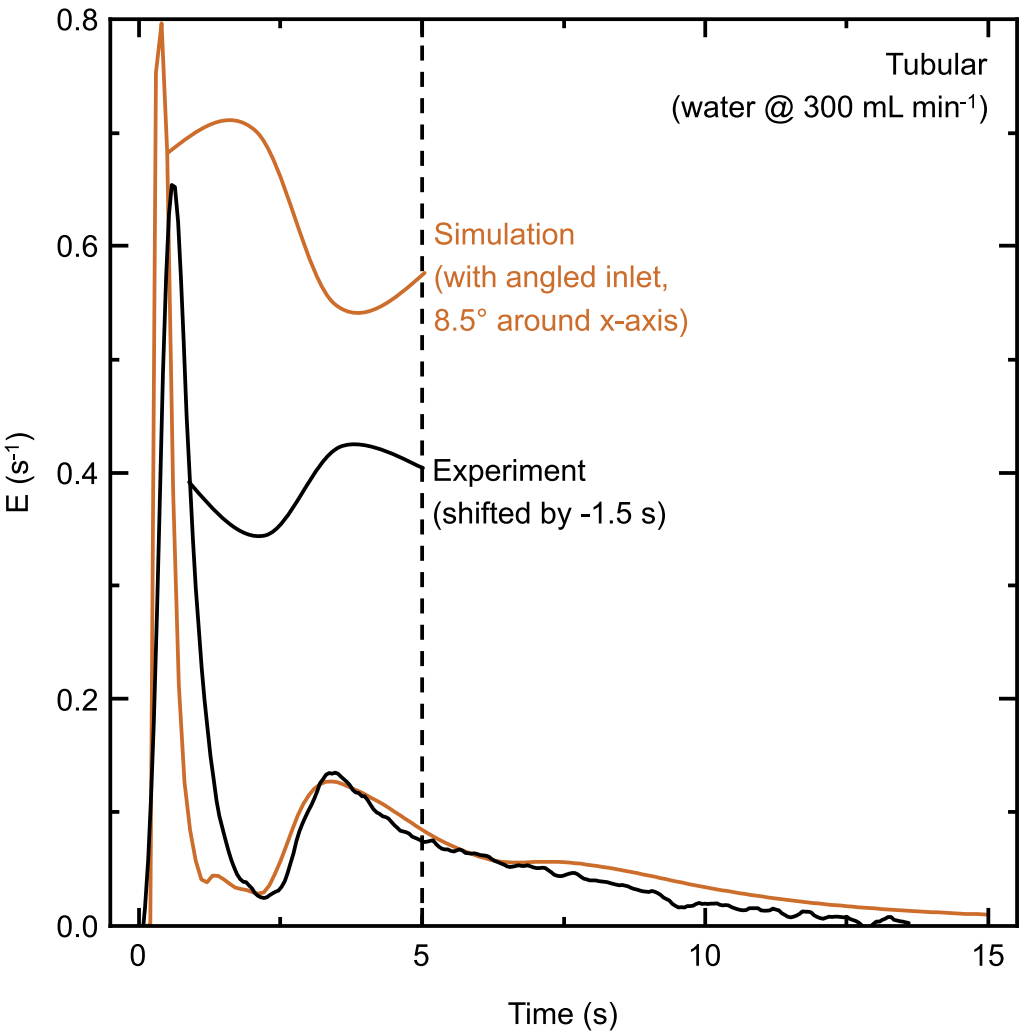

Figure 3.5: Simulative and experimental RTD for the tubular module, with the inlet face rotated by 8.5° around the X-axis to replicate potential deviations caused by a bent tube in the experimental setup. This specific angle was chosen arbitrarily to demonstrate the effects of such experimental variations. Moreover, the experimental curve in the graph was shifted by -1.5 s to synchronize the start times of both curves, emphasizing the similarity in their shapes. At 5 s the dashed line marks the mean residence time τ.

Unlike the uniform entry of the tracer into the central tube and the first surrounding ring of tubes observed in the ideal setup, here the tracer is eccentrically displaced, highlighting the influence of the angled inflow.

isoTPMS Modules

For the isoTPMS modules, Figure 3.7 presents the results of the RTD simulations and measurements. Simulations were conducted for both unit cell sizes; however,

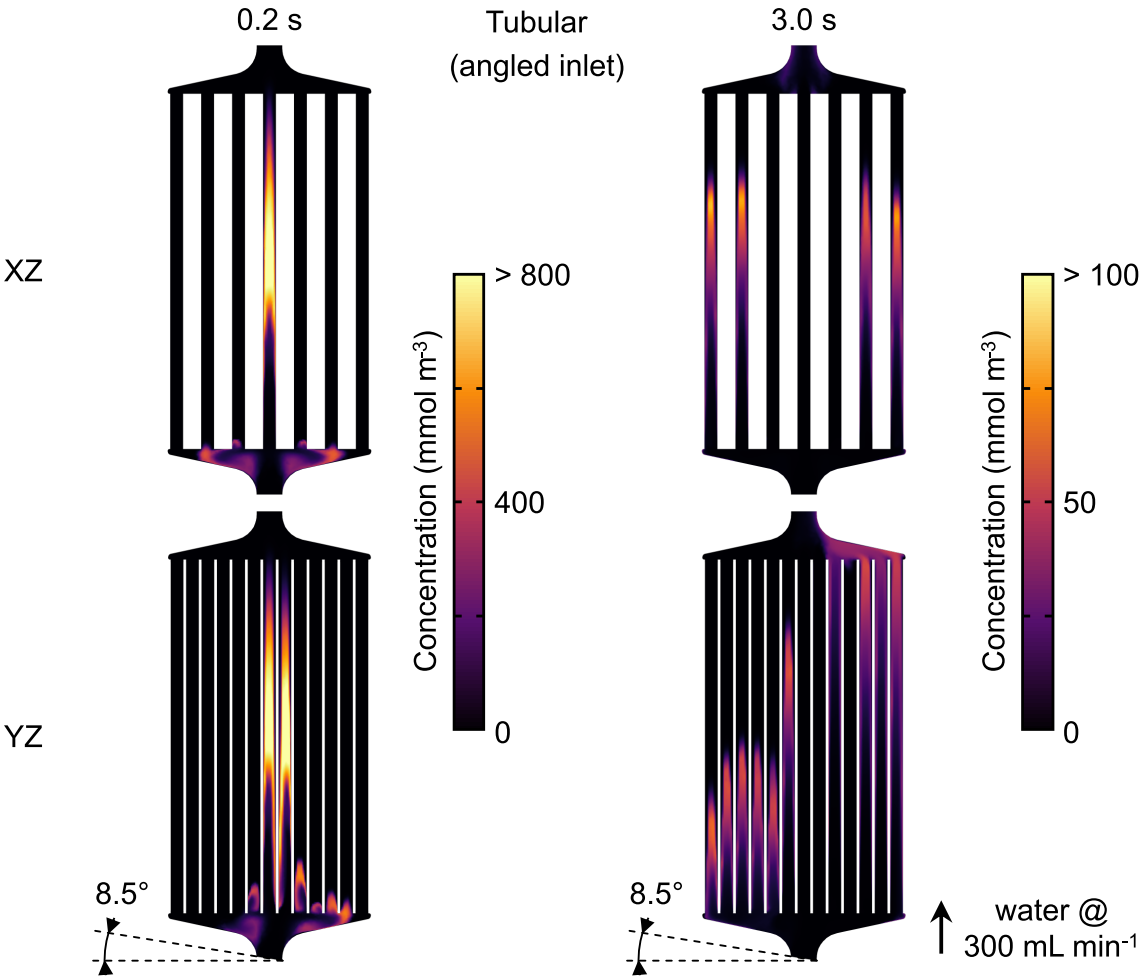

Figure 3.6: Cross-sectional images of the tubular module at 0.2 s and 3.0 s, showcasing the simulated tracer passage. The inlet face was rotated by 8.5° around the X-axis to replicate potential deviations caused by a bent tube in the experimental setup. To improve the visibility of tracer concentrations, distinct color bars were applied: the 0.2 s images utilize a range from 0 to 800 mmol m^{-3}, whereas the 3.0 s images cover a range from 0 to 100 mmol m^{-3}.

only the module with smaller unit cells underwent experimental measurement. All three RTD curves closely align with only minimal differences in the curves between the simulated modules with larger and smaller unit cells. The simulation results show peak times at 4.3 s, while the experimental curve peaks slightly later at 4.6 s. All peaks are near the module's calculated mean residence time, τ = 5 s, which represents the time required to replace the module's 25 mL volume at a flow rate of 300 mL min^{-1} as defined by Equation 2.20.

All curves feature slightly left-shifted maxima, suggestive of channeling effects, and exhibit tailing, which corresponds to the presence of dead zones within the module. These phenomena are illustrated by the cross-sectional images for the

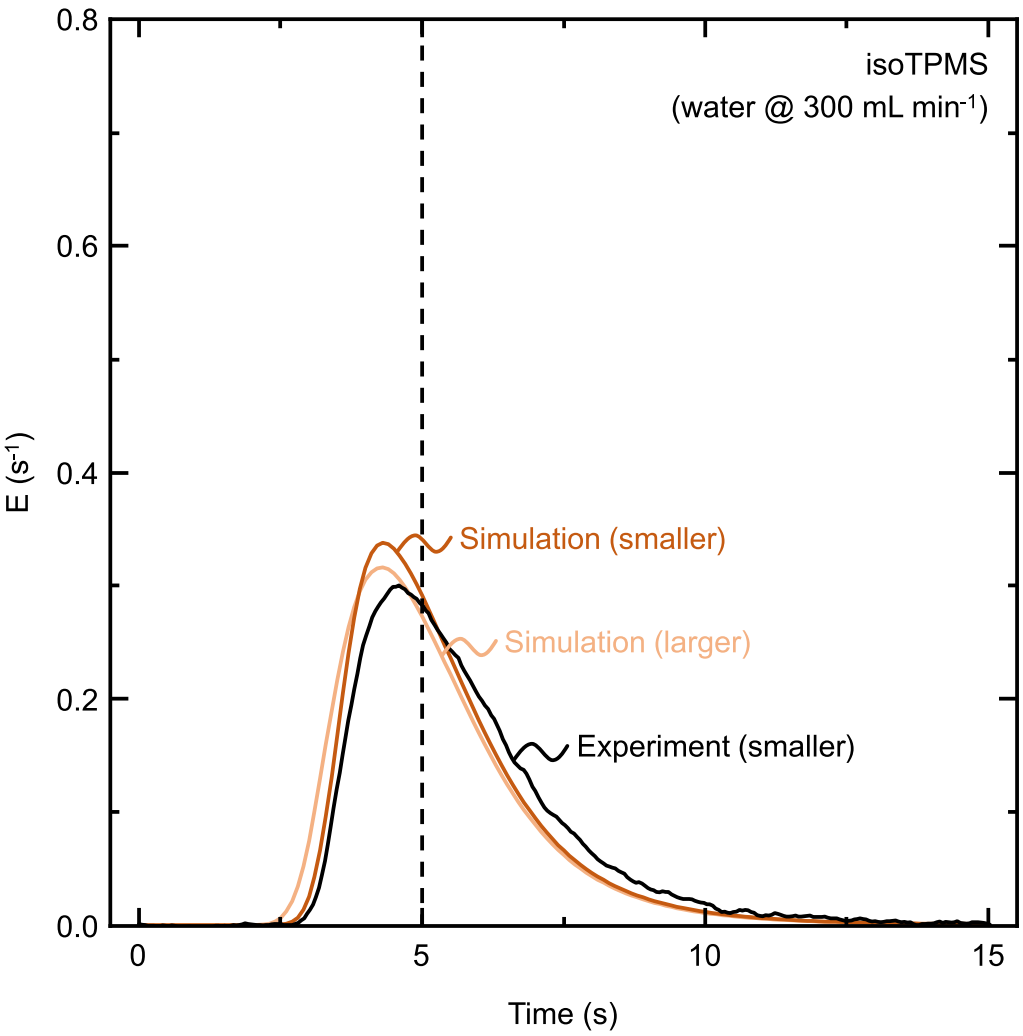

Figure 3.7: Simulative and experimental RTD for the isoTPMS modules. Simulations were run for both unit cell sizes but only the module with smaller unit cells was measured experimentally. At 5 s the dashed line marks the mean residence time τ.

module with smaller unit cells in Figure 3.8. The images captured at 0.2 s reveal that the bottom corners of the module are not directly exposed to the tracer. Furthermore, the images taken at 3.0 s demonstrate wall effects, characterized by low tracer concentrations along the module's outer perimeter where the TPMS structure is constrained by the module's housing. Although not depicted, the concentration profile of the module with larger unit cells is very similar. Along with their analogous RTD curves, this similarity suggests that reducing the unit cell size from 4.27 mm to 3.0 mm does not significantly alter the flow dynamics but does increase the surface-area-to-volume ratio while maintaining consistent flow characteristics. In contrast to the tubular module, the flow within the isoTPMS modules is markedly

more uniform with a single peak and a Gaussian-like distribution.

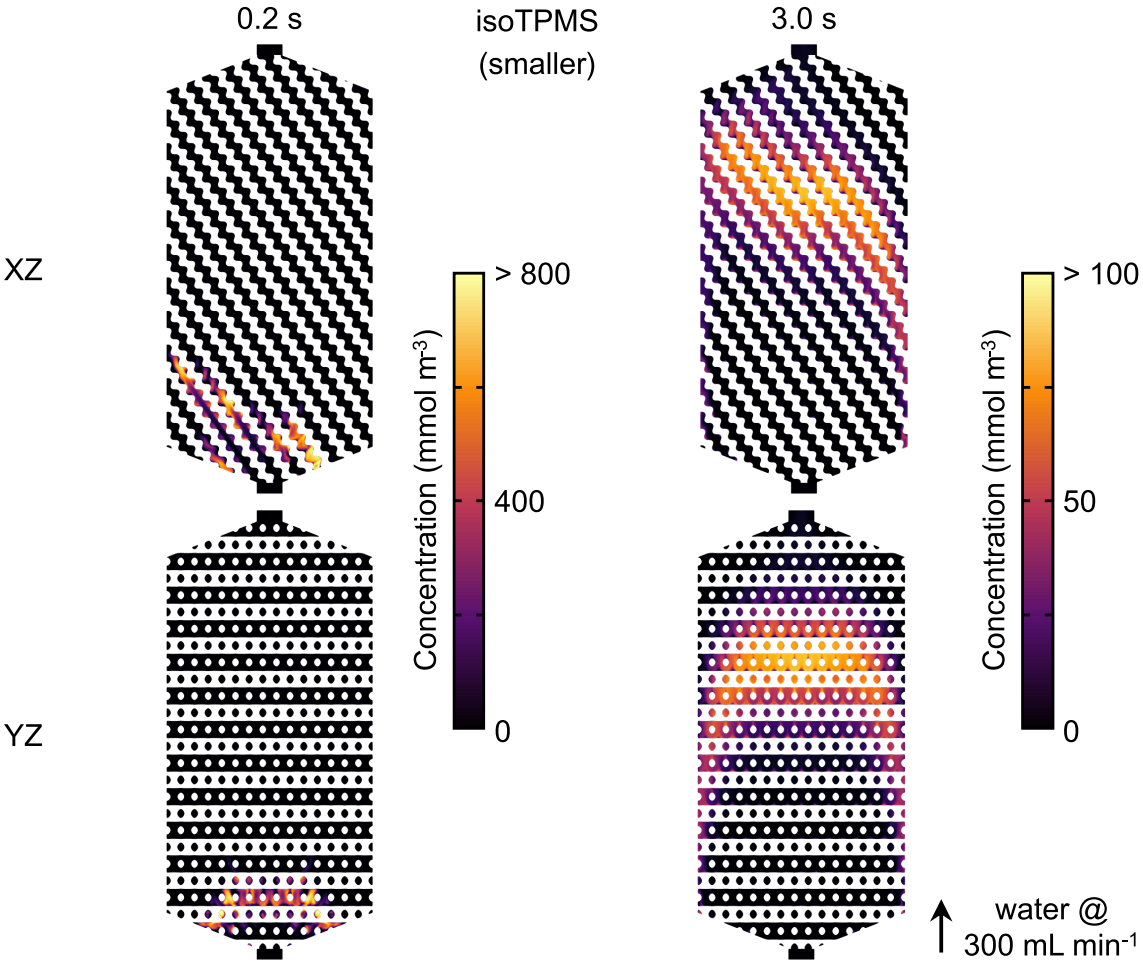

Figure 3.8: Cross-sectional images of the isoTPMS module with smaller unit cells at 0.2 s and 3.0 s, showcasing the simulated tracer passage. To improve the visibility of tracer concentrations, distinct color bars were applied: the 0.2 s images utilize a range from 0 to 800 mmol m^{-3}, whereas the 3.0 s images cover a range from 0 to 100 mmol m^{-3}.

anisoTPMS Module

To mitigate the wall and channeling effects inherent to the isoTPMS geometry, an anisometric structure was explored. This involved using unit cells that gradually decreased in size at the inlet and increased at the outlet to smooth the transition between the tube and the module geometry. In the outer areas, larger unit cells were utilized to reduce flow resistance, aiming to achieve a more uniform flow distribution.

The RTD curves for the anisoTPMS module are displayed in Figure 3.9, where

the simulation and experiment align very closely. The peak maxima were shifted to 3.4 s for the experiment and 3.6 s for the simulation, suggesting enhanced channeling effects compared to the isoTPMS module. Additionally, the presence of more pronounced peak tailing indicates increased dead zones.

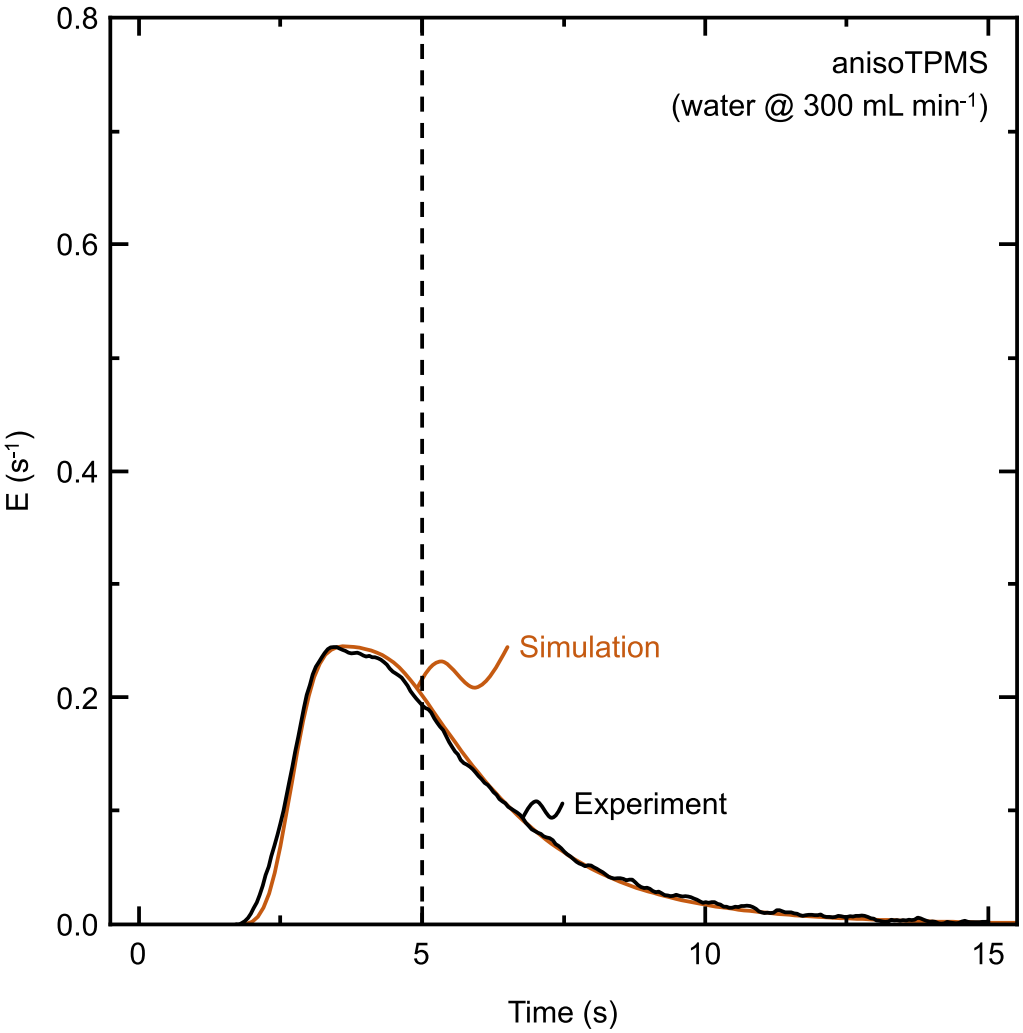

Figure 3.9: Simulative and experimental RTD for the anisoTPMS module. At 5 s the dashed line marks the mean residence time τ.

Despite the intention to create a more uniform flow using anisometric unit cells, the resulting RTD data suggest the opposite effect. The cross-sectional images in Figure 3.10, which visualize the concentration profile, reveal minimal flow through the module corners. The geometry design seems to restrict radial flow at the inlet, causing the main flow to proceed directly to the module's core. Consequently, radial distribution of the tracer is impeded at the inlet, leading to a parabolic tracer front evident in the 3.0 s images.

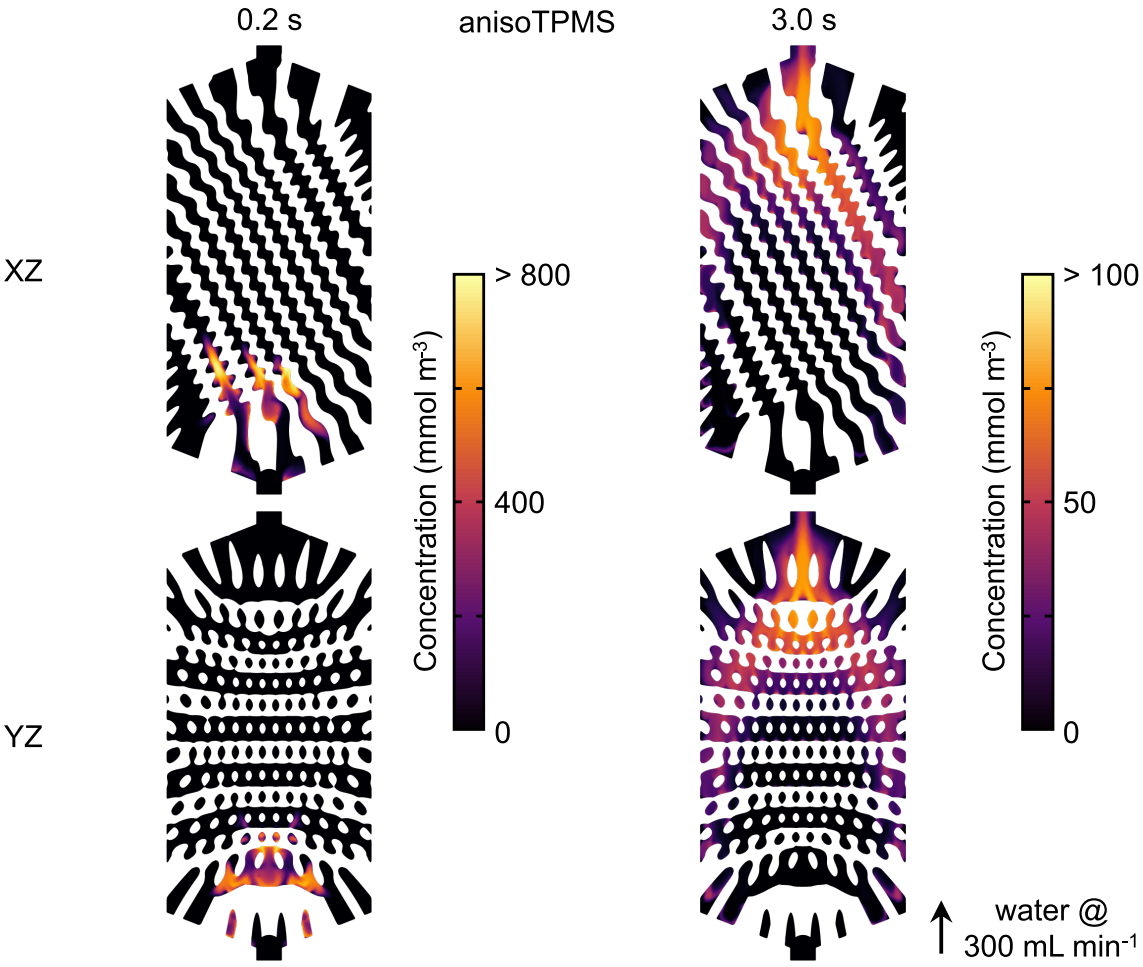

Figure 3.10: Cross-sectional images of the anisoTPMS module, showcasing the simulated tracer passage. To improve the visibility of tracer concentrations, distinct color bars were applied: the 0.2 s images utilize a range from 0 to 800 mmol m^{-3}, whereas the 3.0 s images cover a range from 0 to 100 mmol m^{-3}.

3.3.2 Simulative Investigation of Hemodynamics

Following the validation of the simulation model, a fluid model mimicking blood properties was applied to assess the hydrodynamics of blood perfusion. This assessment was conducted in a stationary study of laminar flow using the inelastic non-Newtonian Carreau-Yasuda viscosity model (Equation 2.36), with parameters derived from Seehanam et al. [Seeh2023]. The study facilitated the extraction of velocity and shear rate profiles, enabling the validation of the laminar flow assumption, identification of stagnation zones, and determination of critical shear rates.

Velocity Profiles

Due to outcomes from the simulation model validation (Section 3.3.1) and RTD measurements, further examination of the "tubular module with straight inflow" will be discontinued. Similarly, the "isoTPMS module with larger unit cells" will be excluded because of its resemblance to the "isoTPMS module with smaller unit cells", which was used in the blood experiments detailed in Chapter 4.

Velocity profiles from the stationary simulation study are illustrated in Figure 3.11 through cross-sections in the XZ and YZ planes. In the tubular module, the velocity profile corroborates the findings from the RTD simulations and measurements, showing much higher velocities in the central tubes, indicating a lack of uniform flow distribution across the module's cross-section. Also in hollow fiber dialyzers this channeling of blood along the central axis was observed [Ronc2002] and dialyzer diameter and packing density can be varied to reduce this effect [Hira2012]. The widening of the inlet region has no impact, causing the flow to clash onto the flat surface from which the tubes protrude leading to a large radial variability in residence time [Umat2019]. However, the angled inlet clearly demonstrates the influence of inflow direction. As radial distribution is compromised, the flow velocity in the peripheral tubes is very low, making these areas prone to stagnation.

In the isoTPMS module, the velocity decreases sharply at the inlet and increases toward the outlet, resulting in high velocities at the transition from tubing to the TPMS structure. Compared to the tubular module, the TPMS structure achieves a more uniform flow distribution, where, after several layers of unit cells, the fluid flows at a nearly homogeneous velocity through the module. Towards the outlet the structure occupies a lot of volume, wherefore high velocities are present. Here, and at the inlet, some void volume would help the transition from tube to TPMS structure. Due to this uniform flow distribution, the core of the module is homogeneously perfused and not susceptible to stagnation. However, the module corners receive less perfusion, leading to some stagnation, as already indicated by the RTD simulations.

In the anisoTPMS module this void volume is present due to the distorted unit cells creating a smooth transition. The large unit cells in the inlet and outlet area drastically reduce the flow velocity. However, the inlet structure is suboptimal as it guides flow axially rather than distributing it radially. While distorting the unit cells facilitates a smooth transition, there remains potential for further optimization of the structure to enhance early radial distribution [Tian2024]. Consequently, the corners at the module's inlet are prone to stagnation, as they receive minimal direct flow.

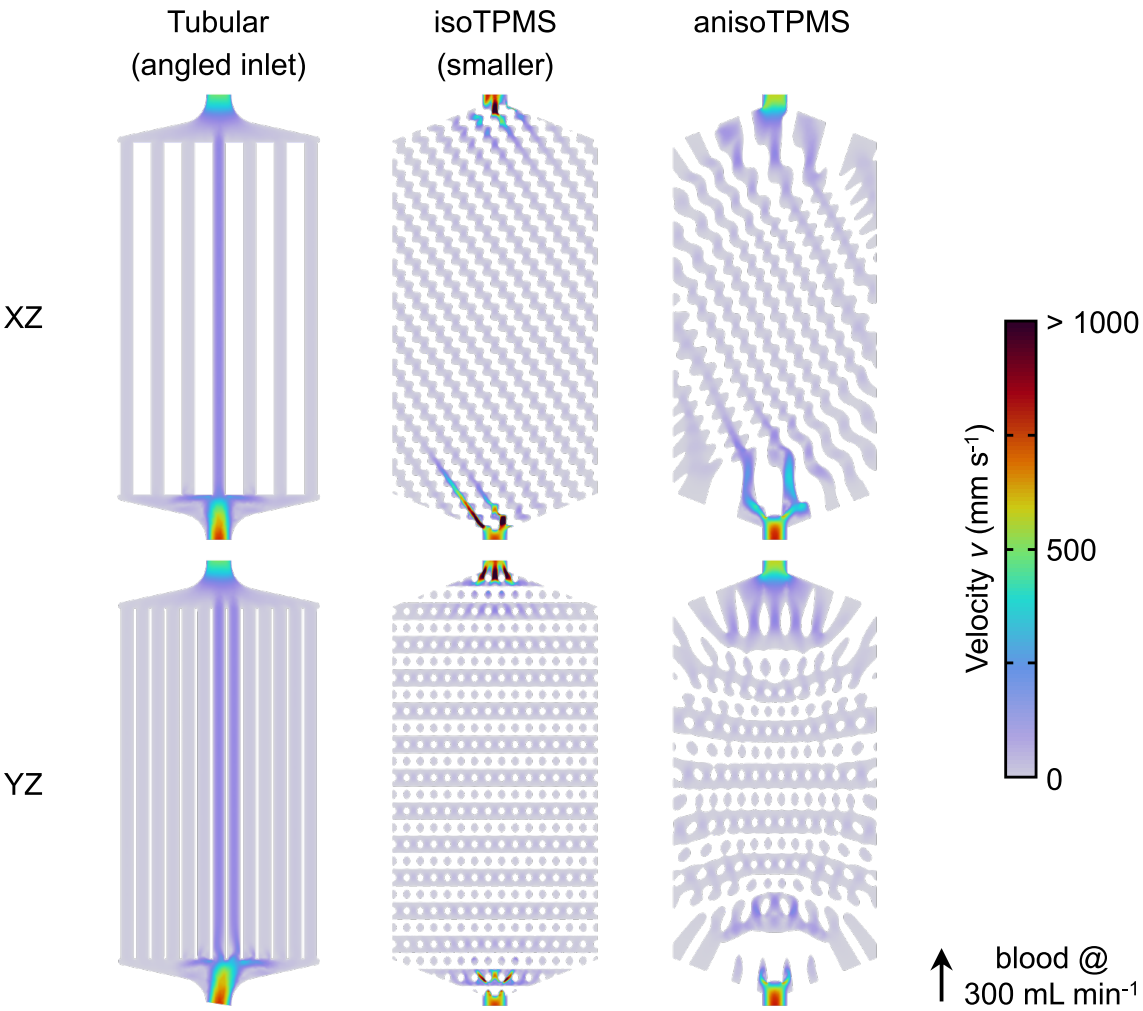

Figure 3.11: Simulated velocity profiles, where the modules were perfused continuously from bottom to top. The simulations use a viscosity modeled by the inelastic non-Newtonian Carreau-Yasuda model. The images display cross-sections in the XZ and YZ planes, with velocities ranging from 0 to 1000 mm s^{-1}.

The maximal Reynolds numbers recorded were *Re* = 34 for the tubular module, and *Re* = 16 each for the isoTPMS and anisoTPMS modules. These values confirm that all modules maintain laminar flow conditions as explained in Section 2.2.2 and documented in literature [Hawk2023]. As intended by the designer, the tubular module has strong similarities to hollow fiber dialyzers even though the tubes are ten-fold larger than hollow fiber membranes. In dialyzers the greater back pressure of the hollow fibers leads to more radial distribution in the inlet region but channeling along the center axis remains [Kim2009; Hira2012]. Hemoadsorbers are similar as their packed bed of porous beads or the fiber bundles for adsorption resemble the flow characteristics of a hollow fiber membrane bundle with limited radial distribution [Umat2019]. In membrane lungs non-uniform flow distributions are also

a common challenge mostly related to the inlet and outlet geometries [Hess2022]. The presented TPMS module designs ensure much better flow distribution while maintaining the flow regime. Furthermore, the anisoTPMS module functions at similar flow velocities compared to the tubular module.

Shear Rate Profiles

Regions with high velocities, particularly near walls, correspond to high shear rates. Figure 3.12 displays the simulated shear rates, color-coded on a non-linear scale ranging from $0\,s^{-1}$ to $4000\,s^{-1}$. Within the tubular module, elevated shear rates are prominent at the inlet, especially at the transition into the tubes. Throughout the module, the central tubes consistently exhibit high shear rates. In the isoTPMS module, areas with high shear rates align with regions of high flow velocities at the inlet and outlet. Compared to the tubular module, the red areas in the isoTPMS indicate much higher shear rates. In the anisoTPMS module, milder flow velocities result in lower shear rates, with few areas colored in red.

Table 3.3 presents the simulated average shear rate $\dot{\gamma}_{av}$, maximum shear rate $\dot{\gamma}_{max}$, the fluid volumes of the modules V_F, and the volumes experiencing shear rates greater than $1000\,s^{-1}$ $V(\dot{\gamma}>1000\,s^{-1})$, along with the volume fraction of the latter calculated by dividing the high shear volume by the fluid volume. Clearly, the average shear rates are similar across all modules.

Table 3.3: Simulated results of average shear rate $\dot{\gamma}_{av}$ and maximal shear rate $\dot{\gamma}_{max}$ and fluid volume with shear rates above $1000\,s^{-1}$ $V(\dot{\gamma}>1000\,s^{-1})$ to quantify the relative volume $\frac{V(\dot{\gamma}>1000\,s^{-1})}{V_F}$ related to the module's total fluid volume V_F.

Module	$\dot{\gamma}_{av}$ [s^{-1}]	$\dot{\gamma}_{max}$ [s^{-1}]	V_F [mL]	$V(\dot{\gamma}>1000\,s^{-1})$ [mm^3]	$\frac{V(\dot{\gamma}>1000\,s^{-1})}{V_F}$ [%]
tubular (angled inflow)	40	3230	24.8	4.1	0.02
isoTPMS (smaller)	86	32 184	25.0	105.8	0.42
anisoTPMS	59	95 807	25.0	13.4	0.05

Notably, the maximum shear rates in the TPMS modules are extremely high. However, the volume fraction with a shear rate greater than $1000\,s^{-1}$ is less than 0.5 % for the isoTPMS module and only 0.05 % for the anisoTPMS module. It is hypothesized that these extremely high shear rates occur on the surface of the module due to a rough mesh. For the anisoTPMS module, the left image in Figure 3.13 shows a 3D volume cut in half in the XZ plane. The center of the figure

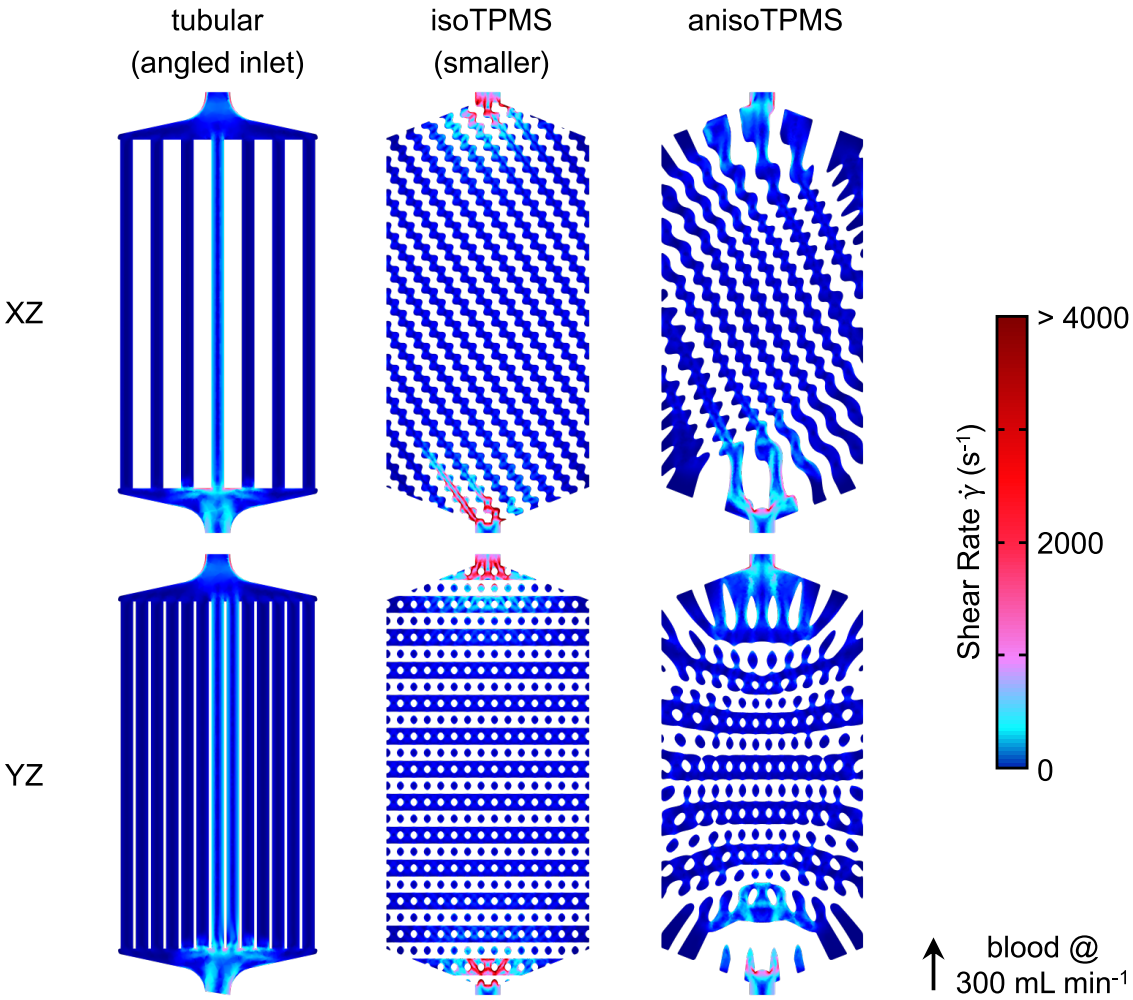

Figure 3.12: Simulated shear rate profiles, where the modules were perfused continuously from bottom to top. The simulations use a viscosity modeled by the inelastic non-Newtonian Carreau-Yasuda model. The images display cross-sections in the XZ and YZ planes, where shear rates are color-coded with a non-linear color scale ranging from 0 to 4000 s^{-1}.

highlights two cropped sections at the inlet and outlet where the fluid elements have a shear rate greater than 1000 s^{-1}. On the right side of the figure, a further magnification of the inlet in the XY plane shows only fluid elements with shear rates exceeding 4000 s^{-1}, illustrating that the sharp-edged mesh defining the fluid volume contributes to the extreme shear rates observed.

The shear rates in all modules are within a reasonable range compared to state of the art dialyzers (up to 800 s^{-1}) [Ronc2002], oxygenators (up to 3000 s^{-1}) [Birk2018], and common shear rates in the human body (10 to 2000 s^{-1}) [Feau2023]. When neglecting possible mesh deficits in the TPMS modules, the isoTPMS module exhibits high-shear areas in the inlet and outlet but the anisoTPMS

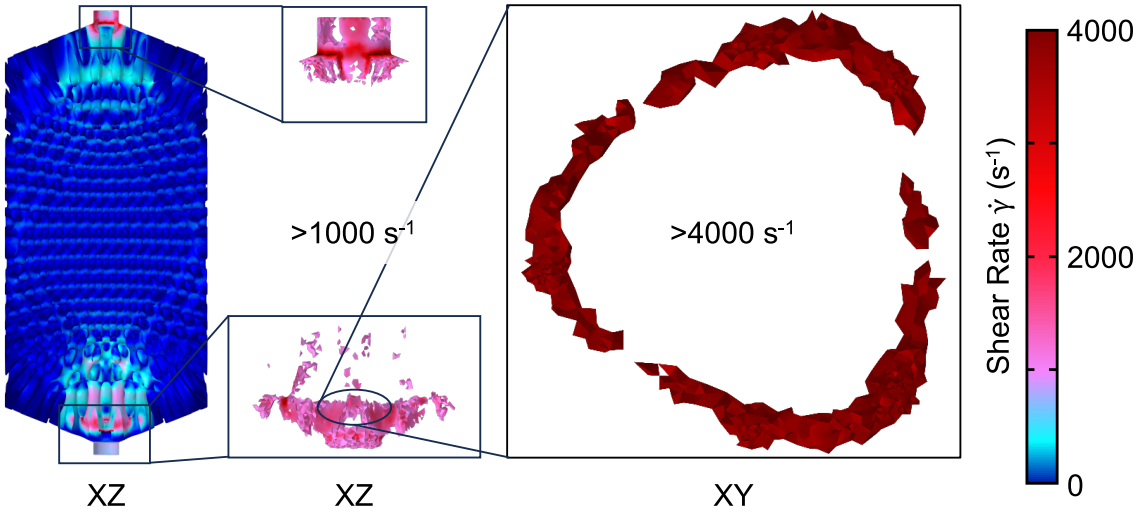

Figure 3.13: Simulated shear rate profile of the anisoTPMS module, where the module was perfused continuously from bottom to top. The simulation used a viscosity modeled by the inelastic non-Newtonian Carreau-Yasuda model. The left image shows the 3D volume of the module cut in half in the XZ plane. Next to it are two magnifications of the 3D volume of the inlet and outlet region cropped to all fluid elements with a shear rate $>1000\,s^{-1}$. The right image shows a further magnification of the inlet in the XY plane with all fluid elements with a shear rate $>4000\,s^{-1}$.

module resembles the tubular module very well. For hemoadsorbers, especially fiber based devices, similar shear rates are expected due to their similarity to hemodialyzers. Nevertheless, shear rates above approximately $630\,s^{-1}$ are sufficient to change the binding behavior of platelets. However, the time for which a particle is exposed to a shear force also plays a decisive role. A short exposure at a high shear rate can have the same effect as a long exposure at a low shear rate. [Casa2015]

3.4 Conclusion

This chapter describes the design of perfusable modules with integrated TPMS structures as internal geometries. One highlight is, that the entire module volume was utilized, which represents an enormous advance over classical tubular modules. The modules were successfully additively manufactured and their digital twin was used in a stationary flow simulation with time-dependent tracer transport.

The simulation model used was validated with the help of RTD experiments. For the TPMS modules in particular, the results from simulation and experiment are in good agreement. Furthermore, it was shown for the *tubular* module that the deviations in the shape of the curve between simulation and experiment are due to the direction of flow into the module. In this respect, the TPMS modules offer a decisive advantage, as their distributor function is independent of the inflow direction. The temporal offset of the RTD measurement for the *tubular* module could not be fully explained. For the TPMS modules no such displacement was recorded, thus diminishing assumed variations due to manual handling.

Stagnation and low flow areas within blood-contacting modules are commonly associated with blood clot formation. These conditions, particularly prevalent in regions where shear rates drop below $10\,s^{-1}$, can lead to stasis, significantly increasing the risk of clotting. The corner regions of all modules are critical areas where such low shear conditions were observed.

In addition to stagnation, blood clotting can also be triggered by high shear rates, which activate platelets and initiate the coagulation cascade, as detailed in Section 2.1.1. Comparing shear rates within the modules to those occurring naturally in the human body, it is evident that shear rates exceeding $630\,s^{-1}$ can lead to platelet activation and subsequent binding to von Willebrand factor (vWf). This is particularly concerning in the inlet and outlet regions, as well as the central tubes of the *tubular* module, where such high shear rates may precipitate shear-induced coagulation. Among the geometries studied, the *isoTPMS* module exhibits the best flow distribution across the module but also presents the largest volume subjected to elevated shear rates. The *anisoTPMS* module, while ensuring good flow distribution, effectively reduces high shear rates at both the inlet and outlet, mitigating the risk of shear-induced coagulation.

Concluding from the presented hydrodynamic analysis, the expected areas that are prone to coagulation due to stagnation are

a. the outer tubes of the *tubular* module

b. and the corner regions of all modules.

Furthermore, areas that might be prone to coagulation due to elevated levels of shear rates are

c. the inlet and outlet regions

d. and the inner tubes of the *tubular* module.

In the following chapter these identified critical areas are examined in a randomized study with human whole blood.

4.

Structure-Induced Clotting in 3D Printed Blood Contactors

Parts of this chapter have been published as:
Lukas T. Hirschwald, Franziska Hagemann, Maik Biermann, Paul Hanßen, Patrick Hoffmann, Tim Höhs, Florian Neuhaus, Maerthe Theresa Tillmann, Petar Peric, Maximilian Wattenberg, Maik Stille, Tamara Fechter, Alexander Theißen, Patrick Winnersbach, Kai P. Barbian, Sebastian V. Jansen, Ulrich Steinseifer, Bettina Wiegmann, Rolf Rossaint, Matthias Wessling, Christian Bleilevens, John Linkhorst
Enhanced Hemodynamics of Anisometric TPMS Topology Reduce Blood Clotting in 3D Printed Blood Contactors, Advanced Healthcare Materials, 2024
DOI: 10.1002/adhm.202403111

4.1 Introduction

Triply periodic minimal surface (TPMS) geometries are novel geometries for blood treatment devices whose advantages have been demonstrated particularly in the field of gas exchange in membrane lungs [Hess2021]. The secondary flows generated by the structure reduce the accumulation of gases at the membrane and thus increase the driving force for more diffusive mass transport [Femm2015b; Femm2015a]. Furthermore, TPMS have excellent properties as a distributor structure to uniformly deliver blood to the entire interior of the device in order to utilize the full potential of the device. However, regions with increased shear rates or regions with very slow blood flow lead to deposits and blood clots that clog the membrane and thus reduce mass transfer [Lehl2008; Lai2024]. These regions must be avoided when designing blood treatment devices.

Furthermore, the influence of TPMS geometries on the coagulation behavior of blood has not yet been investigated. The margination of platelets that occurs in laminar flow due to the Fåhræus effect [Fåhr1929; Herc2016] could be reduced with the help of secondary flows, resulting in fewer platelets adsorbing and fewer clots forming. The uniform distribution of blood flow in the inlet region has the potential to homogenize the flow conditions in the module, eliminating regions with low flow velocities.

To investigate the coagulation behavior of human whole blood in TPMS geometries, three modules were perfused according to ISO 7199 [DIN 2020]. During the experiments, blood parameters such as the number of platelets and experimental parameters such as the pressure drop across the module and the flow velocity were recorded hourly. Following the experiments, the deposits and blood clots were fixed and their volume and location determined by computed tomography (CT) scanning. A comparison with the hemodynamics investigated in the previous chapter shows the clear influence of the shear rate on coagulation. Furthermore, significant differences in coagulation due to the geometry could be determined.

4.2 Materials and Methods

The same blood contactor modules discussed in section 3.2.1 were employed for human whole blood experiments. Additionally, a 33 cm piece of tubing (ECC noDop 3/8 x 3/32, Raumedic AG, Germany) fitted with two tapering tube connectors (4 mm to 10 mm, MEDICOPLAST International GmbH, Germany) and two 8 cm pieces of tubing (Class VI, 1/8 x 1/16 S DEHP free, from CAPIOX FX05 set, Terumo Europe N.V., Belgium) was used as reference. This tubing assembly, with a total volume of 25 mL, was pre-filled with a 0.9 % NaCl infusion solution (B. Braun SE, Germany).

4.2.1 Experimental Setup for Blood Circulation

Human blood experiments were conducted using a setup that included two identical circuits, allowing for simultaneous testing of two modules. The blood for these experiments was donated by 12 healthy volunteers following approval by the ethical committee of the University Hospital of RWTH Aachen University (file no. EK22-355) and after obtaining informed consent. Details on donor variability can be found in Table 4.1.

Table 4.1: Donor meta data and mapping to module numbers: module - donor - sex - age, where sex is either male (m) or female (f) and the age is given in years. * These experiments were discarded because tube connectors were used which made comparability impossible.

tubular	isoTPMS	anisoTPMS	reference
tub1 - A - f - 24	iso1 - G - m - 26	aniso1 - G - m - 26	ref1 - C - m - 28 *
tub2 - B - m - 37	iso2 - A - f - 24	aniso2 - B - m - 37	ref2 - I - m - 27 *
tub3 - C - m - 28	iso3 - H - w - 28	aniso3 - H - w - 28	ref3 - J - w - 27 *
tub4 - D - f - 29	iso4 - I - m - 27	aniso4 - D - f - 29	ref4 - E - f - 26 *
tub5 - E - f - 24	iso5 - J - w - 27	aniso5 - K - w - 27	ref5 - K - w - 27
tub6 - F - m - 28	iso6 - F - m - 28	aniso6 - L - m - 29	ref6 - L - m - 29

Pretreatment of Blood Contactor Modules

Prior to a whole blood experiments, each module was installed in an HPLC system (Äkta avant 25 with Unicorn 6.1, GE Healthcare Bio-Science AB, Sweden) in place of a column. First, the module was wetted with ethanol (>99.8 % denatured, Carl Roth GmbH, Germany) at a flow rate of 5 mL min^{-1} to remove all air. Then, a

flow of 25 mL min^{-1} was applied for at least 2 min to rinse the module. Afterward, the module was rinsed with ultra-pure water (MilliQ) at a flow rate of 25 mL min^{-1} until the UV signal of the HPLC detector was constant (λ = 280 nm). In the last step, the module was filled with infusion solution (NaCl 0.9 % infusion solution, B. Braun SE, Germany) at 25 mL min^{-1} until a constant conductivity was established in the conductivity detector. Both ends were closed with Luer-Lock plugs (Combi-Stoppers, Ref 4495101, B. Braun SE, Germany).

Before conducting whole blood experiments, each module was installed in a high pressure liquid chromatography (HPLC) system (Äkta avant 25 with Unicorn 6.1, GE Healthcare Bio-Science AB, Sweden) in lieu of a column. The module was initially wetted with ethanol (>99.8 % denatured, Carl Roth GmbH, Germany) at a flow rate of 5 mL min^{-1} to ensure all air was expelled. This was followed by a 25 mL min^{-1} flow for at least 2 min to thoroughly rinse the module. Subsequently, the module was flushed with ultra-pure water (MilliQ) at the same flow rate until the UV signal from the HPLC detector stabilized at λ = 280 nm. The final preparation step involved filling the module with a 0.9 % sodium chloride infusion solution (B. Braun SE, Germany) at 25 mL min^{-1} until the conductivity detector indicated a constant conductivity. Both ends of the module were then sealed with Luer plugs (Combi-Stoppers, Ref 4495101, B. Braun SE, Germany).

Blood Circulation

Each circuit was assembled according to Figure 4.1 using one 90 cm and two 20 cm pieces of silicone tubing (ECC silicone 1/4 x 1/16, Raumedic AG, Germany), connected through four T-piece tubing connectors with lateral Luer connection (connector straight, 1/4 x 1/4, FLSKG13300, free life medical GmbH, Germany). At the ends, two couplers (Coupler Funnel/Luer-Lock, Ref 4896645, B. Braun SE, Germany) were employed to attach the module. Additionally, three three-way stopcocks (Discofix C, Ref 16494C, B. Braun SE, Germany) and a temperature probe (Temperature Probe with Female Luer-Lock, Ref BFF01990, Promepla OEM Solutions, Monaco) were integrated into the circuit, which has a total volume of 41 mL.

Peripheral Devices

The 90 cm tube was positioned within a peristaltic pump (CAPS double pump, Stöckert Instrumente GmbH, Germany), set to deliver a blood flow rate of approximately 300 mL min^{-1} at a rotational speed of about 70 min^{-1}. The connector for

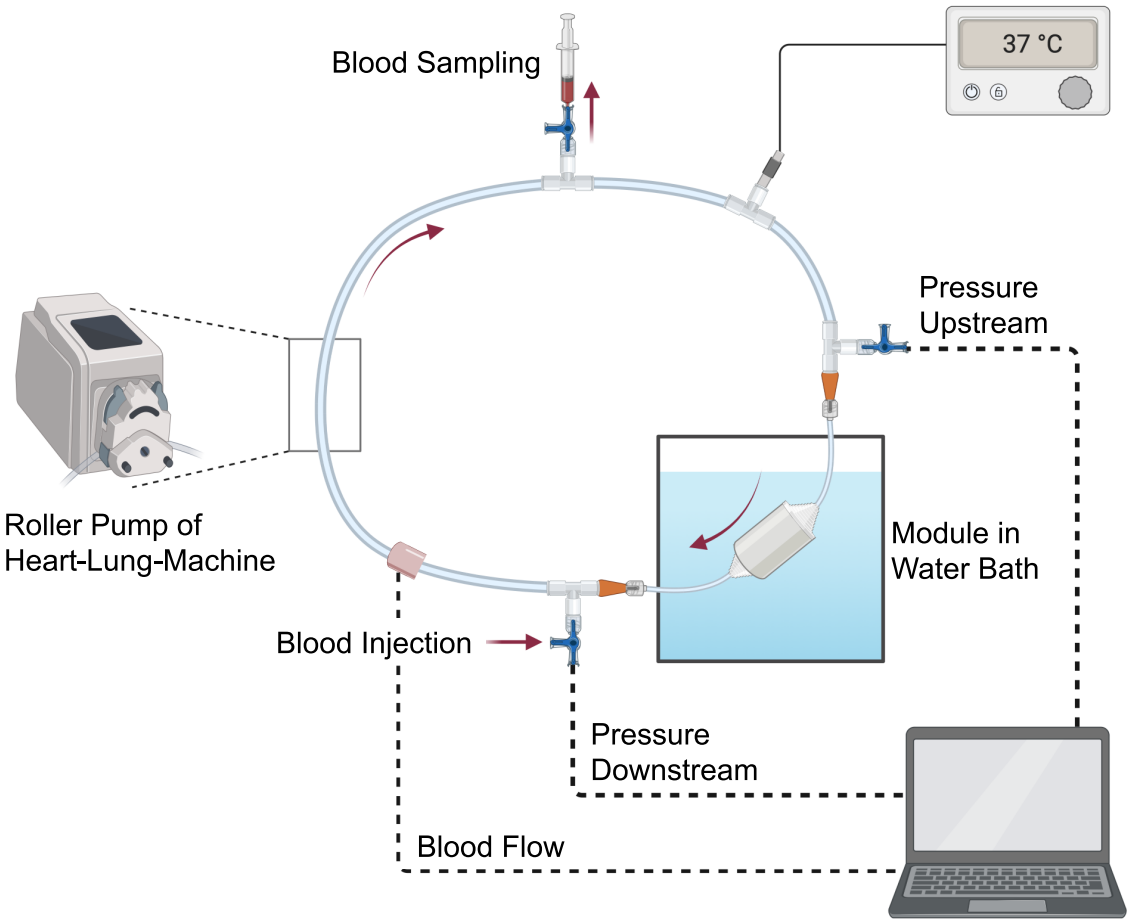

Figure 4.1: Setup for human whole blood experiments. A roller pump of a heart-lung-machine circulates human whole blood at a flow rate of 300 mL min^{-1}. The module is placed in a temperate water bath to keep it at a constant temperature of around 37 °C. Right before and after the module the pressure is measured. At the top and bottom, ports are available for sampling and filling, respectively. A flow sensor monitors the flow rate.

blood sampling was installed slightly elevated to allow air to accumulate. Two perfusion lines (Original Perfusor Line, Ref 8255067, B. Braun SE, Germany) were attached to the three-way stopcocks upstream and downstream of the module to facilitate system pressure measurement using a pressure transducer (Xtrans, CODAN pvb Medical GmbH, Germany). A male-to-male Luer adapter (male-2-male LL, Ref 893.00, Vygon, France) was necessary for connecting the pressure transducer. Pressure data were acquired via a contact board (Contactboard 3-fold, Ref 75.1078, CODAN pvb Medical GmbH, Germany) and transmitted to a patient monitoring device (IntelliVue MX500, Philips Medizin Systeme Boeblingen GmbH, Germany). Temperature was monitored using a sensor (RET-3 Rectal Probe for Mice, Physitemp Instruments LLC, USA), connected to a temperature controller (TCAT-

2LV Animal Temperature Controller - Low Voltage, Physitemp Instruments LLC, USA). Additionally, a non-invasive flow sensor (1/4 x 1/16, em-tec GmbH, Germany) was placed around the silicone tubing downstream of the peristaltic pump, with readings taken by a flow computer (SonoTT Ultrasonic Flowcomputer, em-tec GmbH, Germany). Once assembled, the module was positioned in a plastic box linked to a water bath with a thermostat (Haake B3 and DC3, Gebr. HAAKE GmbH, Germany) to maintain stable temperature conditions.

Filling of Blood Circulation

The perfusion lines were initially filled with infusion solution, flushed, and the pressures zeroed using the patient monitor. Following this, the inlet and outlet tubes of the module were clamped off (Sicherheitsklemme KL 20, Achim Schulz-Lauterbach Vertrieb medizinischer Produkte GmbH, Germany). The plugs were removed, and the tube ends were meticulously filled with perfusion solution to eliminate any air before connecting the module to the circuit, while all three-way stopcocks were closed. Prior to connecting the module, the two connectors were partially filled with infusion solution using a syringe with cannula.

Blood was drawn from a donor into a 50 mL syringe pre-loaded with 50 IU of heparin (Heparin-Natrium 25 000 IU mL^{-1}, B. Braun Melsungen AG, Germany), and gradually introduced into the circuit through the injection port. To facilitate the entry of blood and expulsion of air, the blood sampling port was opened during this process. Just before the circuit was fully filled, a 10 mL syringe was attached to the sampling port to withdraw any remaining air and about 5 mL of blood.

Once this setup was complete, the three-way stopcocks were switched to connect with the pressure sensor. The pre-module pressure was adjusted to (75 ± 2) mmHg using the 10 mL syringe. After zeroing the flow sensor, the roller pump was started, and its speed was gradually increased until the blood flow reached 300 mL min^{-1}.

4.2.2 Experimental Procedure and Blood Analytics

Before initiating blood circulation, baseline parameters such as blood cell counts were recorded (CellTac-alpha cell counter, Nihon Khoden, MEK-6500K, Germany). Additionally, the initial activated clotting time (ACT) was measured (Hemochron Junior Analyzer & JACT+ Cuvette, Werfen GmbH, Germany), and baseline blood

serum samples were stored at $-80\,^{\circ}C$ for later analysis. Samples were taken after 5 min and at 1 h, 2 h, 3 h, 4 h, 5 h and 6 h, or upon terminating the experiment.

During the experiment, parameters such as blood temperature (°C), roller pump speed (min^{-1}), blood flow ($mL\,min^{-1}$), and the pressure difference across the module (mmHg) were continuously monitored. At the 5 min mark, 0.5 mL of blood was withdrawn from the circuit via the blood sample port for analysis of blood cell count and ACT. For all other sampling intervals, 2.5 mL of blood were withdrawn to assess cell count, ACT, and for blood serum storage. Stagnant blood in the valve was discarded each time a sample was taken. After each sampling event, infusion solution was re-injected to maintain the pre-module pressure at (75 ± 2) mmHg.

The experiment was terminated after 6 h or earlier if the module became blocked (flow $<100\,mL\,min^{-1}$). Following termination, the module was flushed with infusion solution and then filled with formalin (4 % formaldehyde in aqueous solution) to preserve the coagulated blood for subsequent CT scanning. Analysis of the blood serum included measuring free hemoglobin levels as an indicator of hemolysis (ABL800 blood gas analyzer, Radiometer, Germany).

4.2.3 Computed Tomography (CT) Analysis

The modules were imaged using a CT scanner (FF35, Comet yxlon GmbH, Germany). Prior to scanning, they were emptied of formalin and dried with a gentle air stream. Scanning parameters included a tube voltage of 30 kV and a tube current of 410 µA. The set focus-detector-distance was 940 mm, with a focus-object-distance of 204 mm. Utilizing a detector binning of 3 x 3 and a pixel pitch of 150 µm, the resolution achieved was a voxel size of 97 μm^3. The tomograms were reconstructed using the FDK-filtered back projection approach (CERA, Siemens Healthineers AG, Germany).

Target-Actual Comparison

A target-actual comparison of the modules was conducted using VGSTUDIO MAX (version 3.5, Volume Graphics GmbH, Germany). This process involved detecting the module's surface, performing a best-fit registration to the CAD file in STL format, and applying a target-actual comparison function with a set exclusion threshold of 300 µm. This threshold was used to disregard discrepancies between surfaces greater than the set value, such as the rods of the part holder, which are considered irrelevant.

Analysis of Residual Blood

Additionally, a custom-written algorithm was used to analyze the distribution of residual blood within the modules based on the CT scans. The algorithm processed 180 images, each centered and rotated around the central module axis. The axis was identified by applying a Haugh transformation to both a lower and an upper slice of the tomogram, as shown in Figure 4.2. These images were then overlaid and averaged to produce a two-dimensional image that provides density information, illustrating the location of coagulated blood within the modules.

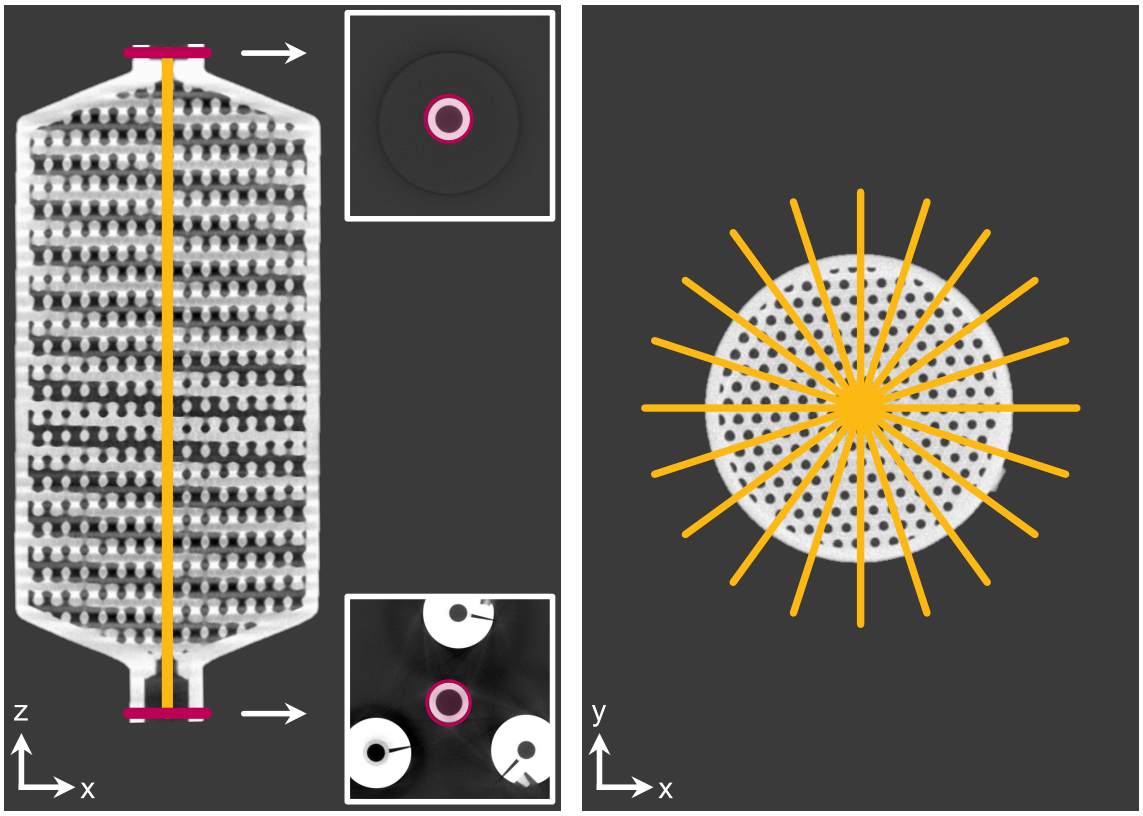

Figure 4.2: Left: Determined rotation axis visualized in the x-z-plane with alignment images at the inlet and outlet. Right: Exemplary visualization of 10 out of 180 read out positions for the aggregation of the density images of each module scanned via CT.

4.2.4 Data Analysis

Calculation of Corrected and Normalized Platelets

The graphs depicting the corrected and normalized platelet counts in Figure 4.3 and 4.5 were adjusted to enhance clarity and comparability. Corrections were applied

to account for the dilution effect during sampling. Normalization was necessary to standardize the results across different donors. All calculations were based on an assumed blood circuit volume of 41 mL, with normalizations referencing the values measured at 5 min after starting the experiment. If data at 5 min were unavailable, the measurements taken at 1 h were used.

Statistical Analysis

Statistical analyses were conducted using OriginPro (version 2023, OriginLab Corporation, USA). The volume of blood clots, expressed as a percentage, was tested for normal distribution using the Kolmogorov-Smirnov test. Upon confirming normal distribution, a One-Way ANOVA for non-paired data was performed, including a multiple comparison analysis using the TUKEY method. P-values less than 0.05 were considered statistically significant.

4.3 Results and Discussion

The coagulation in the three module types was investigated in a two-part study. The first part involved experiments with human whole blood, employing the setup illustrated in Figure 4.1. Clogging within the modules was monitored visually and linked with various measurements including blood flow, pressure drop, and platelet count. In the second part, CT imaging scanned the modules to determine the quantity and locations of clots. All experiments used fresh human blood from both female and male donors in equal proportion. Details on the donor assignments and their metadata are provided in Table 4.1. Each module or reference tube was infused for 6 h; however, if clogging reduced the flow rate below 100 mL min^{-1}, the experiment was terminated early.

4.3.1 Validation of Measurement Setup

To validate the experimental setup, six reference measurements with just a straight piece of tubing instead of a module were conducted. In the first four measurements (ref1 to ref4), connectors between the circuit and the reference tube induced significant pressure drops and hemolysis. Consequently, only the last two measurements (ref5 and ref6), which used the same connectors as the module experiments, were considered for validation. Figure 4.3 presents the pressure drops ΔP and corrected, normalized platelet counts $\overline{PLT'}$ across the reference tubes over the 6 h test period.

All measurements were carried out in a blood circuit with a test plan similar to the ISO 7199 standard [DIN 2020]. The setup's reliability is confirmed as there was negligible pressure drop, no coagulation, and only a minor reduction in platelet numbers. Additionally, the stable levels of free hemoglobin, an indicator of hemolysis, suggest minimal cell damage, thus this variable is not further discussed.

4.3.2 Visual Inspection and Evaluation of Pressure Drop and Platelet Count

Three indicators of clogging were examined. Firstly, Figure 4.4 displays photographs of all modules post-experiment, used as visual confirmation of blood debris accumulation. The initial color of the modules is transparent with a yellow tint. Therefore, any dark red discoloration signals erythrocyte deposition, a key compo-

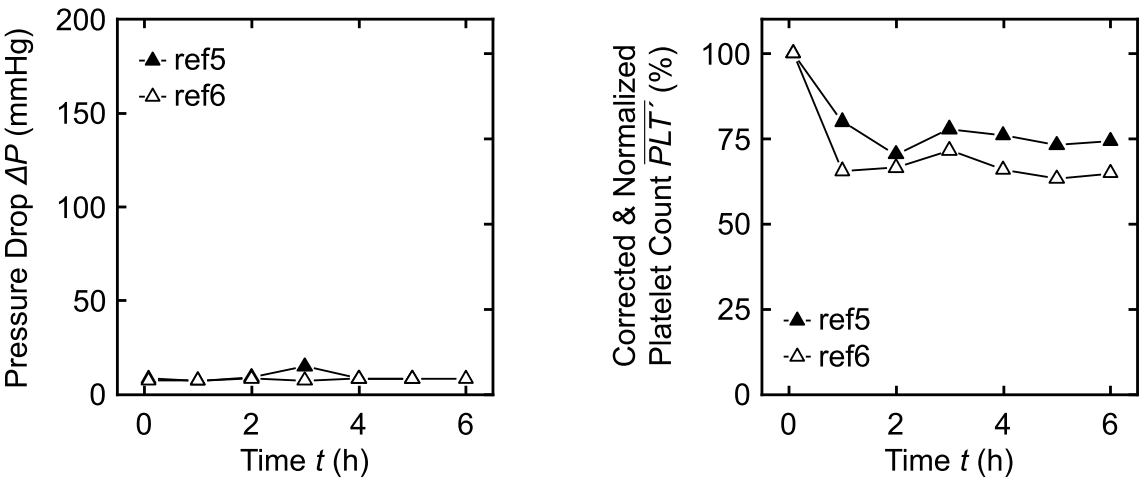

Figure 4.3: Graphs depicting pressure drop ΔP and corrected, normalized platelet count $\overline{PLT'}$ for the references measurements over 6 h. Out of six reference measurements, only the last two (ref5 and ref6) were valid for comparison due to identical connector usage as in module experiments, mitigating the connector-induced anomalies seen in earlier trials.

nent of blood debris.

Secondly, the pressure drop ΔP across the modules was measured, as blood coagulation can restrict or obstruct flow, leading to increased pressure. Thirdly, the platelet count (PLT) was monitored, as clot formation typically reduces circulating platelet levels. Platelet counts were adjusted for dilution (PLT') and normalized ($\overline{PLT'}$) to control for donor variability. Figure 4.5 showcases graphs of both pressure drop (a) and platelet count (b) across all modules.

Regarding the tubular modules, five out of six exhibited significant red discoloration, indicative of clogging, except for module tub4. This discoloration aligns with the observed trends in platelet reduction and pressure increase. Notably, tub1 displayed a less significant platelet drop yet required early termination after 5 h18 min. Tub3 showed a steady decrease in platelets and increased pressure towards 5 h. After sampling at 5 h, the platelets increased and the pressure decreased, suggesting that the sampling may have alleviated a blockage.

In the isoTPMS series, two of six modules, iso3 and iso5, turned dark red, signifying substantial coagulation, while the others exhibited lighter discoloration. The platelet graphs for iso1 and iso6 indicated significant clot formation after 5 h. For all four modules mentioned, the coagulation indications are corroborated by rising pressures.

The anisoTPMS experiments showed a notable discoloration in module aniso3,

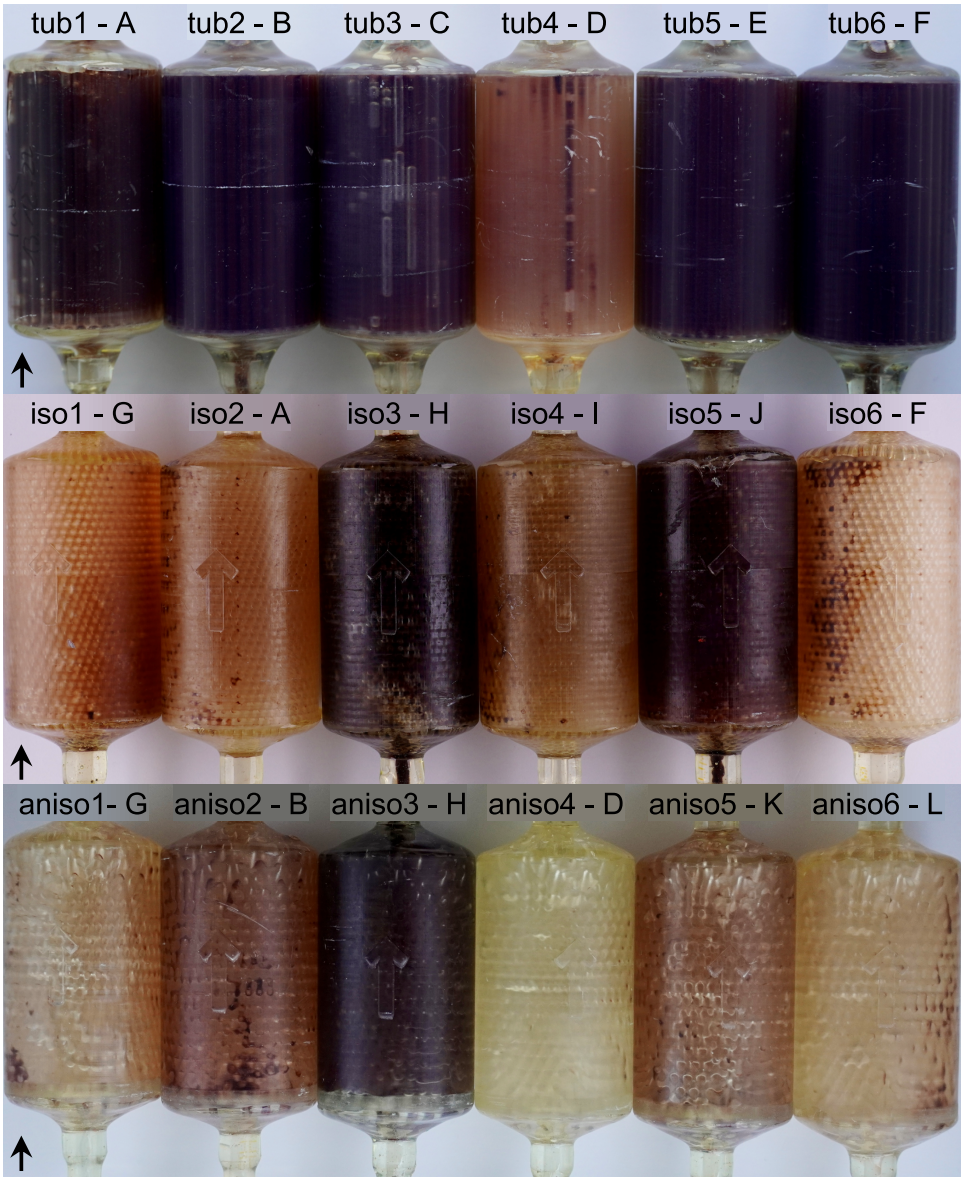

Figure 4.4: Sequential photographs of all tested modules post-experiment, labeled A to L corresponding to donor IDs in Table 4.1. A dark red hue in a module suggests the presence of blood debris and clogging from coagulation.

turning dark red, with lighter red hues in aniso2 and aniso5, suggesting some blood debris. These three modules also recorded the lowest platelet counts by the end, with aniso3 and aniso5 experiencing a sharp increase in pressure, indicative of severe clogging.

Compared to the reference measurements, the pressure drops at the start of the experiments are slightly higher in all modules, which is to be expected due to the integrated modules. The tubular and anisoTPMS modules are at around 30 mmHg, the isoTPMS module at around 50 mmHg. The slightly higher pressure drop in the

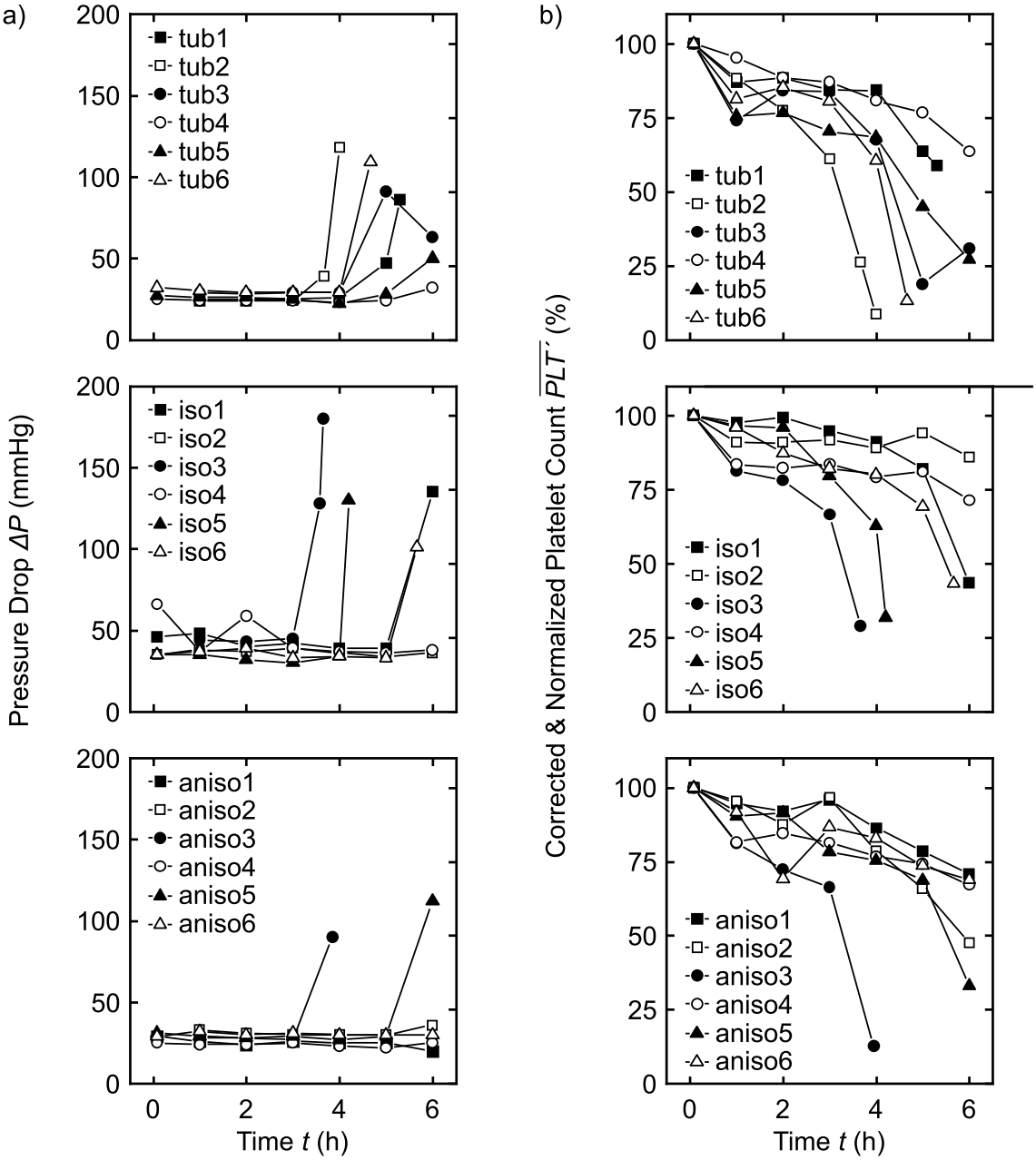

Figure 4.5: a) Graphs of pressure drop (ΔP) over the modules plotted against the experiment time. b) Graphs of corrected and normalized platelet counts $\overline{PLT'}$ in the blood circuit plotted over the experiment time. Notable pressure increases and platelet decreases indicate potential clogging and coagulation.

isoTPMS module can be explained by the larger inner surface area. All values are in the same order of magnitude as pressure drops at 300 mL min^{-1} blood flow in commercial dialyzers (<100 mmHg) [Swee2014; Medt2020] or hemoadsorbers (<50 mmHg) [Cyto]. Membrane lungs are designed for much higher flow rates (up to 7 L min^{-1}) at pressure losses of up to 100 mmHg. Due to the significantly

different operating point, a direct comparison is not possible.

The course of the number of platelets is very identical between the reference measurements and the modules within the first 2 h of the experiments. After the start of the experiment, the platelet level drops to around 75 % of the baseline value. This drop is normal for extracorporeal blood treatment systems and can be attributed to the adhesion of platelets to tube and module surfaces [Duay2022; Kalb2018]. Only the further drop results from the formation of blood clots.

4.3.3 Evaluation via Computed Tomography (CT) Scanning

To explore the hypothesis that module geometry affects clogging rates and patterns, CT imaging was employed to quantify and locate blood debris within the modules. Modules were scanned using an FF35 CT-System at a high resolution of 97 μm^3 per voxel, enabling detailed analysis of the 3D-printed internal structures. Prior to scanning, the modules were cleared of formalin and air-dried to enhance the contrast between the coagulated blood and the surrounding material. A custom post-processing algorithm highlighted clotted blood in 2D representations, as depicted in Figure 4.6. Each image represents a composite of 180 slices taken at 1° intervals around the central axis. Yellow intensities denote high densities, indicating either the module material or accumulated blood debris. An empty module is displayed on the right as a reference. The ratio of clotted volume is noted below each image, with smaller figures indicating lesser debris volume.

In the tubular modules, clots predominantly formed at the transition zone from the inlet to the tubes, although not apparent externally. Also in module tub4, not discolored, a significant clot blocked most of the inlet tubes, except the center ones, explaining the minimal pressure rise observed in Figure 4.5 a). The other tubular modules exhibited clots primarily in areas of high shear rates, as identified in Chapter 3. The presence of a clot before the center tubes redirected flow at increased velocities towards the outer tubes, instigating further shear-induced clotting.

Despite minimal external signs of clotting, CT scans revealed blood debris in all isoTPMS modules, particularly at the inlet. Modules iso1, iso3, iso5, and iso6, all of which showed pressure increases, had clots directly constricting the inlet, the site of the highest shear rates. In contrast, iso2 and iso4 showed a less concentrated deposition pattern directly at the inlet but a more uniform distribution over the entire module's cross-section. Overall, the total clot volume in the isoTPMS modules was

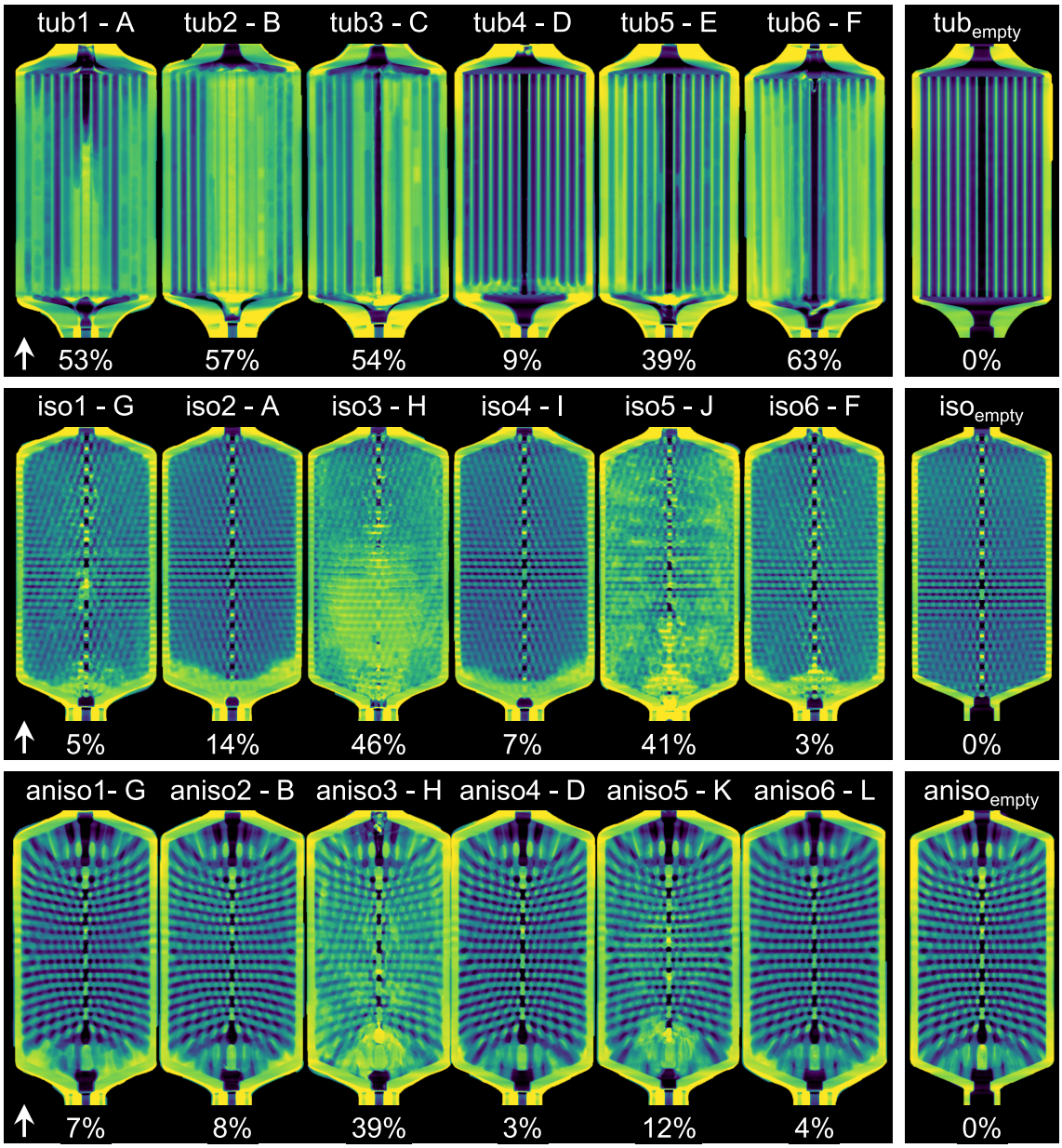

Figure 4.6: Overlay CT images of all modules, where each image represents a composite of 180 slices taken at 1° intervals around the central axis. Yellow intensities denote high densities, indicating either the module material or accumulated blood debris. An empty module is displayed on the right as a reference. The relative clotted volume is noted below each image, with smaller figures indicating lesser debris volume.

considerably less than in the tubular modules.

CT imaging of anisoTPMS modules corroborated the measurement data from Figure 4.5. Large clots were present in aniso3 and aniso5 at the inlet, aligning with identified areas of high shear rate. Aniso2, despite a significant decrease in platelet count, showed only minor deposits, primarily in the bottom corners of the

module. Also in aniso1, aniso4, and aniso6 very small deposits are visible in the bottom corners identified as areas of stagnation.

The comparative analysis of clotted blood volumes across different module types revealed significant differences. The mean clotted blood volume, with standard deviation, was measured at (46 ± 20) % for tubular modules, (19 ± 19) % for isoTPMS modules, and (12 ± 14) % for anisoTPMS modules. Notably, a statistically significant difference (<5 %) was found between the tubular and anisoTPMS modules, indicating that tubular modules tend to accumulate more clots. However, no significant differences were observed between the tubular and isoTPMS modules or between the isoTPMS and anisoTPMS modules.

In all of the modules examined, the blood clots mainly occurred in the inlet area, a region of increased shear rate. In state-of-the-art devices, deposits and blood clots also occur in regions with increased shear rates, which are usually located in the inlet area of these devices [Beel2016]. However, regions with low flow rates, such as the contact points of the fibers or weaving points in membrane lungs, also lead to significant deposits and blood clots [Lehl2008; Lai2024]. Regions with higher flow rates, on the other hand, are less affected. Reducing the size of the unit cells of the TPMS modules can result in low flow rates that lead to clotting. Therefore, regions with high shear rates or low flow rates must be avoided in the design.

4.3.4 Examination of Module Pairs Perfused With the Same Blood

The limited sample size in this study poses challenges in accounting for natural variations in human blood across different donors. However, a direct comparison of modules using blood from the same donor allows for more controlled observations of clogging tendencies. Analysis of these paired modules reveals trends in early experiment termination due to pressure drop (ΔP), platelet count ($\overline{PLT'}$), and relative clotted blood volume (ΔV_{clot}), with values recorded at experiment end provided in Table 4.2. Higher ΔP values suggest blockages, lower $\overline{PLT'}$ levels indicate clot formation, and greater ΔV_{clot} percentages reflect the amount of coagulated blood in the module.

The analysis confirms that tubular modules consistently exhibit poorer performance compared to their TPMS counterparts in terms of blockage and clot formation, as evidenced by the parameters measured. Notable is the tub4-aniso4 pair, which, despite following the trend, shows minimal variation across all measured

Table 4.2: Post-experiment comparison of modules perfused with blood from the same donor. Higher pressure drops (ΔP) suggest blockages, lower platelet counts ($\overline{PLT'}$) indicate clot formation, and greater relative clot volumes (ΔV_{clot}) reflect the amount of coagulated blood in the module.

		tub1	iso2	tub2	aniso2	tub4	aniso4	tub6	iso6	iso1	aniso1	iso3	aniso3
ΔP	[mmHg]	86	36	118	36	32	25	109	101	135	20	180	90
$\overline{PLT'}$	[%]	59	86	9	48	64	67	13	43	44	71	29	13
ΔV_{clot}	[%]	53	14	57	8	9	3	63	3	5	7	46	39

values. For the tub6-iso6 pair, differences in ΔP are slight, yet discrepancies in platelet counts and clot volumes are pronounced. The isoTPMS and anisoTPMS pairs (iso1-aniso1 and iso3-aniso3) show variations mainly in pressure, with inconclusive differences in platelet count and clot volume. These results substantiate the hypothesis that module geometry significantly influences coagulation dynamics, with blood clotting occurring more rapidly in tubular modules compared to TPMS modules.

Clot formation is predominantly observed in the inlet areas of all module types, where the blood encounters higher shear rates. This suggests that elevated shear rates are a major factor contributing to clotting and blood deposition. Although dead zones, characterized by low flow areas as detailed in Chapter 3, were noted primarily in the anisoTPMS modules, their impact appears minimal in this study. The extent to which dead zones affect clotting remains uncertain, particularly since the blood was treated with heparin, which prevents coagulation in stagnant conditions but not under shear-induced conditions.

4.4 Conclusion

From the blood experiments, a trend for the coagulation behavior depending on the module geometry is recognizable. The tubular modules discolored the strongest, the number of platelets decreased the most, and the experiments had to be terminated earlier than the others. However, no direct statistical significance can be derived from the data of the blood experiments. Only determining the clot volume within the modules using CT scans shows that the anisotropic geometry is significantly better than the tubular geometry. It is striking that the blood formed blood clots almost exclusively in regions of increased shear rates.

Regarding dead zones, it is essential to note that we used heparin as an anticoagulant that primarily inhibits blood coagulation in stagnant areas. The small amount of heparin applied was expected to be degraded over the experimental period of 6 h, ensuring that dead zones also contribute to clotting. However, it was impossible to predict when the effect of the heparin diminished and whether there was sufficient time for a clot to form due to stasis by the end of the experiment. Since no clots were found in the identified dead zones, but the heparin may have prevented them, no conclusive statement regarding geometry-related coagulation in dead zones is possible.

In order to prevent coagulation, the elimination of both coagulation mechanisms, stasis in dead zones and activation in regions of increased shear rates, is necessary. Anisotropic TPMS structures create a smooth transition from tubing to structure to avoid high shear rates. With the help of optimization algorithms, creating an anisotropic TPMS structure with perfect residence time distribution (RTD) could be possible. As the unit cells become smaller, the flow resistance increases such that the flow distribution in the module can be adjusted based on the size of the unit cells. By optimizing the module housing and tailoring the TPMS structure towards a perfect RTD, this module type has a high potential to circumvent non-ideal flow distributions in blood contactors.

5.

Simulative Optimization of Blood Contactor Modules

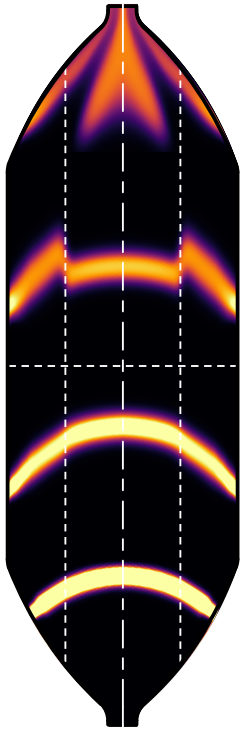

5.1 Introduction

Commercial blood treatment devices use simple cuboidal or cylindrical housings with homogeneous hollow fiber stacks. As in the human lung, blood must be distributed to all areas of the devices to fully exploit the exchange surface. However, the flow paths in the peripheral areas are longer than along the central axis. Thus, the optimal perfusion of a these devices is achieved when each blood fluid element remains for an equal time in the module and is exposed to physiological shear rates [Ronc2007]. One way to achieve equal residence times with flow paths of different lengths is to achieve local differences in flow velocity. Hollow fiber membranes of the same size and in a homogeneous arrangement offer a uniform resistance that leads to uniform flow velocities. For local variability, the resistances must be varied. [Hess2022]

Depending on the design, the spacing of the hollow fiber membranes can be varied, which is only possible with the help of additional spacers [Ronc2007]. However, only two-dimensional spacing can be achieved with spacers between hollow fibers. Adapting the inlet port, the blood can first be distributed over the cross-section of the device, whereby it must flow faster radially than axially in order to compensate for the residence time shift in the inlet or outlet area [Yama2009]. However, additional head space is required for distribution that does not contribute to mass exchange. Alternatively, a cubic module shape that increases the length between the inlet and outlet with a very narrow shape is conceivable, so that the deviations of the flow path lengths are minimized [Umat2019]. With anisometric triply periodic minimal surface (TPMS) structures, almost any housing geometry can be completely filled and the flow can be tailored to the desired conditions. Hesselmann et al. showed that iterative computational fluid dynamics (CFD) simulations allowed the flow velocity to be approximated to a target value by changing the local permeability. [Hess2022]

In order to achieve optimal perfusion, measured as residence time distribution (RTD), CFD simulation in combination with Bayesian optimization was employed. Firstly, the outer geometry of previous modules (Chapter 4) was parameterized and optimized (Set 1 & 2). Therefore, the module's interior was abstracted as a porous medium with uniform permeability. Secondly, the fluid volume of the optimized outer geometry was sectioned into domains with variable permeability, each optimized towards optimal perfusion (Set 3). In detail, the position of the RTD peak, the distribution's broadening and symmetry, and the maximal and average shear

rate were investigated parameters. The optimization of the outer geometry yielded a significant improvement compared to previous module geometries. In particular, the elongation of the inlet and outlet zone that form the transition from tubing to module improved perfusion. Incorporating rounded corners considerably reduced the maximum shear rate. Moreover, by segmenting the module into only four domains with differentiated permeabilities, the optimization achieved a narrow and almost ideal Gaussian RTD, illustrating the profound impact of these alterations on enhancing perfusion efficacy.

5.2 Materials and Methods

The CFD software COMSOL Multiphysics (Version 6.1, COMSOL AB, Sweden), including the software modules *CFD Module*, *Chemical Reaction Engineering Module*, *Porous Media Flow Module*, and *LiveLink for MATLAB* were used throughout this work. For optimization calculations, the simulations were executed from MATLAB (Version R2022b, The MathWorks, Inc., USA) via LiveLink for MATLAB (Version 6.1, COMSOL AB, Sweden). All computing was performed under 64bit Windows 10 on an Intel Xeon Gold 5122 CPU with 192 GB of RAM.

5.2.1 Computational Fluid Dynamic Simulations

The simulations of the modules were performed as axisymmetric in 2D space using the inverse geometry, which refers to the fluid-containing volume of the module. Velocity profiles and shear rates were simulated with a stationary study (study 1) of *free and porous media flow*. A fully developed laminar flow (Re = 340) with a volumetric flow rate of $\dot{V}$ = 300 mL min^{-1} at the module's inlet was set. The Newtonian fluid had a density of ρ = 1060 kg m^{-3}, and a dynamic viscosity of η = 5 mPa s. When no domains were used, the entire geometry was defined as *porous medium* domain with the same fluid properties, a porosity of ϕ = 0.5, and a permeability of $\kappa = 7.24 \cdot 10^{-10}$ m^2. At the walls a no slip condition was used.

A time-dependent study (study 2) for the transport of a tracer molecule through the module was used to simulate the RTD. Tracer peaks were implemented with the COMSOL physics *transport of diluted species in porous media* coupled to the stationary flow with a *reacting flow, diluted species* multiphysic. The tracer was added via a rectangular function in the interval 0 to 0.05 s with an amplitude of $1 \cdot 10^6$ mol m^{-3} and a diffusion coefficient of $D = 1 \cdot 10^{-9}$ m^2 s^{-1} using the *Millington and Quirk* diffusivity model. The time-dependent study was performed at time steps of 0.01 s for 12 s utilizing the solution of the stationary study. At the outlet boundary the concentration was recorded for further evaluation.

5.2.2 Module Geometry Parameters for Simulation

The module was generated via polygons and Bézier curves and then converted into a solid object. A *physics-controlled* mesh was applied to the entire geometry with the element size set to *finer* as a balance between resolution and computing time.

Figure 5.1 shows the reference module and visualizes the flow from bottom to top with injected tracer at the inlet and measured tracer concentration at the outlet.

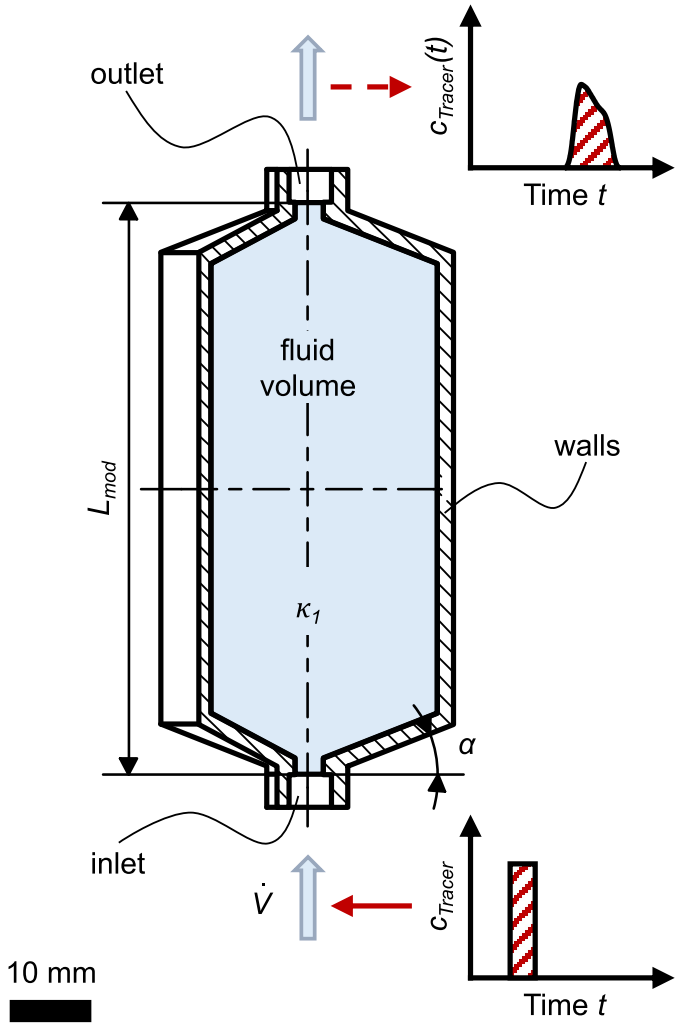

Figure 5.1: Reference module with an inclination angle of $\alpha = 21.45°$, a flow rate of $\dot{V} = 300\,\mathrm{mL\,min^{-1}}$, a pulsed tracer injection with amplitude of $10^6\,\mathrm{mol\,m^{-3}}$, and a permeability of $\kappa_1 = 7.24 \cdot 10^{-10}\,\mathrm{m^2}$.

Figure 5.2 shows the variability for Set 1 and 2 where the outer geometry is optimized.

In Set 3 the inner geometry is optimized by sectioning the fluid volume into $n_{radial} \times n_{vertical}$ domains as visualized by Figure 5.3.

To alter the geometry, the parameters of the polygons and Bézier curves and the number of domains and their permeability were used as variables. They constitute the set of parameters to build the simulation model:

- α_{in}: module's inclination angle at inlet ($\alpha_{in,ref} = 21.45°$),

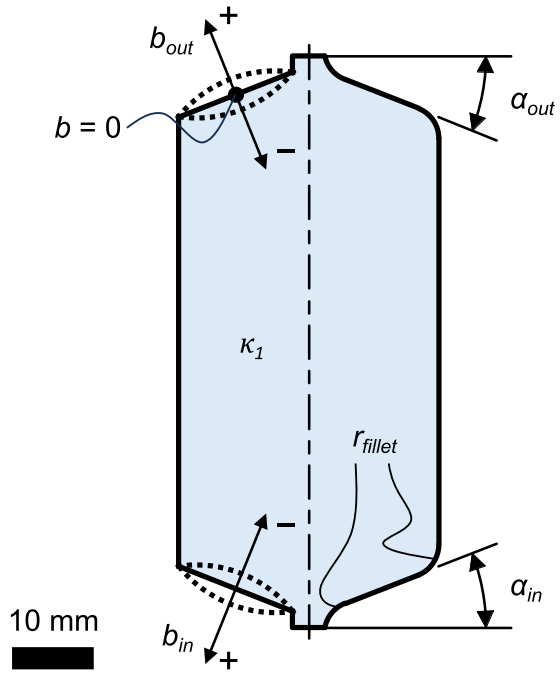

Figure 5.2: Input variables for Set 1 and 2, where the inclination angles α_{in}, α_{out}, the fillet radius r_{fillet}, and the Bézier parameters b_{in} and b_{out} were varied. In Set 1 $b_{in} = b_{out} = 0$ yields a straight line. In blue only the fluid volume previously shown in Figure 5.1 is depicted.

5

- α_{out}: module's inclination angle at outlet ($\alpha_{out,ref} = 21.45°$),
- b_{in}: Bézier parameter for Bézier curve at inlet ($s_{in,ref} = 0$),
- b_{out}: Bézier parameter for Bézier curve at outlet ($s_{out,ref} = 0$),
- r_{fillet}: fillet radius for all corners ($r_{fillet,ref} = 0\,\text{mm}$),
- n_{radial}: number of radial domains ($n_{radial,ref} = 1$),
- $n_{vertical}$: number of vertical domains ($n_{vertical,ref} = 1$),
- κ_d: permeabilities of domains, where $\kappa_1 \ldots \kappa_n$ for each domain ($\kappa_{1,ref} = 7.24 \cdot 10^{-10}\,\text{m}^2$).

The boundary conditions for the input parameters are chosen to limit the length of the module to $L_{mod,max} = 100\,\text{mm}$. Hence, depending on the simulation case the following boundaries apply:

- $\alpha_{in} = \alpha_{out} \in [21.45°, 55.66°]$
- $\alpha_{in} \neq \alpha_{out} \in [21.45°, 68.48°]$ and $\alpha_{in/out,max} = \arctan\left(\frac{2\cdot(100\,\text{mm} - L_0 - 2\cdot L_{end})}{D-d} - \tan(\alpha_{in/out})\right)$
- $b_{in}, b_{out} \in [-0.3, 0.3]$

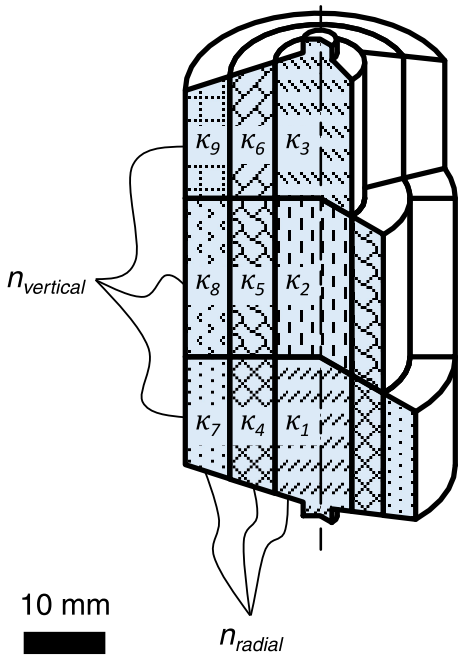

Figure 5.3: Illustration of the sectioning into radial and vertical domains for Set 3. The 2D simulation geometry is uniformly sectioned. κ_n represents the varying permeabilities. These permeabilities are the input variables for the optimization while the outer geometry is kept unchanged.

- $r_{fillet} \in [0\,\text{mm}, 4\,\text{mm}]$ when $b_{in} = b_{out} = 0$
  $r_{fillet} \in [0\,\text{mm}, 3.2\,\text{mm}]$ when $b_{in}, b_{out} \in [-0.3, 0.3]$

5.2.3 Evaluation of Simulation Results

From the COMSOL simulation the concentration values at the module's outlet $c(t)$ and the minimal, maximal, and average shear rates were extracted. With the concentration values the RTD density function $E(t)$, the dimensionless time θ, the mean residence time τ, and the dimensionless RTD density function $E(\theta)$ can be calculated (Equations 2.19-2.22). With those values the RTD graph can be plotted.

The comprising parameter for the optimization algorithm p is made up of three parts:

- peak position p_{pos},
- peak broadening p_{broad},
- and peak symmetry p_{sym}.

These three parameters need to be condensed to one. Therefore, the sum of

squares is calculated as depicted in Equation 5.1.

$$p = p_{pos}^2 + p_{sym}^2 + p_{broad}^2 \tag{5.1}$$

Peak Position

The peak position p_{pos} considers the maximum E_{max} and compares it's corresponding time value $t(E_{max})$ to the mean residence time τ as shown in Figure 5.4 and given by the following Equation 5.2:

$$p_{pos} = |t(E_{max}) - \tau| \qquad p_{pos} \in [0, \infty) \qquad \text{(s)} \tag{5.2}$$

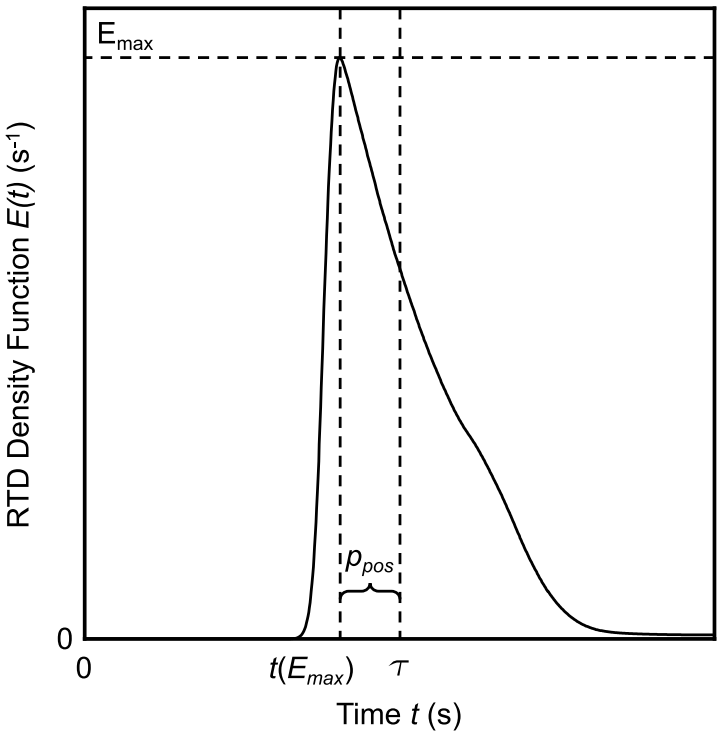

Figure 5.4: Visualization of evaluation parameter peak position p_{pos}.

Peak Broadening

The peak broadening is defined by the square root of the second central moment (variance), thus it is the standard deviation σ given by Equation 2.30 and Equation 5.3. Figure 5.5 shows $2 \cdot p_{broad}$ in the interval $\tau - \sigma$ and $\tau + \sigma$.

$$p_{broad} = \sqrt{\mathbb{V}} = \sigma \qquad p_{broad} \in [0, \infty) \qquad \text{(s)} \tag{5.3}$$

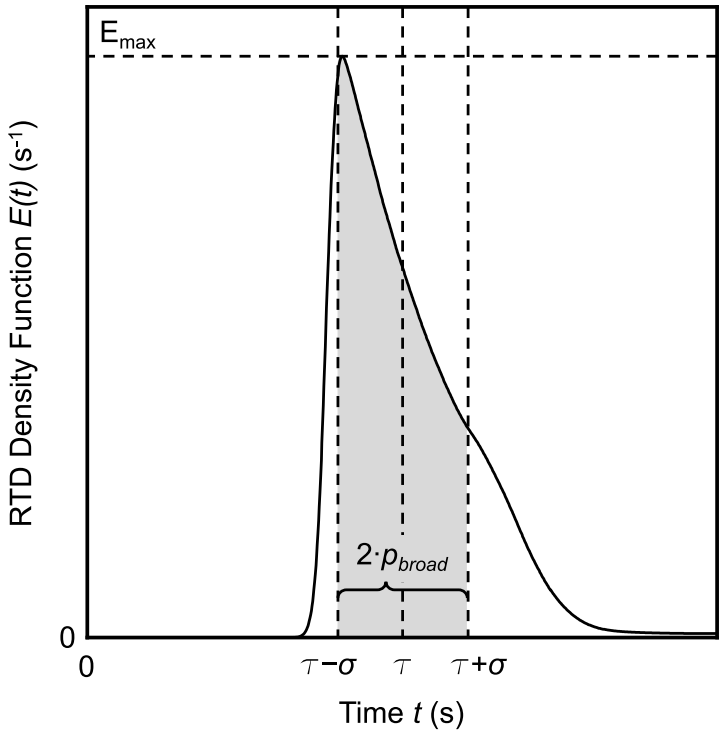

Figure 5.5: Visualization of evaluation parameter peak broadening p_{broad}.

Peak Symmetry

For the calculation of the RTD curve's symmetry, the mirror-image analysis was used as described in Section 2.3.3. The left tail of the curve was mirrored along the vertical axis at the curve's maximum $t(E_{max})$. Then the absolute area between the right and mirrored tail was calculated as visualized in Figure 5.6. The more symmetrical the curve is, the closer both tails are to each other. Due to the area under the $E(t)$ curve equaling unity, the peak's symmetry parameter p_{sym} ranges from 0 to 1.

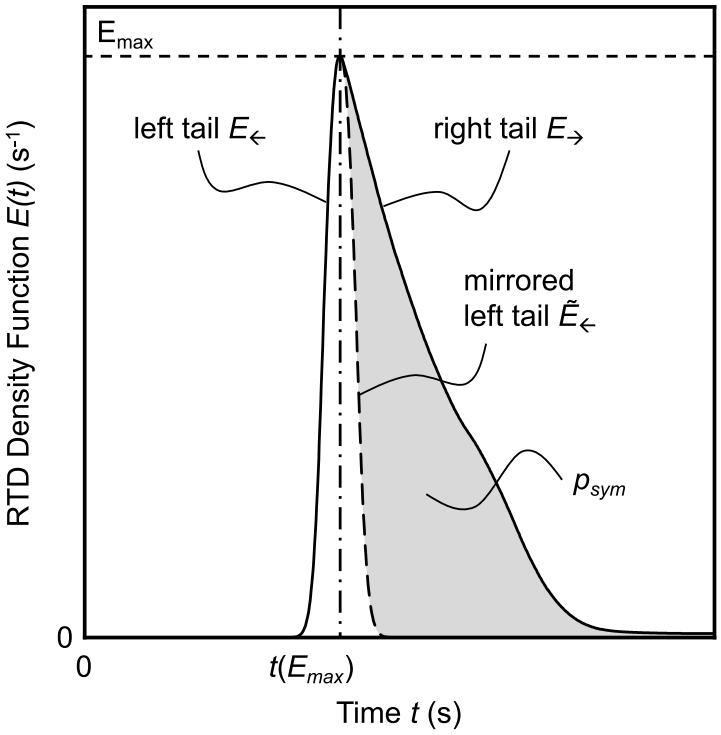

Figure 5.6: Visualization of evaluation parameter peak symmetry p_{sym}.

In the following Equation 5.4, $E_{\leftarrow}(t)$ and $E_{\rightarrow}(t)$ represent the curve's left and right tail, respectively. The mirrored left tail is calculated as $\widetilde{E}_{\leftarrow}(t) = E_{\leftarrow}(2 \cdot t_{max} - t)$. Thus the area between mirrored left tail and right tail is the integral over their absolute difference:

$$p_{sym} = \int_{t_{max}}^{\infty} \left| E_{\rightarrow}(t) - \widetilde{E}_{\leftarrow}(t) \right| \qquad p_{sym} \in [0,1] \qquad (-) \qquad (5.4)$$

$$\text{with} \quad E_{\rightarrow}(t) = E(t \geq t(E_{max})) \qquad (5.5)$$

$$\text{and} \quad E_{\leftarrow}(t) = E(t \leq t(E_{max})) \qquad (5.6)$$

5.2.4 Bayesian Optimization

The optimization was performed by the MATLAB function *bayesopt* and followed the iteration loop as shown in Figure 5.7. The first iteration started by feeding the initial values in MATLAB to create the simulation model. This model was sent to COMSOL to perform the simulation of study 1, study 2, and to extract the results. Those results were passed back to MATLAB to calculate the RTD and optimization parameters. *Bayesopt* then evaluated *p* with the acquisition function *expected-improvement* and generated a new set of model parameters for the next iteration taking into account the limits and dependencies of each parameter. The number

of iterations was set to 30 for the first and second set.

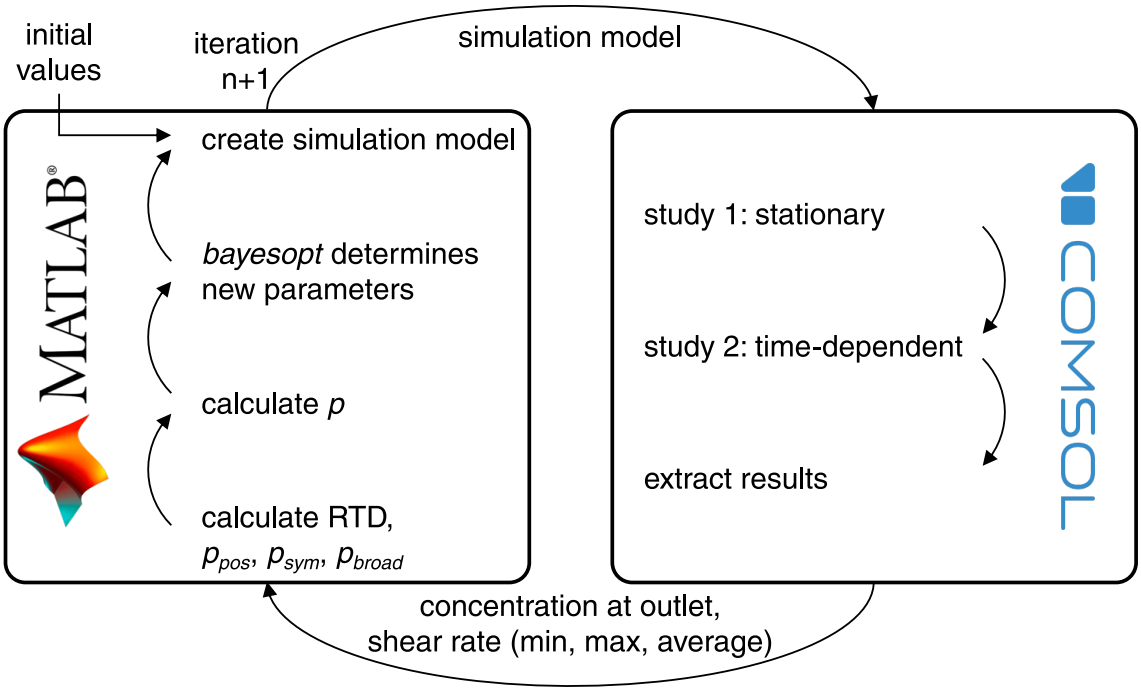

Figure 5.7: Schematic of the optimization process. In the first iteration, the initial values in MATLAB are used to create the simulation model. This model is transferred to COMSOL for both stationary and time-dependent studies. COMSOL then extracts the results and passes them back to MATLAB for evaluation. Based on this evaluation, the *bayesopt* optimizer generates a new set of parameters to create an updated simulation model.

Setup for Domain Set

In addition to the setup from Sets 1 and 2, initial values were defined for optimizing the permeabilities. These comprise ten different permeabilities in the range $2 \cdot 10^{-10}$ to $2 \cdot 10^{-9}\,\mathrm{m}^2$, with each domain being assigned the same initial value. The number of iterations varied between 500 and 1000.

5.3 Results and Discussion

This study is divided into three sets. The first two sets addressed the optimization of the external geometry, in particular the inlet and outlet area. For this purpose, the inlet and outlet angles, the Bézier parameter and the fillet radius were varied. Set 1 examined the geometry with a Bézier parameter of 0. Set 2 added the Bézier parameter and was thus able to examine concave and convex inlet and outlet areas. In Set 3, building upon the outer geometry from Set 2, the fluid volume was sectioned into domains. Each domain was assigned a variable permeability to further optimize residence time and flow.

5.3.1 Optimization of the Outer Geometry with Straight Tapering at In and Outlet

This first set varied the inlet α_{in} and outlet α_{out} angles along with the fillet radius r_{fillet}. The parameter b remained set to 0, rendering the Bézier curve equivalent to a straight line. A single domain with a permeability value of $\kappa_1 = 7.24 \cdot 10^{-10}\,\mathrm{m}^2$, derived from Santos et al was utilized. This permeability corresponds to a Schwarz diamond TPMS structure with $s_{unit} = 3.25\,\mathrm{mm}$ [Sant2020]. Four distinct cases were explored, each focusing on optimizing different parameter combinations:

- Case 1.1: $\alpha_{in} = \alpha_{out} \in [21.45, 55.66]$ and $r_{fillet} = 0$
- Case 1.2: $\alpha_{in} = \alpha_{out} \in [21.45, 55.66]$ and $r_{fillet} \in (0, 4]$
- Case 1.3: $\alpha_{in}, \alpha_{out} \in [21.45, 68.47]$ and $r_{fillet} = 0$
- Case 1.4: $\alpha_{in}, \alpha_{out} \in [21.45, 68.47]$ and $r_{fillet} \in (0, 4]$

Cases 1.1 and 1.2 maintained equal inlet and outlet angles, with Case 1.2 also varying the fillet radius. Cases 1.3 and 1.4 allowed independent inlet and outlet angles, with Case 1.4 also incorporating changes to the fillet radius.

Table 5.1 presents the optimal parameters from these investigations. In every case, both inlet and outlet angles approached their maximum of 55.66°. Cases 1.3 and 1.4, featuring independent angles, exhibited near-symmetrical geometries, with inlet and outlet angles closely matched. The fillet radius consistently leaned towards its maximum of 4 mm.

Table 5.2 lists the maximum and average simulated shear rates ($\dot{\gamma}_{max}$ and $\dot{\gamma}_{av}$) for each case, alongside optimization evaluation parameters p_{pos}, p_{broad}, p_{sym}, and p, the latter being the sum of squares of the first three. Lower p-values indicate a

Table 5.1: Best observed parameters from optimization simulations of Set 1 with $b_{in} = b_{out} = 0$. α_{in}, α_{out}, and r_{fillet} are optimization parameters in different combinations. Case 1.1 to 1.4 are the best of each optimization simulation and Case 1 is the conclusion of the entire set.

	Case	Best observed α_{in} [°]	α_{out} [°]	b_{in} [-]	b_{out} [-]	r_{fillet} [mm]
1.1	$\alpha_{in} = \alpha_{out} \in [21.45, 55.66]$ $r_{fillet} = 0$	55.66	55.66	0	0	0
1.2	$\alpha_{in} = \alpha_{out} \in [21.45, 55.66]$ $r_{fillet} \in (0, 4]$	55.66	55.66	0	0	3.89
1.3	$\alpha_{in} \neq \alpha_{out} \in [21.45, 68.47]$ $\alpha_{max}(L_{mod} \leq 100\,\text{mm})$ $r_{fillet} = 0$	57.66	53.34	0	0	0
1.4	$\alpha_{in} \neq \alpha_{out} \in [21.45, 68.47]$ $\alpha_{max}(L_{mod} \leq 100\,\text{mm})$ $r_{fillet} \in (0, 4]$	53.81	57.32	0	0	3.11

closer approximation to ideal RTD. Compared to the reference module (Case 0), all cases demonstrated significant improvements. Increased inlet and outlet angles facilitated smoother transitions from tubing to module, effectively reducing all *p*-values and shear rates, particularly when fillets were incorporated.

Comparing Cases 1.1 to 1.4 reveals minor differences in peak position, broadening, and symmetry. However, significant disparities were observed in maximum shear rates, attributed to the rounding of module edges. In Cases 1.2 and 1.4, the maximum shear rate decreased by approximately 50 %. As Figure 5.8 indicates, the maximum shear rate decreases with greater fillet radii, reaching its lowest at a radius of 3.8 mm. Nonetheless, suspected mesh inadequacies and numerical variances might explain the unexpected fluctuations in an otherwise steadily decreasing trend. Hence, this best overall result for this first set, including the *p*-value and shear rate, is yielded with $\alpha_{in} = \alpha_{out} = 55.66°$ and $r_{fillet} = 4$ mm. These parameters were simulated as Case 1 for which the geometry is illustrated in Figure 5.9. Notably, the *p*-value is slightly higher than in Case 1.2 but at a benefit in shear rate. As previously stated, suspected mesh inadequacies and numerical variances only allow for qualitative analysis, but satisfy the aim of this first set.

Consequently, Set 1's optimal geometry has inlet and outlet angles of $\alpha_{in} = \alpha_{out} = 55.66°$ and a fillet radius of $r_{fillet} = 4$ mm (Case 1). The RTD density function for

Table 5.2: Results of optimization simulations of Set 1, where $b_{in} = b_{out} = 0$. Case 0 is the reference module. Case 1.1 to 1.4 are optimization simulations and Case 1 is the result of the conclusion of 1.1 to 1.4. $\dot{\gamma}_{max}$ is the maximum occurring shear rate in the entire module and $\dot{\gamma}_{av}$ is the module's average shear rate.

	Case	$\dot{\gamma}_{max}$ [s^{-1}]	$\dot{\gamma}_{av}$ [s^{-1}]	p_{pos} [-]	p_{broad} [-]	p_{sym} [-]	p [-]
0	$\alpha_{in} = \alpha_{out} = 21.45°$ $r_{fillet} = 0$ mm	16 197	9.33	0.91	0.98	0.68	2.26
1.1	$\alpha_{in} = \alpha_{out} = 55.65°$ $r_{fillet} = 0$ mm	11 365	7.75	0.33	0.53	0.46	0.60
1.2	$\alpha_{in} = \alpha_{out} = 55.66°$ $r_{fillet} = 3.67$ mm	8260	7.46	0.34	0.53	0.47	0.62
1.3	$\alpha_{in} = 55.52°$ $\alpha_{out} = 55.75°$ $r_{fillet} = 0$ mm	11 623	7.75	0.34	0.53	0.47	0.62
1.4	$\alpha_{in} = 54.70°$ $\alpha_{out} = 56.41°$ $r_{fillet} = 3.51$ mm	8419	7.52	0.34	0.54	0.47	0.63
1	$\alpha_{in} = \alpha_{out} = 55.66°$ $r_{fillet} = 4$ mm	8260	7.45	0.36	0.53	0.50	0.67

Case 1, illustrated in Figure 5.10, shows that larger angles at the inlet and outlet effectively narrow the RTD, shifting its peak closer to the mean residence time. Despite an early maximum (fronting) and a residual shoulder post-maximum, likely due to wall effects and suboptimal flow near the fillets, the RTD beneath the shoulder is remarkably symmetrical. In summary, larger angles enhance RTD significantly, while fillets, though not affecting RTD directly, reduce the maximum shear rate, promoting more uniform flow conditions.

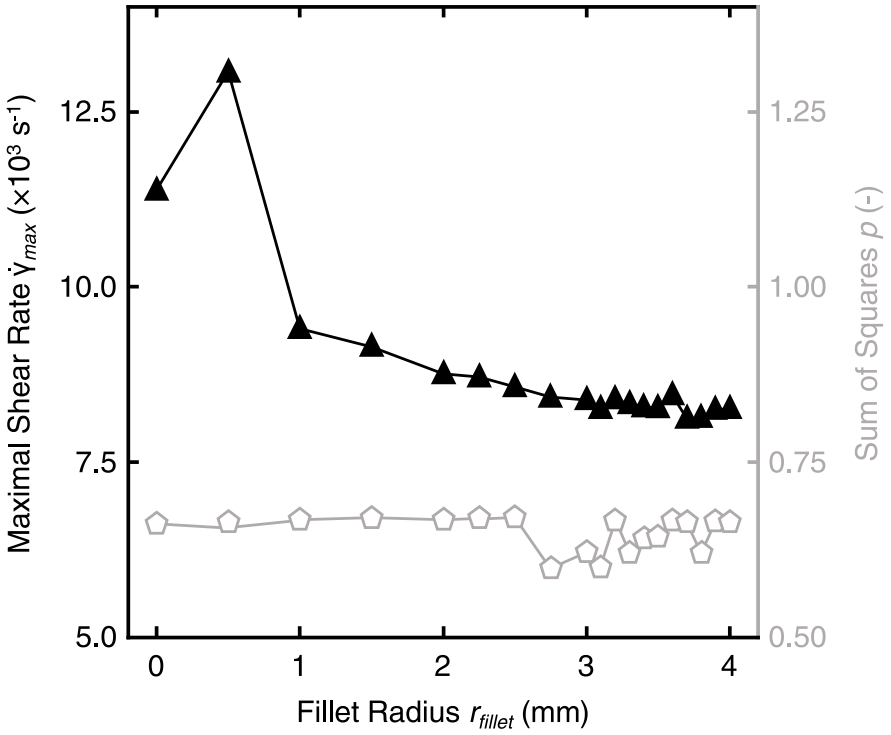

Figure 5.8: Maximum shear rate $\dot{\gamma}_{max}$ in $\times 10^3\,s^{-1}$ and sum of squares p plotted over the fillet radius r_{fillet} for a geometry with $\alpha_{in} = \alpha_{out} = 55.66°$. ▲ represent the maximum shear rate and belong to the left y-axis. ⬠ represent the sum of squares and belong to the right y-axis. The maximum shear rate decreases as the fillet radius increases.

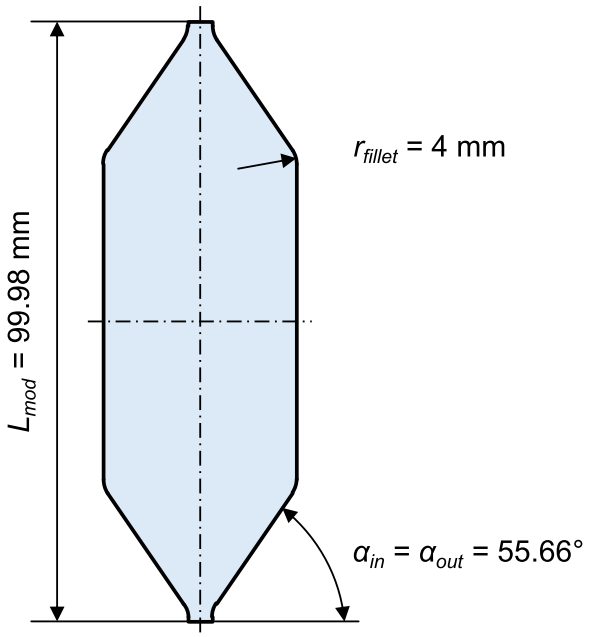

Figure 5.9: Optimized geometry concluding from Set 1 (Case 1).

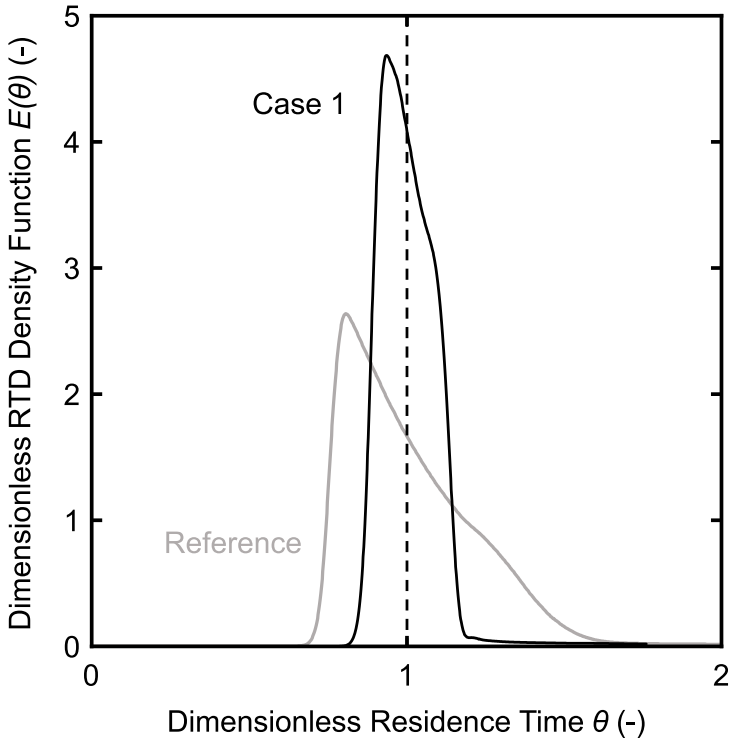

Figure 5.10: Resulting RTD density function $E(\theta)$ of the parameter set concluding from Set 1 (Case 1). The profiles of the RTD curves for Cases 1.1 to 1.4 deviate only minimally from the curve for Case 1, wherefore only Case 1 is presented for better visibility. Compared to the reference curve (gray line), the RTD has been improved considerably. The curve is clearly narrower, higher and more symmetrical.

5.3.2 Optimization of Outer Geometry with Bézier Curve for Tapering at In and Outlet

Following on from the first set, this second set incorporates the Bézier parameter *b*. Positive *b* values yield a convex shape, while negative ones result in a concave shape. The parameter is restricted to the range between -0.3 and 0.3 to prevent the creation of inefficient flow paths that arise from protrusions outside this range. Values more negative than -0.3 result in an indented inlet shape, as the Bézier curve no longer aligns tangentially. Values exceeding 0.3 cause the formation of a pocket at the inlet because the Bézier curve forms an angle greater than 90° with the inlet structure. The fillet radius's upper limit is now 3.2 mm to ensure error-free geometrical configurations. Apart from these modifications, all other parameters mirror those from the initial set, thus yielding four cases:

- Case 2.1: $\alpha_{in} = \alpha_{out} \in [21.45, 55.66]$, $b_{in} = b_{out} \in [-0.3, 0.3]$, and $r_{fillet} = 0$
- Case 2.2: $\alpha_{in} = \alpha_{out} \in [21.45, 55.66]$, $b_{in} = b_{out} \in [-0.3, 0.3]$, and $r_{fillet} \in [0, 3.2]$

- Case 2.3: α_{in}, $\alpha_{out} \in [21.45, 68.47]$, $b_{in}, b_{out} \in [-0.3, 0.3]$, and $r_{fillet} = 0$
- Case 2.4: α_{in}, $\alpha_{out} \in [21.45, 68.47]$, $b_{in}, b_{out} \in [-0.3, 0.3]$, and $r_{fillet} \in [0, 3.2]$

Table 5.3 presents the optimal parameters identified. In each instance, only the most effective parameters were selected, highlighting a preference for inlet and outlet angles near their maximum of 55.66°. Notably, Cases 2.3 and 2.4, with independent angles, led to only slightly asymmetrical geometries, and the fillets' radius typically settled in the middle of its range.

Table 5.3: Best observed parameters from optimization simulations of Set 2. α_{in}, α_{out}, b_{in}, b_{out}, and r_{fillet} are optimization parameters in different combinations. Case 2.1 to 2.4 are the best of each optimization simulation.

	Case	Best observed α_{in} [°]	α_{out} [°]	b_{in} [-]	b_{out} [-]	r_{fillet} [mm]
2.1	$\alpha_{in} = \alpha_{out} \in [21.45, 55.66]$ $b_{in} = b_{out} \in [-0.3, 0.3]$ $r_{fillet} = 0$	55.65	55.65	0.13	0.13	0
2.2	$\alpha_{in} = \alpha_{out} \in [21.45, 55.66]$ $b_{in} = b_{out} \in [-0.3, 0.3]$ $r_{fillet} \in [0, 3.2]$	55.65	55.65	0.14	0.14	2.19
2.3	$\alpha_{in} \neq \alpha_{out} \in [21.45, 68.47]$ $\alpha_{max}(L_{mod} \leq 100\,\text{mm})$ $b_{in} \neq b_{out} \in [-0.3, 0.3]$ $r_{fillet} = 0$	55.26	55.75	0.13	0.13	0
2.4	$\alpha_{in} \neq \alpha_{out} \in [21.45, 68.47]$ $\alpha_{max}(L_{mod} \leq 100\,\text{mm})$ $b_{in} \neq b_{out} \in [-0.3, 0.3]$ $r_{fillet} \in [0, 3.2]$	53.66	57.37	0.15	0.16	1.84

Table 5.4 provides data on maximum and average simulated shear rates for the respective cases, alongside optimization evaluation parameters p_{pos}, p_{broad}, p_{sym}, and their sum of squares p. For context, Case 1's data from the first set is included. Compared to Case 1, all cases exhibit enhanced p-values. Although Case 1 shows a superior maximum shear rate, attributable to the larger fillet radius, the reduction of average shear rate achieved through the Bézier curve is noteworthy.

An optimal range for the Bézier parameter appears to be at around 0.15. Figure 5.11 illustrates the relationship between p and the maximum shear rate across the b parameter range for a module with $\alpha_{in} = \alpha_{out} = 55.66°$ and $r_{fillet} = 3.2\,\text{mm}$. A minimum around $b = 0.15$ is evident, with negligible impact on the maximum

Table 5.4: Results of optimization simulations of Set 2. Case 1 is the result from the previous section as comparison. Case 2.1 to 2.4 are optimization simulations and Case 2 is the result of the conclusion of 2.1 to 2.4. $\dot{\gamma}_{max}$ is the maximum occurring shear rate in the entire module and $\dot{\gamma}_{av}$ is the module's average shear rate.

	Case	$\dot{\gamma}_{max}$ [s^{-1}]	$\dot{\gamma}_{av}$ [s^{-1}]	p_{pos} [-]	p_{broad} [-]	p_{sym} [-]	p [-]
1	$\alpha_{in} = \alpha_{out} = 55.66°$ $r_{fillet} = 4$ mm	8260	7.45	0.36	0.53	0.50	0.67
2.1	$\alpha_{in} = \alpha_{out} = 55.65°$ $b_{in} = b_{out} = 0.13$ $r_{fillet} = 0$ mm	12 332	7.19	0.29	0.49	0.42	0.50
2.2	$\alpha_{in} = \alpha_{out} = 55.65°$ $b_{in} = b_{out} = 0.14$ $r_{fillet} = 2.19$ mm	8671	6.84	0.29	0.50	0.42	0.52
2.3	$\alpha_{in} = 55.26°$ $\alpha_{out} = 55.75°$ $b_{in} = 0.13$ $b_{out} = 0.13$ $r_{fillet} = 0$ mm	12 354	7.18	0.30	0.49	0.43	0.52
2.4	$\alpha_{in} = 53.66°$ $\alpha_{out} = 57.37°$ $b_{in} = 0.15$ $b_{out} = 0.16$ $r_{fillet} = 1.84$ mm	8939	6.83	0.29	0.51	0.41	0.51
2	$\alpha_{in} = \alpha_{out} = 55.66°$ $b_{in} = b_{out} = 0.14$ $r_{fillet} = 3.2$ mm	8405	6.68	0.31	0.50	0.44	0.54

shear rate. The lowest maximum shear rate is found at $b = -0.3$, the geometry of which is depicted in Figure 5.12a. Here, the concave shape allows a gradual inlet widening, slowing the flow and reducing abrupt transitions that cause high shear rates. Nonetheless, this geometry results in a less favorable RTD due to a rapidly increasing p.

The results for Cases 2.1 to 2.4 show that the algorithm determined an inlet and outlet angle close to the maximum allowable as optimal. Consideration of the maximum shear rate and the optimization parameter over the Bézier parameter results in an optimum at $b = 0.14$. These findings and the insight from Set 1, which indicated that larger fillet radii contribute to lower shear rates, Case 2 consolidates

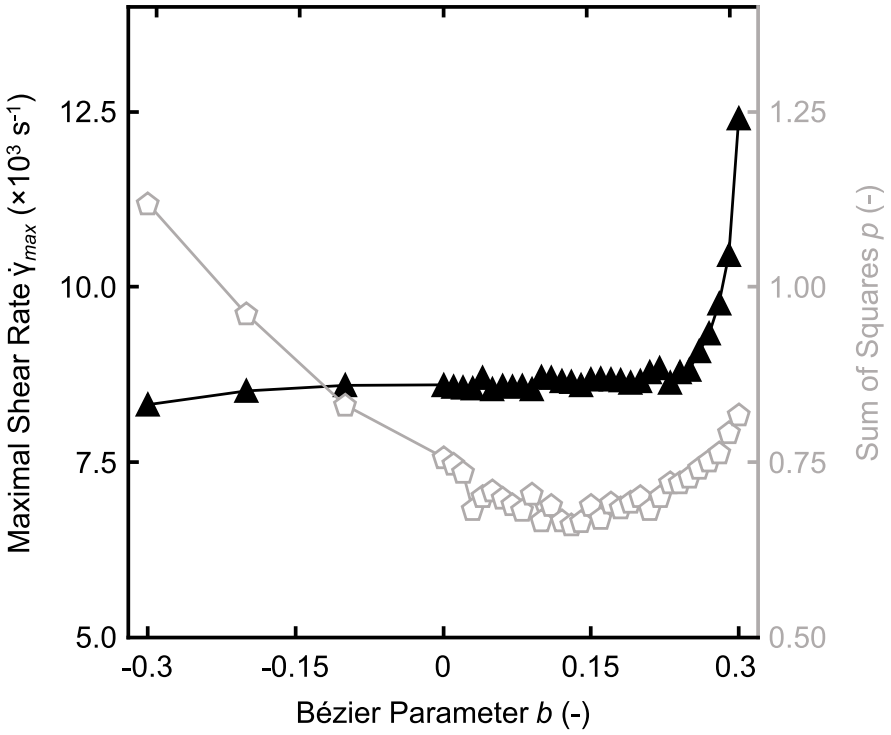

Figure 5.11: Maximum shear rate $\dot{\gamma}_{max}$ in $10^3\,s^{-1}$ and sum of squares p plotted over the Bézier parameter b for a geometry with $\alpha_{in} = \alpha_{out} = 55.66°$ and $r_{fillet} = 3.2\,mm$. ▲ represent the maximum shear rate and belong to the left y-axis. ⬠ represent the sum of squares and belong to the right y-axis. The sum of squares decreases as the Bézier parameter increases until a minimum at $b = 0.13$. Around this b-value the lowest maximum shear rate is $8405\,s^{-1}$ for $b = 0.14$.

the findings of the second set. As shown in Table 5.4, Case 2 records a slight increase in the maximum shear rate but a decrease in the average shear rate, with negligible changes in p-values. This increase in the maximum shear rate is attributed to the smaller fillet radius of 3.2 mm, compared to 4 mm used in Case 1. Figure 5.12b illustrates Case 2's geometry, which has a slightly convex shape. As depicted in Figure 5.11, inlet and outlet geometries that are concave tend to minimize the maximum shear rate. Therefore, a combination of concave and convex Bézier curves, forming an "S" shape, may offer further improvements, although this extends beyond the scope and objectives of this chapter.

Figure 5.13 shows the RTD curve for Case 2 that significantly outperforms the reference curve (gray line). While the peak maximum approaches the expected mean residence time and the post-peak shoulder is more pronounced, the curve remains more symmetrical below this shoulder compared to Case 1 (dashed line). Thus, the introduction of a Bézier curve as a transitional element primarily reduces the average shear rate and modestly improves the RTD.

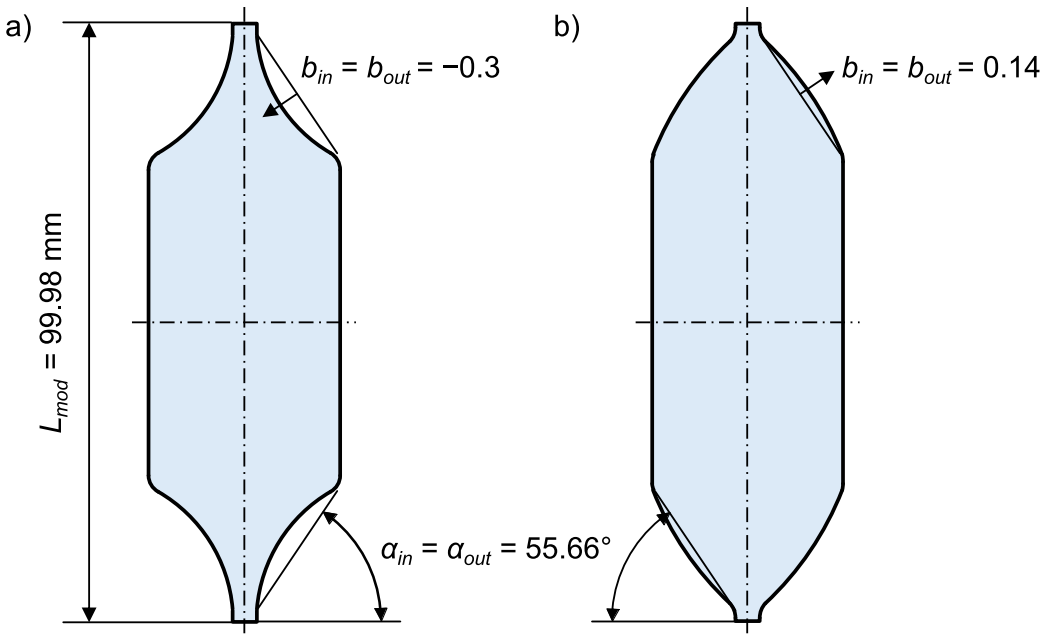

Figure 5.12: a) Geometry with $b = -0.3$ exhibiting the lowest maximum shear rate of 7976 s^{-1} and b) optimized geometry with $b = 0.14$ as conclusion of Set 2 (Case 2).

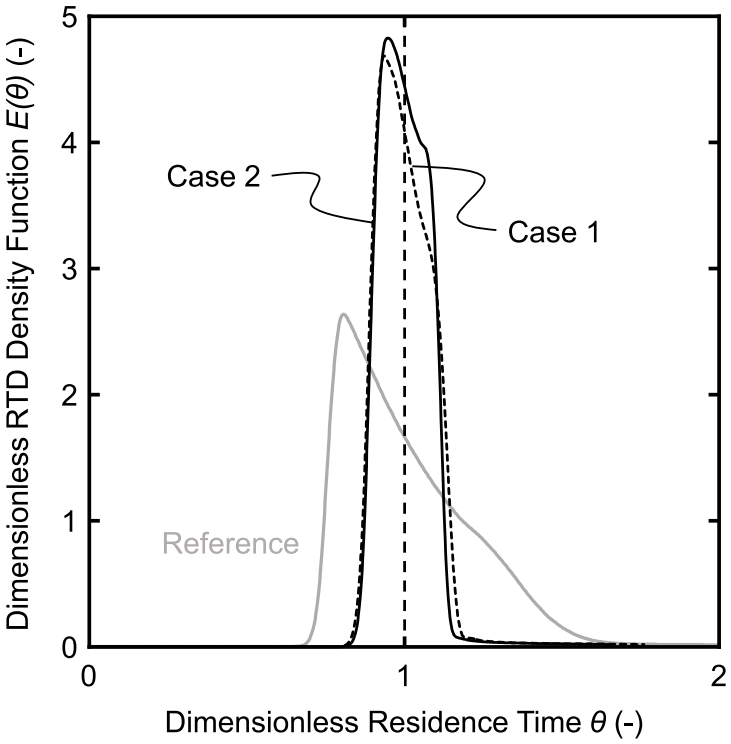

Figure 5.13: Resulting RTD density function $E(\theta)$ of the parameters concluding from Set 2 (Case 2). The profiles of the RTD curves for Cases 2.1 to 2.4 deviate only minimally from the curve for Case 2, wherefore only Case 2 is presented for better visibility. Compared to the reference curve (gray line), the RTD has been improved considerably. Compared to Case 1 (dashed line), the peak maximum is a little closer to the expected mean and the post-peak shoulder is more pronounced, but the curve below the shoulder is more symmetrical.

5.3.3 Optimization of Inner Geometry by Domains with Variable Permeabilities

Although significant improvements have been achieved by varying and optimizing the external geometry, the RTD curve still displays some minor deviations from the ideal, including an early peak and shoulder. These deviations are linked to slower fluid and tracer movement through the module's peripheral areas compared to its central path. This discrepancy could be mitigated by modifying local flow resistances. In simulations, fluid flow resistance is determined by permeability, denoted as κ.

To facilitate local changes in permeability, the module was segmented into $n_{vertical}$ and n_{radial} equidistant domains, as illustrated in Figure 5.3. Each cylinder segment was assigned a specific permeability value, κ_n, by the optimization algorithm. Transitioning from simulation to real-world manufacturing, the permeability of each TPMS unit cell varies, with smaller unit cells being less permeable than larger ones. It is essential to define the permeability range with consideration for TPMS structures that are feasible for additive manufacturing to ensure the practical application of simulation results. Typically, 3D printers can achieve resolutions of about 500 µm. For a porosity of 50 %, this implies a minimum unit cell size of 1 mm, establishing the lower boundary for permeability. Conversely, the upper limit is determined by the inlet module diameter of 4 mm, equating to a maximum TPMS unit cell size of 8 mm.

Experimental data from Santos et al. provide permeabilities for Schwarz diamond TPMS structures with 3.25 mm unit cells and 50 to 80 % porosities, where a 50 % porosity corresponds to $7.24 \cdot 10^{-10}\,\mathrm{m}^2$ permeability [Sant2020]. However, Santos et al.'s data is inadequate for defining all constants in Equation 2.17. Therefore, only the second order term in Equation 2.17 was used, replacing s_{chan} with s_{unit} in Equation 2.16. This simplification yields $c_1\phi - c_2 = 6.85 \cdot 10^{-5}$. To maintain a manageable range, values are rounded, resulting in $\kappa_n \in [2 \cdot 10^{-10}\,\mathrm{m}^2, 2 \cdot 10^{-9}\,\mathrm{m}^2]$. Note that the outer geometry remains unchanged during optimization.

Figure 5.14a illustrates the geometry, color-coded to represent the permeabilities resulting from an optimization that segmented the module's fluid volume into two radial and two vertical domains (Case 3.1). In 5.14b, the tracer concentration within the module is displayed at different times (t = 2 s, 4 s and 6 s), revealing an intriguing pattern: the permeability in the lower domains is almost uniform ($\kappa_1 \approx \kappa_3$).

However, in the upper half, the permeabilities differ ($\kappa_4 > \kappa_2$), leading to quicker fluid and tracer movement in the outer area, which then aligns with the flow in the inner area.

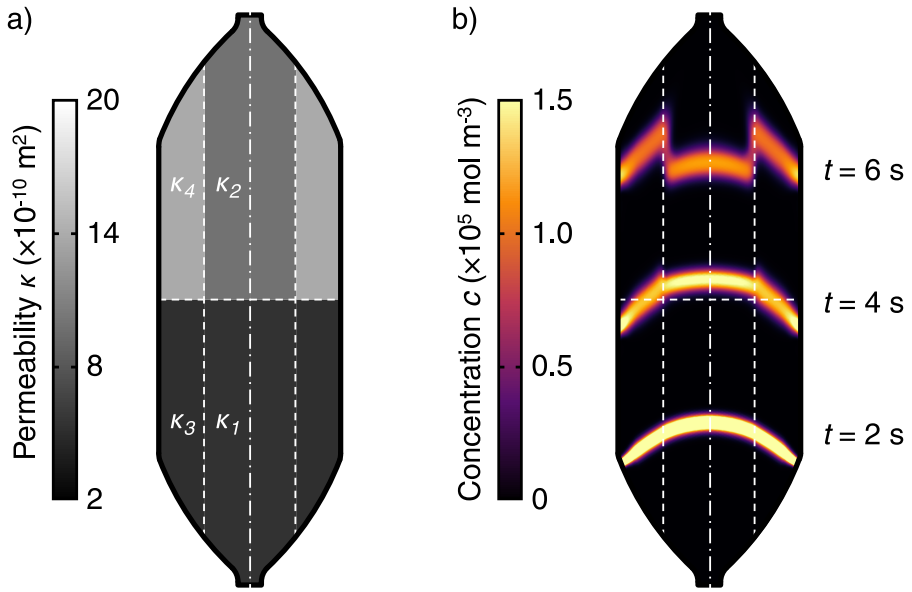

Figure 5.14: Resulting permeabilities for an optimization with segmentation into 2x2 domains (Case 3.1), two radial and two vertical domains. Depicted is the entire cross-section with a vertical central mirror axis. a) Geometry colored according to permeability, where darker regions are less permeable and brighter regions are more permeable. b) Concentration profile for different time steps.

The corresponding RTD density function is shown in Figure 5.15, where it is compared with the reference module and the findings from Case 2. This curve is notably symmetric and narrow, with its peak very close to $\theta = 1$, as supported by the *p*-values in Table 5.5. Although there's some scope for reducing the broadening value, it's important to recognize that longitudinal diffusion cannot be completely eliminated and thus a spike-like RTD is physically impossible. In terms of shear rate, the values are on par with those from previous sets with slight increases in maximum shear rate (7 %) and average shear rate (3 %) compared to Case 2. The inlet and outlet regions continue to be the zones of maximum shear rate.

The 2x2 case (Case 3.1) results demonstrate that varying permeabilities can nearly optimize the RTD curve. However, this configuration also results in undesirable discontinuities at domain boundaries due to major differences in permeability between adjacent domains. Reflecting on the translation between permeability and TPMS unit cell size, such discontinuities cannot be mapped with gradually merging

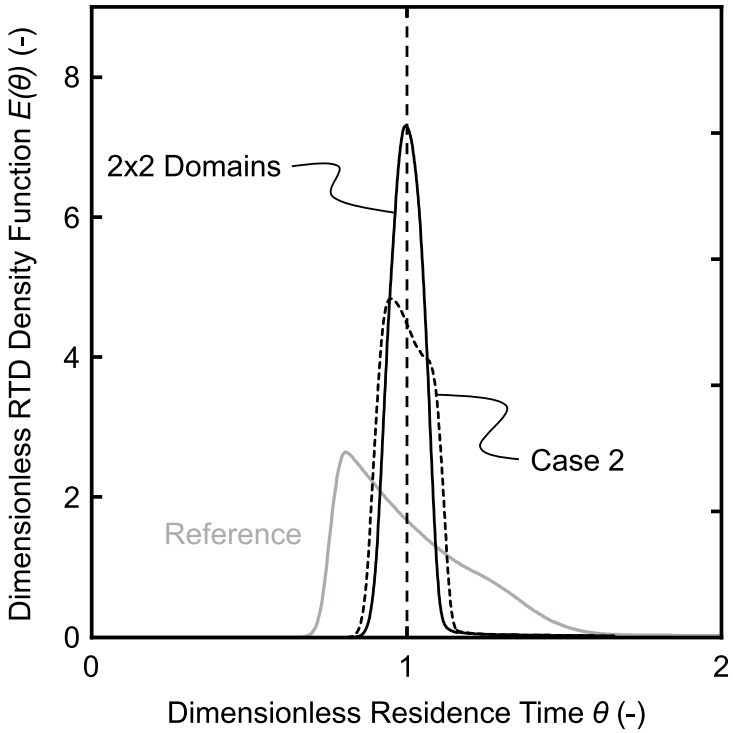

Figure 5.15: Resulting density function $E(\theta)$ for geometry with 2x2 domains in comparison to the reference module (gray line) and Case 2 (dashed line).

Table 5.5: Results of optimization simulations of Set 3. $\dot{\gamma}_{max}$ is the maximum occurring shear rate in the entire module and $\dot{\gamma}_{av}$ is the module's average shear rate.

Case		$\dot{\gamma}_{max}$ [s^{-1}]	$\dot{\gamma}_{av}$ [s^{-1}]	p_{pos} [-]	p_{broad} [-]	p_{sym} [-]	p [-]
3.1	(2x2)	9023	6.86	0.03	0.41	0.05	0.17
3.2	(4x4)	6302	7.87	0.02	0.46	0.06	0.21

unit cells. Ideally, the tracer front moves evenly and horizontally from the bottom to the top of the module. To facilitate smoother transitions between the domains, the number of domains was increased to a 4x4 grid.

The outcomes from the 4x4 setup (Case 3.2), depicted in Figure 5.16, present an extreme contrast. In 5.16a the domain's permeabilities show no discernible pattern, indicating that simply increasing the number of domains does not necessarily lead to more uniformity. Despite assuming a gradual permeability change across domains, large discrepancies persist, similar to the 2x2 configuration. In 5.16b, while the tracer shows almost horizontal movement at $t = 2\,s$ in the peripheral regions, it travels faster in the center, increasing the lateral offset toward the outlet.

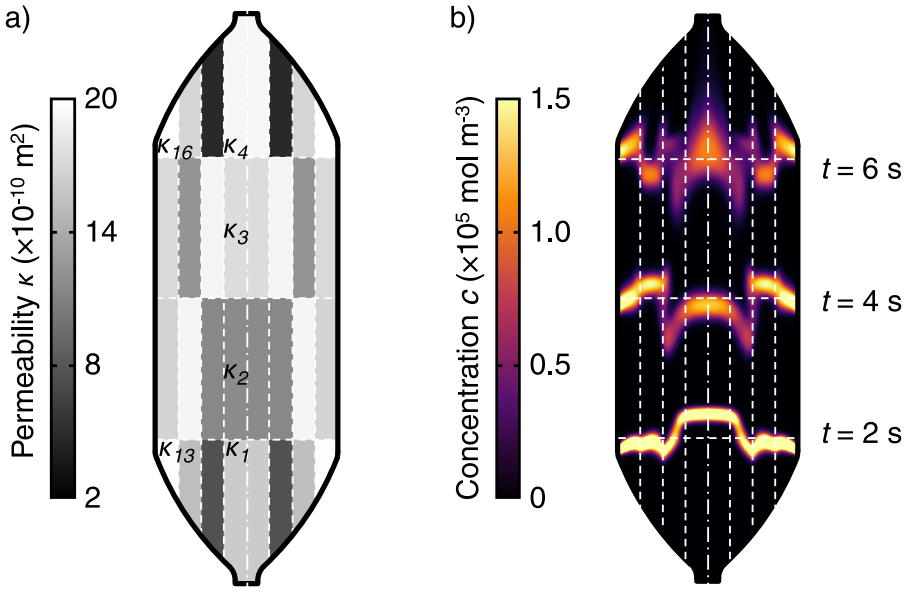

Figure 5.16: Resulting permeabilities for an optimization with segmentation into 4x4 domains (Case 3.2), four radial and four vertical domains. Depicted is the entire cross-section with a vertical central mirror axis. a) Geometry colored according to permeability, where darker regions are less permeable and brighter regions are more permeable. b) Concentration profile at different time steps.

Even after 1000 iterations, the optimization of the 4x4 domains did not improve the overall *p*-value compared to the 2x2 setup. While the position and symmetry measurements are similar, the broadening has slightly worsened, as detailed in Table 5.5. Although the maximum shear rate drastically decreased, the average shear rate increased. Introducing more domains enhances resolution but complicates the problem due to the independence of the domains, which leads to jumps in permeability. Addressing this requires additional constraints to limit permeability variations between neighboring domains, which could be implemented in MATLAB with sufficient coding knowledge.

A direct comparison reveals that the 4x4 setup exhibits even larger permeability differences between adjacent domains than the 2x2 setup. For the 2x2 case the greatest horizontal difference is between domain 2 and 4 with $\Delta\kappa_{2-4} = 3.93 \cdot 10^{-10}\,\mathrm{m}^2$ and the greatest vertical difference is between domain 3 and 4 with $\Delta\kappa_{3-4} = 8.62 \cdot 10^{-10}\,\mathrm{m}^2$. In the 4x4 case the greatest horizontal difference is $\Delta\kappa_{4-8} = 14.44 \cdot 10^{-10}\,\mathrm{m}^2$ and the greatest vertical difference is $\Delta\kappa_{7-8} = 14.32 \cdot 10^{-10}\,\mathrm{m}^2$.

Despite these challenges, the RTD curve for the 4x4 setup, shown in Figure 5.17,

remains well-aligned, narrow, and symmetrical. The lower portion is broader, and the left tail displays a small shoulder. Compared to the 2x2 case, the upper part of the curve is even narrower, resulting in a higher peak.

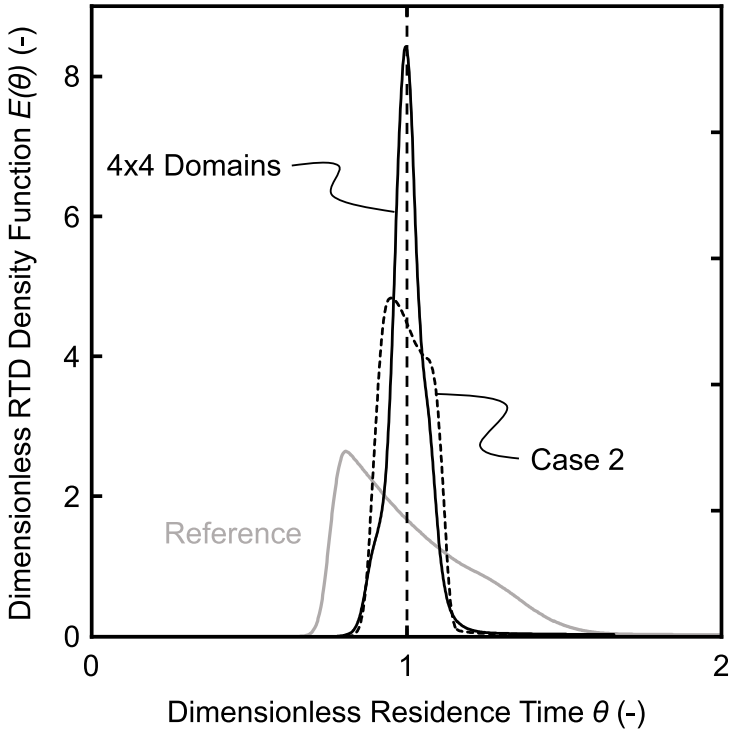

Figure 5.17: Resulting density function $E(\theta)$ for geometry with 4x4 domains in comparison to the reference module (gray line) and Case 2 (dashed line).

5.4 Conclusion and Outlook

The objective of this chapter focused on optimizing fluid flow through a module designed for extracorporeal blood applications. To achieve this, both the external and internal geometry of the module was enhanced through simulative Bayesian optimization, aiming for a more uniform flow distribution. The flow distribution was quantified using RTD measurements, characterized by three RTD parameters: position, broadening, and symmetry. Initially, modifications to the external geometry yielded a substantial improvement in RTD parameters compared to a reference geometry ($-76\,\%$). Subsequently, introducing anisotropy by segmenting the internal geometry into domains with different permeabilities led to further enhancements in RTD parameters compared to modifications to the external geometry ($-69\,\%$).

In terms of permeability assumptions, the values used derive from Santos et al. and are specific to flow rates between 1 to 10 $\mathrm{mL\,min^{-1}}$. Research by Asbai-Ghoudan et al., conducted at Reynolds number (Re) = 1, demonstrates that permeability is independent of flow rate [Asba2021]. Yet, when considering higher Reynolds numbers and flow rates, the applicability becomes uncertain. To tackle this, further experimental validation is necessary, not only to corroborate the simulation results but also to develop an equation that correlates permeability with TPMS unit cell size and porosity.

By segmenting the fluid volume into multiple domains with varying permeability, the module's flow distribution can be manipulated. The optimization process, under chosen boundary conditions, resulted in pronounced anisotropy - neighboring domains exhibited significantly different permeabilities. Transitioning to an anisometric TPMS structure is challenging due to the required connection of small to large unit cells, necessitating a boundary condition to limit the permeability gradient.

Furthermore, Bayesian optimization is a single-objective optimization method, thus the challenge lies in consolidating target variables. The current approach used the sum of squares, treating all variables equally. However, this raises questions about the realistic boundaries of the optimization parameters and whether the actual feasible range is smaller or larger than assumed. For instance, while a curve's maximum at $\theta = 1$ ($p_{pos} = 0$) is realistic, a broadening value of 0 (implying an impulse) is non-physical due to axial diffusion. The reference values for position, broadening, and symmetry, suggest varying degrees of realism within the feasible range. This leads to a dilemma of whether to optimize universally or in relation

to a reference module. A target function could offer a more cohesive optimization approach.

The Thompson sampling efficient multi-objective optimization (TSEMO) strategy, as an alternative to Bayesian optimization, presents a compelling approach. TSEMO, a multi-objective optimization strategy, efficiently identifies minima for all output variables, forming what is known as a Pareto front [Brad2018]. This method stands in contrast to Bayesian optimization, as it allows for the weighting of output variables to be adjusted post-optimization. Such flexibility facilitates a more comprehensive and adaptable optimization process. However, during the simulation phase, the implementation of the TSEMO strategy and the subsequent weighting of variables appeared more complex compared to utilizing the readily available *bayesopt* function in Matlab. Additionally, focusing on locally observing the tracer front's movement through the module, rather than optimizing parameters describing the RTD curve, could lead to a more uniform perfusion of the module.

6.
Conclusion and Perspectives

Extracorporeal blood therapies use artificial devices to treat the patient's blood. Large surfaces are required for the treatment, provided by functional entities such as hollow fiber membranes or porous beads. The flow through the artificial devices is non-uniform and non-physiological, causing blood damage and immune reactions. However, due to the geometric limitations of the functional entities, perfusion cannot be adapted to the biological counterpart. Consequently, permanent use for patients with irreversibly damaged organs is impossible.

In commercial blood therapy devices, the blood inlet geometry has the biggest impact on blood distribution. Furthermore, blood usually coagulates in the hollow fiber bundle in regions of low flow and shear rates. Triply periodic minimal surfaces (TPMS) promise an improved blood perfusion and thus reduced blood damage and immune reactions. Anisometric TPMS further allow tailoring the residence time distribution (RTD) for optimal efficiency. However, the hemodynamics of TPMS and the influence of TPMS on blood have rarely been investigated.

Flow analysis Three perfusable modules with integrated TPMS structure were designed, of which two modules had an isometric TPMS structure with different unit cell sizes, and one had an anisometric TPMS structure. Compared to classical hollow fiber membrane modules, the entire inner void of each module was employed by the TPMS structure, yielding an increase in surface area to volume ratio. Experimental RTD measurements successfully validated the time-dependent simulation of a tracer passage through the modules. Therefore, the simulative investigation of the hemodynamics inside the modules made it possible to identify geometry-dependent zones of low and high flow velocities and shear rates prone to triggering blood clotting.

Structure-induced blood clotting In the follow-up study, the modules were continuously perfused with human whole blood to investigate the structure-induced blood coagulation. Besides the conventional measurement of pressure drop and platelet amount, the formed blood clots were post-experimentally visualized and quantified by computed tomography (CT) scanning. From the CT scans, the location of formed blood clots became visible, enabling cross-linking to the simulated hemodynamics, where identified regions with elevated shear rates correlate to regions of blood clot formation. Additionally, the overall amount of clotted blood inside the different modules revealed significantly lesser clot formation in an anisometric TPMS structure due to more physiological shear rates.

Optimization of blood contactors Critical flow regimes were identified from the simulative flow analysis and experimental investigation of blood clot formation, which helped to understand the bottlenecks of perfused blood contactors. These findings were used as the starting point for a series of optimization simulations to harmonize the flow conditions inside the modules and tailor the RTD for best module efficiency. Therefore, the module was subdivided into its outer shape and inner volume. Optimizing the outer shape simply by elongating the module yielded lower shear rates and a considerably better RTD. For simplicity, the inner volume was modeled as multiple domains of porous media, each assigned a permeability and porosity value. Through Bayesian optimization, the permeabilities were varied to further enhance RTD, showcasing the potential of anisotropy and closing the loop to the advanced performance of the anisometric TPMS module. With this procedure, the RTD can be optimally tailored within a given external shape, e.g., a lung lobe, to enable the design of patient-individualized devices.

Limitations All investigations presented in this thesis were carried out at a blood flow rate of 300 mL min^{-1}, which is a typical value for dialyzers and adsorbers but not for membrane lungs, which are operated at flow rates of up to 7 L min^{-1}. However, due to the small module volume of only 25 mL, the average residence time of 5 s corresponds to that of membrane lungs, whereas dialyzers and adsorbers have notably longer residence times of 10 to 30 s. Which flow rate and residence time combination is needed strongly depends on the device's performance, use case, and patient pathology. Nevertheless, the level of shear rate, in combination with exposure time, decides about the activation of blood components starting the coagulation cascade [Casa2015].

Furthermore, the presented work investigated and advanced the hemodynamics of blood-contacting devices, but the materials used did not provide any functionality for treating the blood. With steadily advancing technology and an increasing variety of materials for additive manufacturing, suitable processes for manufacturing blood-contacting support devices are emerging. For example, the 3D printing of a nanoporous material [Dong2021] or a UV curable and 3D printable polydimethylsiloxane (PDMS) [Flec2023], a widely used material in biological and medical applications, was already shown.

Perspectives Future research could investigate modules with smaller unit cells and a larger inner surface area at variable flow rates and a broader range of donors. Furthermore, the modules could be adapted to the properties of the donor blood in order to explore the possibilities of individualization. The individually optimized modules, which currently only exist in digital form, must be converted into physical modules, effectively bridging the gap between theoretical models and practical applications. This transition will involve comprehensive testing and validation to ensure the selected TPMS structure optimally replicates the simulated fluid properties and behaviors. In this process, the smooth and continuous transition of TPMS is crucial, and optimization algorithms will be pivotal in enhancing uniformity. Whether the Schwarz diamond TPMS is the best for extracorporeal blood therapies needs to be investigated.

Bibliography

[Anka2018] G. Ankawi, M. Neri, J. Zhang, A. Breglia, Z. Ricci, and C. Ronco. “Extracorporeal techniques for the treatment of critically ill patients with sepsis beyond conventional blood purification therapy: The promises and the pitfalls”. *Critical Care*, vol. 22, no. 1. Dec. 2018. DOI: 10.1186/s13054-018-2181-z (cit. on pp. 5, 30).

[Ansy] Ansys, Inc., *What is Computational Fluid Dynamics (CFD)?* [Online]. Available: https://www.ansys.com/simulation-topics/what-is-computational-fluid-dynamics (visited on 07/28/2024) (cit. on pp. 41, 44, 45).

[Aren2020] J. Arens, O. Grottke, A. Haverich, L. S. Maier, T. Schmitz-Rode, U. Steinseifer, H. Wendel, and R. Rossaint. “Toward a Long-Term Artificial Lung”. *ASAIO Journal*, vol. 66, no. 8. Aug. 2020. DOI: 10.1097/MAT.0000000000001139 (cit. on pp. 1–3).

[Asba2021] R. Asbai-Ghoudan, S. Ruiz De Galarreta, and N. Rodriguez-Florez. “Analytical model for the prediction of permeability of triply periodic minimal surfaces”. *Journal of the Mechanical Behavior of Biomedical Materials*, vol. 124. Dec. 2021. DOI: 10.1016/j.jmbbm.2021.104804 (cit. on pp. 33, 119).

[Barb2024] K. P. Barbian, L. T. Hirschwald, J. Linkhorst, M. Neidlin, U. Steinseifer, M. Wessling, B. Wiegmann, and S. V. Jansen. “Flow and mass transfer prediction in anisotropic TPMS-structures as extracorporeal oxygenator membranes using reduced order modeling”. *Journal of Membrane Science*, vol. 690. Jan. 2024. DOI: 10.1016/j.memsci.2023.122160 (cit. on p. 6).

[Baum2003] W. W. Baumann, U. Bunge, M. Schatz, and F. Thiele. *Finite-Volumen-Methode in der Numerischen Thermofluiddynamik*. 4th ed. Berlin: Fachbereich 10, TU Berlin, 2003. (Cit. on pp. 41–43, 45).

[Beel2016] B. M. Beely, J. E. Campbell, A. Meyer, T. Langer, K. Negaard, K. K. Chung, A. P. Cap, L. C. Cancio, and A. I. Batchinsky. "Electron Microscopy as a Tool for Assessment of Anticoagulation Strategies During Extracorporeal Life Support: The Proof Is on the Membrane". *ASAIO Journal*, vol. 62, no. 5. Sep. 2016. DOI: 10.1097/MAT.0000000000000394 (cit. on p. 90).

[Bhav2011] S. S. Bhavsar, T. Schmitz-Rode, and U. Steinseifer. "Numerical Modeling of Anisotropic Fiber Bundle Behavior in Oxygenators: ANISOTROPIC FIBER BUNDLE BEHAVIOR IN OXYGENATORS". *Artificial Organs*, vol. 35, no. 11. Nov. 2011. DOI: 10.1111/j.1525-1594.2011.01365.x (cit. on p. 4).

[Birk2018] C. Birkenmaier, T. Steiger, A. Philipp, K. Lehle, and L. Krenkel. "Flow-Induced Accumulations of Von Willebrand Factor Inside Oxygenators During Extracorporeal Life Support Therapy", in: *2018 International Conference BIOMDLORE*, Bialystok: IEEE, Jun. 2018. ISBN: 978-1-5386-2396-1.DOI: 10.1109/BIOMDLORE.2018.8467205 (cit. on p. 70).

[Bona2018] A. Bonavia, A. Groff, K. Karamchandani, and K. Singbartl. "Clinical Utility of Extracorporeal Cytokine Hemoadsorption Therapy: A Literature Review". *Blood Purification*, vol. 46, no. 4. 2018. DOI: 10.1159/000492379 (cit. on p. 5).

[Boyd2007] J. Boyd, J. M. Buick, and S. Green. "Analysis of the Casson and Carreau-Yasuda non-Newtonian blood models in steady and oscillatory flows using the lattice Boltzmann method". *Physics of Fluids*, vol. 19, no. 9. Sep. 2007. DOI: 10.1063/1.2772250 (cit. on p. 46).

[Brad2018] E. Bradford, A. M. Schweidtmann, and A. Lapkin. "Efficient multiobjective optimization employing Gaussian processes, spectral sampling and a genetic algorithm". *Journal of Global Optimization*, vol. 71, no. 2. Jun. 2018. DOI: 10.1007/s10898-018-0609-2 (cit. on pp. 47, 120).

[Casa2015] L. D. Casa, D. H. Deaton, and D. N. Ku. “Role of high shear rate in thrombosis”. *Journal of Vascular Surgery*, vol. 61, no. 4. Apr. 2015. DOI: 10.1016/j.jvs.2014.12.050 (cit. on pp. 2, 17, 50, 71, 122).

[Conr2018] S. A. Conrad, L. M. Broman, F. S. Taccone, R. Lorusso, M. V. Malfertheiner, F. Pappalardo, M. Di Nardo, M. Belliato, L. Grazioli, R. P. Barbaro, D. M. McMullan, V. Pellegrino, D. Brodie, M. M. Bembea, E. Fan, M. Mendonca, R. Diaz, and R. H. Bartlett. “The Extracorporeal Life Support Organization Maastricht Treaty for Nomenclature in Extracorporeal Life Support. A Position Paper of the Extracorporeal Life Support Organization”. *American Journal of Respiratory and Critical Care Medicine*, vol. 198, no. 4. Aug. 2018. DOI: 10.1164/rccm.201710-2130CP (cit. on pp. 1, 23).

[Cyto] CytoSorbents Europe GmbH, *Technical data - CytoSorb*. [Online]. Available: https://cytosorb-therapy.com/en/the-adsorber/technical-data/ (visited on 05/29/2029) (cit. on p. 87).

[Dams2011] J. Damstra, B. C. M. Oosterkamp, J. Jansma, and Y. Ren. “Combined 3-dimensional and mirror-image analysis for the diagnosis of asymmetry”. *American Journal of Orthodontics and Dentofacial Orthopedics*, vol. 140, no. 6. Dec. 2011. DOI: 10.1016/j.ajodo.2010.03.032 (cit. on p. 40).

[De S2013] F. De Somer. “Does contemporary oxygenator design influence haemolysis?”, *Perfusion*, vol. 28, no. 4. Jul. 2013. DOI: 10.1177/0267659113483803 (cit. on pp. 2, 3).

[DIN 2020] DIN Deutsches Institut für Normung e.V., *DIN EN ISO 7199:2020-10, Kardiovaskuläre Implantate und künstliche Organe_- Blut-Gas-Austauscher (Oxygenatoren) (ISO_7199:2016_+ Amd_1:2020); Deutsche Fassung EN_iso_7199:2017_+ A1:2020*, Oct. 2020. DOI: 10.31030/3129189. [Online]. Available: https://www.beuth.de/de/-/-/317329787 (visited on 05/29/2024) (cit. on pp. 76, 84).

[Dong2021] Z. Dong, H. Cui, H. Zhang, F. Wang, X. Zhan, F. Mayer, B. Nestler, M. Wegener, and P. A. Levkin. “3D printing of inherently nanoporous polymers via polymerization-induced phase separation”. *Nature Communications*, vol. 12, no. 1. Jan. 2021. DOI: 10.1038/s41467-020-20498-1 (cit. on p. 123).

[Duay2022] I. F. Duayer, M. J. C. L. N. Araújo, C. H. Nihei, M. A. F. Barcelos, O. Braga, Z. M. L. Britto, and R. M. Elias. “Dialysis-related thrombocytopenia: A case report”. *Brazilian Journal of Nephrology*, vol. 44, no. 1. Mar. 2022. DOI: 10.1590/2175-8239-jbn-2020-0109 (cit. on p. 88).

[Duy 2021] B. T. Duy Nguyen, H. Y. Nguyen Thi, B. P. Nguyen Thi, D.-K. Kang, and J. F. Kim. “The Roles of Membrane Technology in Artificial Organs: Current Challenges and Perspectives”. *Membranes*, vol. 11, no. 4. Mar. 2021. DOI: 10.3390/membranes11040239 (cit. on pp. 1–4, 28).

[Eloo2002] S. Eloot, D. De Wachter, I. Van Tricht, and P. Verdonck. “Computational Flow Modeling in Hollow-Fiber Dialyzers”. *Artificial Organs*, vol. 26, no. 7. 2002. DOI: 10.1046/j.1525-1594.2002.07081.x (cit. on p. 4).

[Evse2019] A. K. Evseev, S. V. Zhuravel, A. Y. Alentiev, I. V. Goroncharovskaya, and S. S. Petrikov. “Membranes in Extracorporeal Blood Oxygenation Technology”. *Membranes and Membrane Technologies*, vol. 1, no. 4. Jul. 2019. DOI: 10.1134/S2517751619040024 (cit. on p. 24).

[Fåhr1929] R. Fåhræus. “THE SUSPENSION STABILITY OF THE BLOOD”. *Physiological Reviews*, vol. 9, no. 2. Apr. 1929. DOI: 10.1152/physrev.1929.9.2.241 (cit. on pp. 15, 76).

[Feau2023] T. Feaugas, G. Newman, S. T. Calzuola, A. Domingues, W. Arditi, C. Porrini, E. Roy, and C. M. Perrault. “Design of artificial vascular devices: Hemodynamic evaluation of shear-induced thrombogenicity”. *Frontiers in Mechanical Engineering*, vol. 9. Feb. 2023. DOI: 10.3389/fmech.2023.1060580 (cit. on pp. 50, 70).

[Femm2015a] T. Femmer, A. J. Kuehne, J. Torres-Rendon, A. Walther, and M. Wessling. “Print your membrane: Rapid prototyping of complex 3D-PDMS membranes via a sacrificial resist”. *Journal of Membrane Science*, vol. 478. Mar. 2015. DOI: 10.1016/j.memsci.2014.12.040 (cit. on pp. 6, 32, 76).

[Femm2015b] T. Femmer, A. J. Kuehne, and M. Wessling. “Estimation of the structure dependent performance of 3-D rapid prototyped membranes”. *Chemical Engineering Journal*, vol. 273. Aug. 2015. DOI: 10.1016/j.cej.2015.03.029 (cit. on pp. 32, 76).

[Feng2022] J. Feng, J. Fu, X. Yao, and Y. He. “Triply periodic minimal surface (TPMS) porous structures: From multi-scale design, precise additive manufacturing to multidisciplinary applications”. *International Journal of Extreme Manufacturing*, vol. 4, no. 2. Jun. 2022. DOI: 10.1088/2631-7990/ac5be6 (cit. on p. 6).

[Fern2017] U. P. Fernando, A. J. Thompson, J. Potkay, H. Cheriyan, J. Toomasian, A. Kaesler, P. Schlanstein, J. Arens, R. B. Hirschl, J. L. Bull, and R. H. Bartlett. “A Membrane Lung Design Based on Circular Blood Flow Paths”. *ASAIO Journal*, vol. 63, no. 5. Sep. 2017. DOI: 10.1097/MAT.0000000000000616 (cit. on pp. 3, 4).

[Fick1855] A. Fick. “Ueber Diffusion”. *Annalen der Physik*, vol. 170, no. 1. Jan. 1855. DOI: 10.1002/andp.18551700105 (cit. on p. 20).

[Flec2023] E. Fleck, C. Keck, K. Ryszka, E. DeNatale, and J. Potkay. “Low-Viscosity Polydimethylsiloxane Resin for Facile 3D Printing of Elastomeric Microfluidics”. *Micromachines*, vol. 14, no. 4. Mar. 2023. DOI: 10.3390/mi14040773 (cit. on p. 123).

[Foge2015] A. L. Fogelson and K. B. Neeves. “Fluid Mechanics of Blood Clot Formation”. *Annual Review of Fluid Mechanics*, vol. 47, no. 1. Jan. 2015. DOI: 10.1146/annurev-fluid-010814-014513 (cit. on p. 15).

[Freu2014] J. B. Freund. “Numerical Simulation of Flowing Blood Cells”. *Annual Review of Fluid Mechanics*, vol. 46, no. 1. Jan. 2014. DOI: 10.1146/annurev-fluid-010313-141349 (cit. on p. 46).

[Fuch2023] A. Fuchs, N. Berg, L. Fuchs, and L. Prahl Wittberg. “Assessment of Rheological Models Applied to Blood Flow in Human Thoracic Aorta”. *Bioengineering*, vol. 10, no. 11. Oct. 2023. DOI: 10.3390/bioengineering10111240 (cit. on p. 46).

[Goh2024] T. Goh, L. Gao, J. Singh, R. Totaro, R. Carey, K. Yang, B. Cartwright, M. Dennis, L. A. Ju, and A. Waterhouse. “Platelet Adhesion and Activation in an ECMO Thrombosis-on-a-Chip Model”.

Advanced Science. May 2024. DOI: 10.1002/advs.202401524 (cit. on p. 1).

[Gund2020] G. Gundersen, *Understanding Moments*, Apr. 2020. [Online]. Available: https://gregorygundersen.com/blog/2020/04/11/moments/ (visited on 02/20/2024) (cit. on p. 40).

[Hall2011] J. E. Hall and A. C. Guyton. *Guyton and Hall textbook of medical physiology*. 12th ed. Philadelphia, Pa: Saunders/Elsevier, 2011. ISBN: 978-1-4160-4574-8. (Cit. on pp. 11–13, 18, 20–22, 28).

[Haut2020] S. Hautala. *Physics Across Oceanography: Fluid Mechanics and Waves*. Washington, 2020. (Cit. on p. 45).

[Hawk2023] M. Hawken, S. Reid, D. Clarke, M. Watson, C. Fee, and D. Holland. "Characterization of pressure drop through Schwarz-Diamond triply periodic minimal surface porous media". *Chemical Engineering Science*, vol. 280. Oct. 2023. DOI: 10.1016/j.ces.2023.119039 (cit. on pp. 30, 32, 33, 68).

[Herc2016] R. Herczyński. "Fåhræus effect revisited". *Archives of Mechanics*, vol. 68, no. 1. 2016. (Cit. on pp. 15, 16, 76).

[Hess2021] F. Hesselmann, N. Scherenberg, P. Bongartz, S. Djeljadini, M. Wessling, C. Cornelissen, T. Schmitz-Rode, U. Steinseifer, S. V. Jansen, and J. Arens. "Structure-dependent gas transfer performance of 3D-membranes for artificial membrane lungs". *Journal of Membrane Science*, vol. 634. Sep. 2021. DOI: 10.1016/j.memsci.2021.119371 (cit. on pp. 6, 50, 76).

[Hess2022] F. Hesselmann, M. Halwes, P. Bongartz, M. Wessling, C. Cornelissen, T. Schmitz-Rode, U. Steinseifer, S. V. Jansen, and J. Arens. "TPMS-based membrane lung with locally-modified permeabilities for optimal flow distribution". *Scientific Reports*, vol. 12, no. 1. May 2022. DOI: 10.1038/s41598-022-11175-y (cit. on pp. 3, 6, 50, 69, 94).

[Hira2009] A. Hirano, K.-i. Yamamoto, M. Matsuda, M. Inoue, S. Nagao, K. Kuwana, M. Kamiya, and K. Sakai. "Flow Uniformity in Oxygenators with Different Outlet Port Design". *ASAIO Journal*, vol. 55, no. 3. May 2009. DOI: 10.1097/MAT.0b013e31819c6f19 (cit. on p. 3).

[Hira2011] A. Hirano, K.-i. Yamamoto, M. Matsuda, T. Ogawa, T. Yakushiji, T. Miyasaka, and K. Sakai. “Evaluation of Dialyzer Jacket Structure and Hollow-Fiber Dialysis Membranes to Achieve High Dialysis Performance: Evaluation of Dialyzer Jacket Structure”. *Therapeutic Apheresis and Dialysis*, vol. 15, no. 1. Feb. 2011. DOI: 10.1111/j.1744-9987.2010.00869.x (cit. on p. 5).

[Hira2012] A. Hirano, S. Kida, K.-i. Yamamoto, and K. Sakai. “Experimental evaluation of flow and dialysis performance of hollow-fiber dialyzers with different packing densities”. *Journal of Artificial Organs*, vol. 15, no. 2. Jun. 2012. DOI: 10.1007/s10047-011-0620-6 (cit. on pp. 5, 50, 67, 68).

[Hosc2024] W. L. Hosch, *Navier-Stokes equation*, May 2024. [Online]. Available: https://www.britannica.com/science/Navier-Stokes-equation (visited on 07/28/2024) (cit. on p. 45).

[Hoss2017] H. Hosseinzadegan and D. K. Tafti. “Modeling thrombus formation and growth”. *Biotechnology and Bioengineering*, vol. 114, no. 10. Oct. 2017. DOI: 10.1002/bit.26343 (cit. on p. 13).

[Hous2017] K. S. Houschyar, M. N. Pyles, S. Rein, I. Nietzschmann, D. Duscher, Z. N. Maan, K. Weissenberg, H. M. Philipps, C. Strauss, B. Reichelt, and F. Siemers. “Continuous Hemoadsorption with a Cytokine Adsorber during Sepsis – a Review of the Literature”. *The International Journal of Artificial Organs*, vol. 40, no. 5. May 2017. DOI: 10.5301/ijao.5000591 (cit. on p. 4).

[Jaco2008] J. Jacobi, “Minimalflächen”, Hausarbeit, Universität zu Köln, Köln, Aug. 2008. [Online]. Available: www.igt.uni-stuttgart.de/dokumente/semmelmann/abschlussarbeiten/jacobi.pdf (visited on 03/11/2024) (cit. on p. 30).

[Kalb2018] J. Kalbhenn, A. Schlagenhauf, S. Rosenfelder, A. Schmutz, and B. Zieger. “Acquired von Willebrand syndrome and impaired platelet function during venovenous extracorporeal membrane oxygenation: Rapid onset and fast recovery”. *The Journal of Heart and Lung Transplantation*, vol. 37, no. 8. Aug. 2018. DOI: 10.1016/j.healun.2018.03.013 (cit. on p. 88).

[Karc1989] H. Karcher. “The triply periodic minimal surfaces of Alan Schoen and their constant mean curvature companions”. *Manuscripta Mathematica*, vol. 64, no. 3. Sep. 1989. DOI: 10.1007/BF01165824 (cit. on p. 30).

[Kim2009] J. C. Kim, J. H. Kim, J. Sung, H.-C. Kim, E. Kang, S. H. Lee, J. K. Kim, H. C. Kim, B. G. Min, and C. Ronco. “Effects of Arterial Port Design on Blood Flow Distribution in Hemodialyzers”. *Blood Purification*, vol. 28, no. 3. Aug. 2009. DOI: 10.1159/000232934 (cit. on pp. 4, 5, 50, 68).

[Kim2012] J. C. Kim, F. Garzotto, D. N. Cruz, A. Clementi, F. Nalesso, J. H. Kim, E. Kang, H. C. Kim, and C. Ronco. “Computational Modeling of Effects of Mechanical Shaking on Hemodynamics in Hollow Fibers”. *The International Journal of Artificial Organs*, vol. 35, no. 4. Apr. 2012. DOI: 10.5301/ijao.5000094 (cit. on p. 5).

[Lai2024] A. Lai, N. Omori, J. E. Napolitano, J. F. Antaki, and K. E. Cook, “Effect of Artificial Lung Fiber Bundle Geometric Design on Micro- and Macro-scale Clot Formation”, Bioengineering, preprint, Jan. 2024. DOI: 10.1101/2024.01.05.574443. [Online]. Available: http://biorxiv.org/lookup/doi/10.1101/2024.01.05.574443 (visited on 01/11/2024) (cit. on pp. 76, 90).

[Lehl2008] K. Lehle, A. Philipp, O. Gleich, A. Holzamer, T. Müller, T. Bein, and C. Schmid. “Efficiency in Extracorporeal Membrane Oxygenation—Cellular Deposits on Polymethypentene Membranes Increase Resistance to Blood Flow and Reduce Gas Exchange Capacity”. *ASAIO Journal*, vol. 54, no. 6. Nov. 2008. DOI: 10.1097/MAT.0b013e318186a807 (cit. on pp. 4, 76, 90).

[Leve1999] O. Levenspiel. *Chemical reaction engineering*. 3rd ed. New York: Wiley, 1999. ISBN: 978-0-471-25424-9. (Cit. on p. 34).

[Li2023] J. Li, T. He, H. Chen, Y. Cheng, E. Drioli, Z. Wang, and Z. Cui. “Preparation of Hyflon AD/Polypropylene Blend Membrane for Artificial Lung”. *Membranes*, vol. 13, no. 7. Jul. 2023. DOI: 10.3390/membranes13070665 (cit. on p. 4).

[Lim2006] M. W. Lim. “The history of extracorporeal oxygenators”. *Anaesthesia*, vol. 61, no. 10. Oct. 2006. DOI: 10.1111/j.1365-2044.2006.04781.x (cit. on p. 3).

[Luel2017] T. Luelf, M. Tepper, H. Breisig, and M. Wessling. “Sinusoidal shaped hollow fibers for enhanced mass transfer”. *Journal of Membrane Science*, vol. 533. Jul. 2017. DOI: 10.1016/j.memsci.2017.03.030 (cit. on p. 5).

[Mart2023] A. Martins Costa, F. R. Halfwerk, J.-N. Thiel, B. Wiegmann, M. Neidlin, and J. Arens. “Effect of hollow fiber configuration and replacement on the gas exchange performance of artificial membrane lungs”. *Journal of Membrane Science*, vol. 680. Aug. 2023. DOI: 10.1016/j.memsci.2023.121742 (cit. on pp. 3, 4).

[Maza2006] A. R. Mazaheri and G. Ahmadi. “Uniformity of the Fluid Flow Velocities Within Hollow Fiber Membranes of Blood Oxygenation Devices”. *Artificial Organs*, vol. 30, no. 1. Jan. 2006. DOI: 10.1111/j.1525-1594.2006.00150.x (cit. on p. 4).

[McCa2023] S. G. McCallum, J. E. Lerpinière, K. O. Jensen, P. Friederich, and A. B. Walker. “Bayesian optimization approach to quantify the effect of input parameter uncertainty on predictions of numerical physics simulations”. *APL Machine Learning*, vol. 1, no. 4. Dec. 2023. DOI: 10.1063/5.0151747 (cit. on pp. 46, 47).

[Medt2020] Medtronic, *Technical Data Sheet Clearum HS series high flux dialyzer*, 2020. [Online]. Available: https://www.medtronic.com/covidien/en-us/products/chronic-dialysis-solutions/dialyzers/clearum-hs-high-flux-dialyzers.html (visited on 05/29/2024) (cit. on p. 87).

[Meht2023] Y. Mehta, R. Paul, A. S. Ansari, T. Banerjee, S. Gunaydin, A. A. Nassiri, F. Pappalardo, V. Premužić, P. Sathe, V. Singh, and E. R. Vela. “Extracorporeal blood purification strategies in sepsis and septic shock: An insight into recent advancements”. *World Journal of Critical Care Medicine*, vol. 12, no. 2. Mar. 2023. DOI: 10.5492/wjccm.v12.i2.71 (cit. on pp. 1, 29).

[Mine2015] M. Mineshima. “The Past, Present and Future of the Dialyzer”, in: *Contributions to Nephrology*. K. Nitta, Ed., vol. 185, S. Karger AG, 2015. ISBN: 978-3-318-05465-1.DOI: 10.1159/000380965 (cit. on pp. 2, 4).

[Mona2019] C. Monard, T. Rimmelé, and C. Ronco. “Extracorporeal Blood Purification Therapies for Sepsis”. *Blood Purification*, vol. 47, no. Suppl. 3. 2019. DOI: 10.1159/000499520 (cit. on p. 29).

[Most2021] A. H. Mostafavi, A. K. Mishra, M. Ulbricht, J. Denayer, and S. S. Hosseini. “Oxygenation and Membrane Oxygenators: Emergence Evolution and Progress in Material Development and Process Enhancement for Biomedical Applications”. *Journal of Membrane Science and Research*, vol. 7, no. 4. Oct. 2021. DOI: 10.22079/jmsr.2021.521505.1431 (cit. on pp. 24, 25, 27).

[Mull2009] T. Muller, M. Lubnow, A. Philipp, T. Bein, A. Jeron, A. Luchner, L. Rupprecht, M. Reng, J. Langgartner, C. E. Wrede, M. Zimmermann, D. Birnbaum, C. Schmid, G. A. J. Riegger, and M. Pfeifer. “Extracorporeal pumpless interventional lung assist in clinical practice: Determinants of efficacy”. *European Respiratory Journal*, vol. 33, no. 3. Mar. 2009. DOI: 10.1183/09031936.00123608 (cit. on p. 3).

[Osug2004] T. Osuga, T. Obata, and H. Ikehira. “Detection of small degree of nonuniformity in dialysate flow in hollow-fiber dialyzer using proton magnetic resonance imaging”. *Magnetic Resonance Imaging*, vol. 22, no. 3. Apr. 2004. DOI: 10.1016/j.mri.2003.08.008 (cit. on p. 4).

[Park2020] A. Park, Y. Song, E. Yi, B. T. Duy Nguyen, D. Han, E. Sohn, Y. Park, J. Jung, Y. M. Lee, Y. H. Cho, and J. F. Kim. “Blood Oxygenation Using Fluoropolymer-Based Artificial Lung Membranes”. *ACS Biomaterials Science & Engineering*, vol. 6, no. 11. Nov. 2020. DOI: 10.1021/acsbiomaterials.0c01251 (cit. on pp. 2, 4).

[Phil2018] A. Philipp, F. De Somer, M. Foltan, A. Bredthauer, L. Krenkel, F. Zeman, and K. Lehle. “Life span of different extracorporeal membrane systems for severe respiratory failure in the clinical practice”. *PLOS ONE*, vol. 13, no. 6, G. Erdoes, Ed. Jun. 2018. DOI: 10.1371/journal.pone.0198392 (cit. on p. 3).

[Polk2010] A. A. Polk, T. M. Maul, D. T. McKeel, T. A. Snyder, C. A. Lehocky, B. Pitt, D. B. Stolz, W. J. Federspiel, and W. R. Wagner. “A biohybrid artificial lung prototype with active mixing of endothelialized mi-

croporous hollow fibers". *Biotechnology and Bioengineering*. 2010. DOI: 10.1002/bit.22675 (cit. on p. 4).

[Prie1990] A. R. Pries, T. W. Secomb, P. Gaehtgens, and J. F. Gross. "Blood flow in microvascular networks. Experiments and simulation." *Circulation Research*, vol. 67, no. 4. Oct. 1990. DOI: 10.1161/01.RES.67.4.826 (cit. on pp. 15, 16).

[Prie1992] A. R. Pries, D. Neuhaus, and P. Gaehtgens. "Blood viscosity in tube flow: Dependence on diameter and hematocrit". *American Journal of Physiology-Heart and Circulatory Physiology*, vol. 263, no. 6. Dec. 1992. DOI: 10.1152/ajpheart.1992.263.6.H1770 (cit. on pp. 16, 17).

[Rack2017] K. Rack, V. Huck, M. Hoore, D. A. Fedosov, S. W. Schneider, and G. Gompper. "Margination and stretching of von Willebrand factor in the blood stream enable adhesion". *Scientific Reports*, vol. 7, no. 1. Oct. 2017. DOI: 10.1038/s41598-017-14346-4 (cit. on pp. 15, 17).

[Reyn1883] O. Reynolds. "An Experimental Investigation of the Circumstances Which Determine Whether the Motion of Water Shall Be Direct or Sinuous, and of the Law of Resistance in Parallel Channels". *Philosophical Transactions of the Royal Society of London*, vol. 17. 1883. (Cit. on p. 14).

[Roll2005] S. Roller, M. Ferch, C.-D. Munz, and M. Dumbser, *Numerische Grundlagen: Finite Differenzen, Finite Elemente, Finite Volumen*, Stuttarg, 2005. [Online]. Available: https://fs.hlrs.de/projects/par/par_prog_ws/2005D/cfd-05-b.pdf (visited on 07/28/2024) (cit. on p. 43).

[Ronc2001] C. Ronco, P. M. Ghezzi, G. Metry, M. Spittle, A. Brendolan, M. P. Rodighiero, M. Milan, M. Zanella, G. La Greca, and N. W. Levin. "Effects of Hematocrit and Blood Flow Distribution on Solute Clearance in Hollow-Fiber Hemodialyzers". *Nephron*, vol. 89, no. 3. 2001. DOI: 10.1159/000046080 (cit. on p. 4).

[Ronc2002] C. Ronco, A. Brendolan, C. Crepaldi, M. Rodighiero, and M. Scabardi. "Blood and Dialysate Flow Distributions in Hollow-Fiber Hemodialyzers Analyzed by Computerized Helical Scanning Technique". *Journal of the American Society of Nephrology*, vol. 13,

no. suppl_1. Jan. 2002. DOI: 10.1681/ASN.V13suppl_1s53 (cit. on pp. 4, 50, 67, 70).

[Ronc2007] C. Ronco. “Fluid Mechanics and Crossfiltration in Hollow-Fiber Hemodialyzers”, in: *Contributions to Nephrology*. C. Ronco, B. Canaud, and P. Aljama, Eds., vol. 158, Basel: S. KARGER AG, 2007. ISBN: 978-3-318-01494-5.DOI: 10.1159/000107233 (cit. on p. 94).

[Ronc2022] C. Ronco and R. Bellomo. “Hemoperfusion: Technical aspects and state of the art”. *Critical Care*, vol. 26, no. 1. May 2022. DOI: 10.1186/s13054-022-04009-w (cit. on pp. 1, 5, 29, 30).

[Saka2015] K. S. Sakariassen, L. Orning, and V. T. Turitto. “The impact of blood shear rate on arterial thrombus formation”. *Future Science OA*, vol. 1, no. 4. Nov. 2015. DOI: 10.4155/fso.15.28 (cit. on p. 2).

[Sand2023] R. Sander. “Compilation of Henry’s law constants (version 5.0.0) for water as solvent”. *Atmospheric Chemistry and Physics*, vol. 23, no. 19. Oct. 2023. DOI: 10.5194/acp-23-10901-2023 (cit. on p. 20).

[Sant2020] J. Santos, T. Pires, B. P. Gouveia, A. P. Castro, and P. R. Fernandes. “On the permeability of TPMS scaffolds”. *Journal of the Mechanical Behavior of Biomedical Materials*, vol. 110. Oct. 2020. DOI: 10.1016/j.jmbbm.2020.103932 (cit. on pp. 104, 114).

[Schl2014] P. C. Schlanstein, R. Borchardt, I. Mager, T. Schmitz-Rode, U. Steinseifer, and J. Arens. “Gas Exchange Efficiency of an Oxygenator with Integrated Pulsatile Displacement Blood Pump for Neonatal Patients”. *The International Journal of Artificial Organs*, vol. 37, no. 1. Jan. 2014. DOI: 10.5301/ijao.5000293 (cit. on p. 4).

[Schl2017] H. Schlichting and K. Gersten. *Boundary-Layer Theory*. Berlin, Heidelberg: Springer Berlin Heidelberg, 2017. ISBN: 978-3-662-52919-5.DOI: 10.1007/978-3-662-52919-5 (cit. on p. 14).

[Schn2007] S. W. Schneider, S. Nuschele, A. Wixforth, C. Gorzelanny, A. Alexander-Katz, R. R. Netz, and M. F. Schneider. “Shear-induced unfolding triggers adhesion of von Willebrand factor fibers”. *Proceedings of the National Academy of Sciences*, vol. 104, no. 19. May 2007. DOI: 10.1073/pnas.0608422104 (cit. on pp. 2, 17).

[Scho1970] A. H. Schoen, *Infinite Periodic Minimal Surfaces Without Self-Intersections*, May 1970. [Online]. Available: https://ntrs.nasa.gov/citations/19700020472 (visited on 08/30/2023) (cit. on pp. 6, 30).

[Schw1890] H. A. Schwarz. *Gesammelte Mathematische Abhandlungen: Erster Band*. Berlin, Heidelberg: Springer Berlin Heidelberg, 1890. ISBN: 978-3-642-50356-6.DOI: 10.1007/978-3-642-50665-9 (cit. on pp. 6, 30).

[Schw2024] R. S. Schwartz and C. L. Conley, *Blood*, Apr. 2024. [Online]. Available: https://www.britannica.com/science/blood-biochemistry (visited on 05/14/2024) (cit. on pp. 11–13).

[Seeh2023] S. Seehanam, W. Chanchareon, and P. Promoppatum. "Assessing the effect of manufacturing defects and non-Newtonian blood model on flow behaviors of additively manufactured Gyroid TPMS structures". *Heliyon*, vol. 9, no. 5. May 2023. DOI: 10.1016/j.heliyon.2023.e15711 (cit. on pp. 46, 54, 66).

[Snyd2011] L. R. Snyder, J. J. Kirkland, and J. W. Dolan. *Introduction to Modern Liquid Chromatography*. 3rd ed. New York, NY: John Wiley & Sons, 2011. ISBN: 978-1-118-21039-0. (Cit. on p. 5).

[Swee2014] J. Sweeny, *Dialyzer*, Mar. 2014. [Online]. Available: https://www.dialysistech.net/images/DialyzerManual.pdf (visited on 05/29/2029) (cit. on p. 87).

[Tian2024] L. Tian, B. Sun, X. Yan, A. Sharf, C. Tu, and L. Lu. "Continuous transitions of triply periodic minimal surfaces". *Additive Manufacturing*, vol. 84. Mar. 2024. DOI: 10.1016/j.addma.2024.104105 (cit. on pp. 6, 32, 67).

[Umat2019] U. Umatheva, G. Chen, and R. Ghosh. "Computational fluid dynamic (CFD) simulation of a cuboid packed-bed chromatography device". *Chemical Engineering Research and Design*, vol. 152. Dec. 2019. DOI: 10.1016/j.cherd.2019.10.005 (cit. on pp. 5, 50, 67, 68, 94).

[Wu2022] Z. Wu, X. Gao, H. Long, and W. Lai. “Quantitative analysis of facial symmetry by using three-dimensional technology”. *BMC Oral Health*, vol. 22, no. 1. Dec. 2022. DOI: 10.1186/s12903-022-02315-x (cit. on p. 40).

[Yama2007] K.-I. Yamamoto, H. Matsukawa, T. Yakushiji, M. Fukuda, T. Hiyoshi, and K. Sakai. “Technical Evaluation of Dialysate Flow in a Newly Designed Dialyzer”. *ASAIO Journal*, vol. 53, no. 1. Jan. 2007. DOI: 10.1097/01.mat.0000245525.83936.79 (cit. on p. 5).

[Yama2009] K.-i. Yamamoto, M. Matsuda, A. Hirano, N. Takizawa, S. Iwashima, T. Yakushiji, M. Fukuda, T. Miyasaka, and K. Sakai. “Computational Evaluation of Dialysis Fluid Flow in Dialyzers With Variously Designed Jackets”. *Artificial Organs*, vol. 33, no. 6. Jun. 2009. DOI: 10.1111/j.1525-1594.2009.00753.x (cit. on pp. 5, 94).

[Yao2024] S. Yao, H. Yan, S. Tian, R. Luo, Y. Zhao, and J. Wang. “Antifouling coatings for blood-contacting devices”. *Smart Materials in Medicine*, vol. 5, no. 1. Mar. 2024. DOI: 10.1016/j.smaim.2023.10.001 (cit. on p. 4).

[Zhan2007] J. Zhang, T. D. Nolan, T. Zhang, B. P. Griffith, and Z. J. Wu. “Characterization of membrane blood oxygenation devices using computational fluid dynamics”. *Journal of Membrane Science*, vol. 288, no. 1-2. Feb. 2007. DOI: 10.1016/j.memsci.2006.11.041 (cit. on p. 4).

[Zhan2013] J. Zhang, X. Chen, J. Ding, K. H. Fraser, M. Ertan Taskin, B. P. Griffith, and Z. J. Wu. “Computational Study of the Blood Flow in Three Types of 3D Hollow Fiber Membrane Bundles”. *Journal of Biomechanical Engineering*, vol. 135, no. 12. Dec. 2013. DOI: 10.1115/1.4025717 (cit. on p. 4).

[Zhu2022] Y. Zhu, Y. Zhao, and Y. Wang. “A Review of Three-Dimensional Facial Asymmetry Analysis Methods”. *Symmetry*, vol. 14, no. 7. Jul. 2022. DOI: 10.3390/sym14071414 (cit. on p. 40).

List of Symbols

Fundamentals

ΔP	pressure drop	(mmHg)
$\dot{\gamma}$	shear rate	(s^{-1})
$\dot{V}$	volumetric flow rate	($m^3\,s^{-1}$)
η	dynamic viscosity	(Pa s)
κ	permeability in porous media	(m^2)
ϕ	porosity	(-)
ρ	density	($kg\,m^{-3}$)
c	concentration	($mol\,m^{-3}$)
d	diameter	(m)
Hct	hematocrit	(vol%)
J	diffusion flux	($mol\,m^{-2}\,s^{-1}$)
P	pressure	(mmHg) or (Pa)
P_i	partial pressure	(Pa)
Q	Permeance	($m^3\,m^{-2}\,h^{-1}\,bar^{-1}$)
T	temperature	(K or °C)
t	time	(s)
V	volume	(m^3)
v	velocity	($m\,s^{-1}$)

Constants, Coefficients, Dimensionless Quantities

D	diffusion coefficient	$(m^2\,s^{-1})$
D_K	Knudsen diffusion coefficient	$(m^2\,s^{-1})$
H_s^{cp}	Henry's law solubility constant	$(mol\,m^{-3}\,Pa^{-1})$
M	molar mass	$(kg\,mol^{-1})$
R	gas constant	$(8.314\,J\,mol^{-1}\,K^{-1})$
Re	Reynolds number	(-)
SAV	surface area to volume ratio	(m^{-1})

Residence Time Distribution (RTD) Symbols

$\mathbb{E}$	statistical moment	
μ_k	kth raw moment	(s^k)
σ^2	second central moment and distribution's variance	(s^2)
σ_k	kth standard deviation	(s^k)
τ	mean residence time	(s)
θ	dimensionless residence time	(-)
$\widehat{m}_k$	kth standardized moment	(-)
$c(t)$	tracer concentration at module's outlet	$(mol\,m^{-3})$
$E(t)$	residence time distribution density function	(s^{-1})
$E_\theta(\theta)$	dimensionless residence time distribution density function	(-)
m_k	kth central moment	(s^k)
n_{tracer}	amount of tracer	(mol)

Triply Periodic Minimal Surface (TPMS) Symbols

A_{wet}	wetted surface area	(m^2)
d_{hyd}	hydraulic diameter	(m)
Re_{hyd}	Reynolds number based on hydraulic diameter	(-)
s_{chan}	TPMS channel size	(m)

s_{off}	TPMS surface offset	(m)
s_{unit}	TPMS unit cell size	(m)
t_{wall}	TPMS wall thickness	(m)
V_{free}	volume not occupied by TPMS structure	(m^3)
V_{unit}	volume of entire TPMS unit cell	(m^3)
V_{wall}	volume of TPMS wall	(m^3)

Chapter 4: Clotting

ΔV_{clot}	relative volume of clotted blood	(%)
$\overline{PLT'}$	corrected & normalized platelet count	(%)
PLT	platelet count	(μL^{-1})
PLT'	corrected platelet count	(%)

Chapter 5: Optimization

α_{in}	module's inclination angle at inlet	(°)
α_{out}	module's inclination angle at outlet	(°)
$\dot{\gamma}_{av}$	average shear rate	(s^{-1})
$\dot{\gamma}_{max}$	maximum shear rate	(s^{-1})
$\widetilde{E}_{\leftarrow}(t)$	left tail of RTD density function mirrored along $t(E_{max})$	(s^{-1})
b_{in}	module's Bézier parameter for Bézier curve at inlet	(-)
b_{out}	module's Bézier parameter for Bézier curve at outlet	(-)
$E_{\leftarrow}(t)$	left tail of RTD density function	(s^{-1})
$E_{\rightarrow}(t)$	right tail of RTD density function	(s^{-1})
E_{max}	maximum of RTD density function	(s^{-1})
L_0	module base length	(m)
L_{end}	module end cap length	(m)
L_{mod}	module length	(m)
n_{radial}	module's number of radial domains	(-)

$n_{vertical}$	module's number of vertical domains	(-)
p	module's optimization parameter as sum of squares	(n.a.)
p_{broad}	module's optimization parameter for it's broadening	(s)
p_{pos}	module's optimization parameter for it's position	(s)
p_{sym}	module's optimization parameter for it's symmetry	(-)
r_{fillet}	module's fillet radius for all corners	(m)

List of Abbreviations

ACT activated clotting time

ADP adenosine diphosphate

ATP adenosine triphosphate

CAD computer aided design

CFD computational fluid dynamics

CT computed tomography

ECCO$_2$R extracorporeal CO_2 removal

ECLS extracorporeal life support

ECMO extracorporeal membrane oxygenation

FD finite difference

FE finite element

FV finite volume

Hb hemoglobin

Hct hematocrit

HPLC high pressure liquid chromatography

PDMS polydimethylsiloxane

PMP polymethylpentene

PP polypropylene

RTD residence time distribution

SAV surface area to volume ratio

SPH smoothed-particle hydrodynamics

TPMS triply periodic minimal surface

TSEMO Thompson sampling efficient multi-objective optimization

vWf von Willebrand factor